

Stellar CoRGI in MaNGA: Stellar Counter-Rotation Galaxies Identified in MaNGA Survey

DAMIR GASYMOV ^{1,2} IVAN YU. KATKOV ^{3,4,2} EVGENII V. RUBTSOV ² ANNA S. SABUROVA ²
ALEXEI YU. KNIAZEV ^{5,6,7,2} JOSEPH D. GELFAND ^{3,4,8} OLGA K. SIL'CHENKO ² IGOR V. CHILINGARIAN ^{9,2}
ALEXEI V. MOISEEV ^{7,2} ANASTASIA V. KASPAROVA ² AND ANATOLY ZASOV ^{2,10}

¹*Astronomisches Rechen-Institut, Zentrum für Astronomie der Universität Heidelberg, Mönchhofstr. 12–14, 69120 Heidelberg, Germany*

²*Sternberg Astronomical Institute, Lomonosov Moscow State University, Universitetskij pr., 13, Moscow, 119234, Russia*

³*New York University Abu Dhabi, PO Box 129188, Abu Dhabi, UAE*

⁴*Center for Astrophysics and Space Science (CASS), New York University Abu Dhabi, PO Box 129188, Abu Dhabi, UAE*

⁵*South African Astronomical Observatory, PO Box 9, 7935 Observatory, Cape Town, South Africa*

⁶*Southern African Large Telescope Foundation, PO Box 9, 7935 Observatory, Cape Town, South Africa*

⁷*Special Astrophysical Observatory of the Russian Academy of Sciences, Nizhnij Arkhyz, 369167 Russia*

⁸*Center for Cosmology and Particle Physics, New York University, 726 Broadway, room 958, New York, NY 10003*

⁹*Center for Astrophysics — Harvard and Smithsonian, 60 Garden St. MS09, Cambridge, MA 02138, USA*

¹⁰*Faculty of Physics, Moscow M.V. Lomonosov State University, Leninskie gory 1, Moscow, 119991, Russia*

Abstract

Counter-rotating (CR) galaxies consist of two coplanar stellar disks rotating in opposite directions – the main, pre-existing disk with an older stellar population and a younger CR disk likely formed from externally acquired gas. Such systems offer a unique opportunity to study disk assembly by analyzing the stellar populations of each component. Using integral field spectroscopic data from the SDSS-IV Mapping Nearby Galaxies at Apache Point Observatory (MaNGA) survey, we identified a sample of 120 CR disk galaxies by inspecting their kinematic maps and analyzing the shape of the stellar line-of-sight velocity distribution (LOSVD), which was recovered non-parametrically. For one-third of our sample, we further derived the ages and metallicities of stars for both disks via a spectral decomposition technique. We show that the observed kinematic bimodality — where the CR disk is either concentrated in the central region (inner CR) or dominates the outer part of the galaxy (outer CR) — is driven by differences in the stellar mass and angular momentum of the CR disk. The wide range of stellar metallicities observed in CR disks suggests that no single source of external material is solely responsible for CR formation in all galaxies; instead, proposed mechanisms such as merger with gas-rich satellites, accretion from cosmic filaments, and exchange of gas between neighboring galaxies can dominate in individual cases.

Keywords: Disk galaxies (391); Galaxy kinematics (602); Galaxy stellar content (621); Galaxy accretion (575)

1. INTRODUCTION

Understanding how galaxies build their disks is one of the fundamental questions in galaxy physics. However, observationally probing the details of this process is challenging because observed galaxies have already assembled disks, and reconstructing their formation history from spectra integrated along line-of-sight is non-trivial. One of the main challenges is that galaxies are not closed, isolated systems; they experience mergers

with other galaxies (Toomre & Toomre 1972; Barnes 1988) and accrete external material (Sancisi et al. 2008; Combes 2014; Putman 2017). The acquisition of a substantial amount of material, particularly if this material has angular momentum opposite to that of the host, can lead to the formation of distinct kinematic components. Galaxies with these features, termed “multi-spin” galaxies (Rubin 1994), include remarkable examples where two stellar disks rotate in the same plane but in opposite directions, known as counter-rotating (CR) stellar disks. CR in disks is particularly intriguing because the high rotational amplitude generates pronounced kinematic separation, which facilitates disen-

tangling the stellar populations in the two disks and provides insights into the formation and evolution of each.

Co-spatial stellar CR disks were first discovered and studied in NGC 4550 by [Rubin et al. \(1992\)](#) and [Rix et al. \(1992\)](#). Notably, even before this discovery, evidence for stellar CR had been found in elliptical galaxies through the detection of kinematically decoupled cores and nuclear disks ([Franx & Illingworth 1988](#); [Bender 1988](#); [Jedrzejewski & Schechter 1988](#); [Franx et al. 1989](#); [Bertola et al. 1992](#)). Subsequent studies identified CR stellar disks in NGC 7217 ([Merrifield & Kuijken 1994](#)), NGC 3593 ([Bertola et al. 1996](#)), and NGC 4138 ([Jore et al. 1996](#)), confirming that the CR phenomenon is not unique to NGC 4550.

The next significant advance in the field came with the development and application of spectral decomposition techniques ([Chilingarian et al. 2011](#); [Coccatto et al. 2011](#); [Johnston et al. 2013](#); [Katkov et al. 2013](#)), which over the past decade have enabled the assessment of stellar population properties in many CR disk galaxies (Tab. 1). These studies indicate that the CR disk generally contains a younger stellar population that co-rotates with the ionized gas, while the main stellar disk is typically older. This suggests that CR stellar disks likely form in situ from externally acquired gas rather than through the accretion of ex situ stars during a merger. The metallicity of CR stars varies widely among galaxies, ranging from lower to comparable or even higher than that of the main disk. Several scenarios have been proposed to explain the formation of CR disks, including accretion from cosmic filaments ([Algorry et al. 2014a](#)), “wet” mergers with gas-rich dwarf galaxies ([Thakar & Ryden 1996a](#)), tidal gas exchange between neighboring galaxies ([Khim et al. 2021](#); [Sil’chenko et al. 2023](#)), and major merger events with finely tuned orbits that preserve the disk structure ([Puerari & Pfenniger 2001](#); [Crocker et al. 2009](#)). Lower metallicity is expected in CR disks formed from pristine gas accreted via cosmic filaments, whereas other mechanisms tend to result in higher metallicity since the externally accreted gas is already pre-enriched. However, the exact metallicity depends on both star formation and metal enrichment history. Although bar dissolution via separatrix crossing ([Evans & Collett 1994](#)) has also been proposed as an internal mechanism for the formation of CR disks, it cannot account for the observed differences in stellar populations – particularly the significant age differences between stellar components in many CR galaxies – and is therefore not considered here.

Massive spectroscopic IFU surveys, particularly SDSS-IV MaNGA ([Bundy et al. 2015](#)), which observed $\sim 10,000$ galaxies, have greatly advanced the studies of stellar CR and demonstrated that the phenomenon is not particularly rare. Several research teams identified numerous CR galaxies in MaNGA, suggesting that $\approx 1\%$ of its galaxies exhibit stellar CR ([Jin et al. 2016](#); [Gra-](#)

Table 1. CR disk galaxies studied by means of spectral decomposition technique

Studied CR Galaxy	Reference
NGC 5719	Coccatto et al. (2011)
IC 719	Katkov et al. (2013)
	Pizzella et al. (2018)
NGC 4550	Coccatto et al. (2013)
	Johnston et al. (2013)
NGC 3593	Coccatto et al. (2013)
NGC 4138	Pizzella et al. (2014)
NGC 4191	Coccatto et al. (2015)
NGC 448	Katkov et al. (2016)
NGC 1366	Morelli et al. (2017)
NGC 5102	Mitzkus et al. (2017)
SDSS J0748+4441 (PGC 21856)	Bao et al. (2024)
PGC 66551	Katkov et al. (2024b)

[ham et al. 2018](#); [Bao et al. 2022](#); [Bevacqua et al. 2022](#)). In this work, we perform a detailed search for, and analysis of, CR galaxies within the MaNGA survey using a different approach than past work. Our final selection of CR galaxies is based not only on the stellar and gas kinematic maps derived from MaNGA data but also on an analysis of the non-parametrically recovered stellar Line-Of-Sight Velocity Distribution (LOSVD), which allowed us to reliably detect CR galaxies even when the kinematic maps are unclear. For $\approx 1/3$ of the identified CR galaxies, we have also carried out spectral decomposition and assessed the stellar population properties in both the main and CR disks.

This paper is organized as follows. In Section 2, we describe the data used in this work and our visual inspection procedure. In Section 3, we present the workflow for analyzing the MaNGA data. In Section 4, we discuss the dichotomy and possible sources of accreted material in CR-galaxies. Throughout the paper, we adopt the WMAP9 cosmology with $H_0 = 69.3 \text{ km s}^{-1} \text{ Mpc}^{-1}$ and $\Omega_0 = 0.2865$ ([Hinshaw et al. 2013](#)).

2. SAMPLE CONSTRUCTION

2.1. Data

We performed a search for stellar counter-rotating galaxies using data collected by the MaNGA survey ([Abdurro’uf et al. 2022](#)) based on Integral Field Unit (IFU) spectroscopic ([Drory et al. 2015](#)) observations, conducted at the Sloan 2.5-m telescope ([Gunn et al. 2006](#)), of some 10,000 galaxies in the nearby Universe ($0.01 \lesssim z \lesssim 0.15$) covering a wide range of stel-

lar mass and colors (Wake et al. 2017). In the survey, each galaxy was observed using 2 arcsec fibers packed in bundles that vary in diameter from 12 arcsec (19 fibers) to 32 arcsec (127 fibers) covering $(1.5 - 2.5) \times$ the effective diameter of the target. Fiber bundles feed the BOSS spectrographs (Smeed et al. 2013), which provide wavelength coverage of $\lambda\lambda 3600\text{--}10300 \text{ \AA}$ with spectral resolving power $R \sim 2000$, corresponding to an instrumental dispersion $\sigma_{\text{inst.}} \approx 75 \text{ km s}^{-1}$ at 5100 \AA (Law et al. 2016). To fill in the gaps between the round fibers in a bundle, each galaxy was observed using 3 spatially dithered exposures (Law et al. 2015; Yan et al. 2016).

In our work, we also used the quantities reported in MaNGA value added catalogs (VACs) MaNGA-HI DR3 (Stark et al. 2021), GEMA-VAC (Argudo-Fernández M. et al. in prep.), and MaNGA Visual Morphology Catalogue (MVM-VAC), as well as the NASA-Sloan Atlas (Blanton et al. 2011; Wake et al. 2017) and the GALEX-SDSS-WISE Legacy Catalog (GSWLC) (Salim et al.

2016). MaNGA-HI DR3 was derived from an atomic hydrogen survey conducted using radio observations at the 21 cm wavelength collected at the single-dish Green Bank Telescope (GBT), complemented by the results of the ALFALFA survey (Haynes et al. 2018), and includes data for 6632 galaxies. The Galaxy Environment for MaNGA (GEMA) catalog contains environmental properties for MaNGA galaxies, based on the methods described by Argudo-Fernández et al. (2015); Etherington & Thomas (2015); Wang et al. (2016). Morphological classification of galaxies in MaNGA was taken from MVM-VAC (Vázquez-Mata et al. 2022). The GSWLC (Salim et al. 2016) combines data from the GALEX, SDSS, and WISE surveys and provides multi-wavelength properties for a wide range of galaxies.

2.2. Visual inspection

Table 2. Sample of reliable galaxies with stellar counter-rotation.

No.	ID	R.A.	Dec.	Type	$\log(M_*/M_\odot)$	z	Features	CR config.	Env.	Morph.
(1)	(2)	(3)	(4)	(5)	(6)	(7)	(8)	(9)	(10)	(11)
1	1-42660 [†]	01:52:44.4	13:11:33.18	SABab	10.27	0.026	2σ	outer	V, G	LSB
2	1-42247 [†]	02:14:21.1	14:07:06.73	Sab	9.71	0.029	2σ , Srot, CR-GS	inner	V, G	...
3	1-109056 [†]	02:37:47.2	00:24:18.31	SABa	10.41	0.047	2σ	outer	V, P, G	...
4	1-37062 [†]	02:47:23.1	00:03:31.52	SAB0a	10.19	0.025	2σ , CR-GS, Srot	inner	V, G	T, Sh
5	1-37068	02:48:47.6	-00:06:33.07	SAB0a	10.34	0.025	2σ , CR-GS, NRR	inner	V, G	...
6	1-37494 [†]	02:58:30.1	00:47:39.24	S0a	10.18	0.043	2σ	outer	V, P, G	...
7	1-37478 [†]	02:59:23.2	-01:10:00.07	S0	10.46	0.028	σ -elong.	inner	V, G	...
8	1-109275 [†]	03:04:17.0	00:31:11.59	SBa	10.05	0.044	2σ , CR-GS, Srot	inner	V, G	B
9	1-38543 [†]	03:36:07.8	-00:35:47.18	S0a	10.36	0.023	2σ , CR-GS	inner	V, G	E
10	1-297863 [†]	07:47:04.1	18:08:18.03	SAB0	10.25	0.045	2σ , NRR	inner	Cl, G	...
11	1-339061 [†]	07:48:34.6	44:41:17.83	SAB0a	10.32	0.020	2σ , CR-GS, Srot	inner	Sh, G, O	T, Sh
12	1-378729 [†]	07:52:04.2	50:07:50.96	S0	10.20	0.024	Gas-mis, 2σ	undef	Cl, G	...
13	1-44047 [†]	07:58:34.4	41:34:42.27	S0	10.22	0.041	2σ , Srot	outer	F, G, O	...
14	1-44483 [†]	07:59:20.4	42:03:25.46	S0a	10.12	0.025	2σ , Srot	outer	Sh, G, O	E, T
15	1-145913	08:00:53.2	28:07:49.42	Edc	9.85	0.017	Srot, CR-GS, $2\sigma?$	inner	F, G, O	...
16	1-382889 [†]	08:02:28.9	20:30:50.33	Sa	10.37	0.029	2σ , CR-GS, Srot	inner	Sh	E
17	1-121871 [†]	08:03:04.0	36:15:52.16	S0	10.11	0.044	2σ	inner	F, G, O	...
18	1-76425	08:47:18.6	02:45:44.20	Sab	10.61	0.028	2σ , CR-GS	outer	Cl, G	T, LSB
19	1-386322 [†]	08:56:51.3	27:16:12.37	S0a	9.94	0.019	2σ , Srot	outer	Sh, G, O	E
20	1-300092	09:00:47.5	29:59:25.02	Sa	10.74	0.054	CR-GS, Srot	outer	F, G	T, Sh
21	1-137890 [†]	09:08:52.6	44:55:56.16	Sb	9.89	0.027	2σ , CR-GS, Srot	inner	F, G, O	E
22	1-386932 [†]	09:11:22.7	30:05:47.15	Sa	9.87	0.026	2σ , CR-GS, NRR	inner	F, G	...
23	1-232087 [†]	09:30:53.9	35:26:23.23	SABa	10.28	0.028	2σ , Srot	outer	F, G	...
24	1-78381 [†]	09:52:00.7	04:09:02.77	Sa	10.96	0.031	2σ , Srot	outer	F, G	Sh
25	1-182730 [†]	10:18:23.6	05:44:10.06	S0	11.05	0.074	Srot, σ -elong.	inner	V, G	...
26	1-586725 [†]	10:24:07.7	00:08:30.96	SABa	10.37	0.023	2σ , CR-GS	inner	Sh, P, G	T, LSB, C
27	1-274545	10:30:44.6	40:03:26.79	S0a	9.69	0.023	2σ , Srot, CR-GS	unclear	F, G	...
28	1-255220	10:31:23.0	42:16:37.85	S0a	9.87	0.022	2σ , CR-GS, Srot	inner	F, G, O	E
29	1-148987 [†]	10:58:12.4	50:12:48.44	Sa	10.34	0.024	2σ	inner	Cl, G, O	E
30	1-188530 [†]	11:43:16.3	55:16:39.74	S0a	10.66	0.055	CR-GS, Srot	inner	F, O	E
31	1-174947 [†]	11:45:26.1	49:52:44.54	SBab	10.68	0.033	2σ , Srot	outer	F, G, O	B, Sp

Table 2 continued

Table 2 (continued)

No.	ID	R.A.	Dec.	Type	$\log(M_*/M_\odot)$	z	Features	CR config.	Env.	Morph.
(1)	(2)	(3)	(4)	(5)	(6)	(7)	(8)	(9)	(10)	(11)
32	1-139814	11:57:23.5	04:32:35.01	Sa	10.17	0.020	2σ	unclear	F, G	...
33	1-519907 [†]	11:58:34.7	24:07:01.77	Sb	10.09	0.030	2σ , gas-polar, NRR	outer	Sh, G	E, C
34	1-189376	12:04:03.4	55:12:17.69	S0	9.88	0.019	CR-GS, 2σ , Srot	inner	F, G	...
35	1-623416 [†]	12:57:53.9	28:29:59.25	S0a	10.16	0.024	2σ , Srot	outer	Cl, G	...
36	1-456884 [†]	12:58:19.2	27:45:43.54	Sa	9.54	0.018	2σ , Srot	inner	Cl, G	E
37	1-456672 [†]	13:00:19.1	27:33:13.37	SB0	10.13	0.020	2σ , Srot	outer	Cl, G	B, T
38	1-456645 [†]	13:03:05.9	26:31:52.02	SABa	9.96	0.019	2σ , NRR	outer	Cl, G	LSB
39	1-419257 [†]	13:24:33.7	31:32:46.96	SB0a	10.31	0.023	2σ , CR-GS, Srot	inner	F, G, O	B
40	1-457547	13:27:41.0	26:03:41.88	SABab	9.86	0.024	2σ	unclear	F, G, O	...
41	1-244115 [†]	13:38:01.5	55:11:15.52	Sa	10.14	0.025	2σ , CR-GS, NRR	inner	Cl, G	E
42	1-260823 [†]	13:53:10.0	40:07:09.11	S0	10.47	0.051	2σ , NRR	outer	Sh, G, O	...
43	1-245235 [†]	14:05:41.9	55:46:36.83	Sab	10.15	0.041	2σ , CR-GS, Srot	inner	F, G	...
44	1-245301 [†]	14:10:07.7	54:55:11.75	SABa	10.75	0.040	2σ , CR-GS	outer	Cl, G	LSB, Sh
45	1-593328 [†]	14:38:37.7	46:39:47.23	Sa	11.20	0.037	2σ , CR-GS, Srot	inner	Cl, G	...
46	1-13736 [†]	14:52:19.4	-00:16:09.14	S0	10.08	0.044	2σ , CR-GS, Srot	inner	Cl, G	...
47	1-566335	15:05:07.9	08:06:26.47	SABa	10.33	0.047	2σ , Srot	outer	F	...
48	1-333770	15:05:13.6	08:47:47.79	Edc	11.06	0.045	2σ , Srot	unclear	F, G	T, Sh
49	1-633000 [†]	15:32:55.7	42:26:17.72	SAB0	10.06	0.020	2σ , CR-GS, Srot	inner	Cl, G, O	...
50	1-199775	16:03:23.5	39:59:08.68	S0	10.22	0.030	2σ , CR-GS, NRR	inner	F, G	...
51	1-210611 [†]	16:17:33.7	41:41:18.76	SAB0	10.30	0.027	CR-GS, σ -elong.	inner	F, G, O	...
52	1-248869 [†]	16:18:45.8	39:20:04.01	S0a	10.85	0.032	2σ , CR-GS	outer	F, G, O	...
53	1-323764	16:24:13.0	31:52:33.09	Sbc	9.71	0.021	2σ , NRR	unclear	V, G, O	...
54	1-135190 [†]	16:27:00.8	40:48:37.89	S0	10.47	0.030	CR-GS, σ -elong.	inner	Cl, P, G	...
55	1-135503	16:31:31.7	39:53:51.55	Sa	10.72	0.030	2σ , star-polar	undef	Cl, G, O	Sh, P
56	1-94773 [†]	16:37:12.6	44:05:07.84	SB0a	10.18	0.033	2σ , CR-GS	inner	F, G, O	B
57	1-211561 [†]	16:40:46.8	37:02:31.32	Sa	10.27	0.030	2σ , CR-GS, NRR	inner	F, G	...
58	1-135767 [†]	16:40:55.1	37:54:15.54	Sab	10.55	0.031	2σ , Srot	outer	F, G	LSB, Sh, Sp
59	1-94690 [†]	16:45:30.7	43:34:53.91	S0a	10.22	0.031	2σ , CR-GS	inner	F, G, O	E
60	1-136248 [†]	16:55:10.5	36:54:22.72	Sa	10.52	0.024	2σ , Srot	outer	F, G	...
61	1-178027 [†]	17:14:58.2	29:08:18.57	SABab	10.44	0.045	2σ , CR-GS	outer	F, O	LSB, C, Sp
62	1-635506 [†]	21:16:24.8	10:16:24.19	SB0	10.21	0.017	CR-GS, 2σ	inner	V, G	B
63	1-179561 [†]	21:19:00.3	-00:57:50.37	S0	10.09	0.020	2σ , CR-GS, Srot	inner	V, P, G	C
64	1-26197 [†]	22:02:53.7	-00:47:04.57	S0a	10.93	0.064	2σ , CR-GS, Srot	outer	V, G	...
65	1-115097 [†]	22:08:48.8	13:21:53.06	Sab	10.23	0.027	2σ , CR-GS, Srot	inner	V, G	E

NOTE: Column (1) lists the sequential number of galaxy. (2) is the MaNGA ID of the galaxy. In the e-version, the ID contains a hyperlink to the galaxy page in the interactive visualizer service <https://manga.voxastro.org>. Symbol † marks galaxies with a clear X-shape in the non-parametric LOSVD (Sec. 3.2). Galaxies with bold IDs were upgraded from the probable to the reliable category after LOSVD inspection. (3) and (4) are sky coordinates. (5) morphological type from MVM-VAC. (6) contains the stellar mass from NSA, corrected to the adopted H_0^2 . (7) is the redshift from MaNGA-DAP. (8) is the categories assigned during our visual inspection (Sec. 2.2). (9) an inner or outer kinematic configuration of the CR-disk (Sec. 4.1), “unclear” cases refer to galaxies where classification is not possible based on kinematic maps or LOSVD analysis, and “undef” where the CR disk is out of the main galactic plane. (10) provides environmental galaxy properties from the GEMA-VAC (**P** — Pair, **G** — Group, **O** — Overdensity, **Cl** — Cluster, **Sh** — Sheet, **F** — Filament, **V** — Void). (10) includes the morphological features from the MVM-VAC (**B** — Bar, **E** — Edge-on, **T** — Tidal) and from our visual inspection (**LSB** — LSB outskirts, **Sh** — Shells/tails, **C** — Near companion/cluster, **Sp** — Spirals, **P** — Polar structure).

To identify galaxies with CR disks, we visually inspected the Data Analysis Products (DAP) maps (Westfall et al. 2019; Belfiore et al. 2019; Law et al. 2021) of

the stellar velocity, gas ($H\alpha$) velocity, and stellar velocity dispersion of all MaNGA galaxies. Galaxies possibly exhibiting kinematic misalignment features associated with CR disks were identified and attributed to one of the following types (Fig. 1) by the following criteria:

- 2σ (132 galaxies) — characterized by two symmetrically positioned off-centered peaks in the stellar

Table 3. Sample of **probable** galaxies with stellar counter-rotation. The column descriptions are provided in the Tab. 2.

No.	ID	R.A.	Dec.	Type	$\log (M_*/M_\odot)$	z	Features	CR config.	Env.	Morph.
(1)	(2)	(3)	(4)	(5)	(6)	(7)	(8)	(9)	(10)	(11)
1	1-600853	00:31:12.1	-00:24:26.48	Sa	10.35	0.019	$2\sigma?$, CR-GS, KDC	inner	V, G	...
2	1-40771	01:11:08.3	14:13:22.11	Sa	11.20	0.054	$2\sigma?$, CR-GS, Srot	unclear	V, G	T, Sh
3	1-41072	01:21:36.3	14:27:10.34	SABa	10.65	0.052	CR-GS, Srot	unclear	V, G	T, Sh
4	1-34036	01:25:29.1	-00:03:26.30	S0	9.84	0.021	CR-GS, Srot, $2\sigma?$	inner	V, G	...
5	1-41752	02:07:48.7	13:36:34.54	Sa	10.87	0.065	2σ , CR-GS	inner	V, G	T, Sh
6	1-38062	03:16:54.9	-00:02:31.23	S0	10.20	0.023	2σ , Srot	unclear	V, G	...
7	1-217842	07:50:40.8	23:29:39.55	S0	10.35	0.019	CR-GS, 2σ	inner	Sh, G	...
8	1-382697	07:56:49.8	17:22:49.09	S0	10.56	0.036	CR-GS, $2\sigma?$	inner	Sh, G	E
9	1-382818	07:59:43.3	18:28:03.84	Sb	9.95	0.038	2σ , CR-GS	inner	Sh, P, G, O	B
10	1-153127	08:03:13.3	33:07:56.42	Sab	9.81	0.018	2σ , CR-GS	unclear	Cl, G	LSB
11	1-298482	08:10:12.2	22:46:20.22	SABa	9.57	0.016	CR-GS, $2\sigma?$	inner	Cl, P, G	...
12	1-386154	08:54:18.0	26:30:22.03	SB0a	9.93	0.027	2σ , CR-GS	inner	Sh, G, O	B
13	1-77006	09:02:21.2	03:36:56.66	S0	10.03	0.024	2σ , CR-GS	unclear	V, G	...
14	1-386394	09:02:46.6	29:17:17.66	Sa	9.94	0.042	CR-GS, $2\sigma?$	unclear	Sh, P, G	...
15	1-166613	09:38:03.8	42:58:27.56	S0a	11.07	0.047	Srot	unclear	F, G, O	...
16	1-181720	09:44:21.9	06:04:31.71	Sa	10.90	0.062	Srot, σ -elong.	unclear	Cl, G	T, C
17	1-167079	09:51:12.4	44:00:33.51	Sab	9.51	0.016	2σ	unclear	V, G, O	...
18	1-78858	10:06:02.2	04:31:19.69	S0a	10.20	0.023	CR-GS, $2\sigma?$	inner	F, G	...
19	1-274440	10:22:50.1	39:22:08.19	S0	9.55	0.026	2σ	unclear	F, G, O	...
20	1-255878	10:52:52.6	43:25:42.26	S0	10.02	0.024	CR-GS, NRR?, $2\sigma??$	inner	Cl, P, G, O	T, LSB
21	1-277289	11:01:06.0	45:17:35.91	S0a	9.86	0.037	2σ	unclear	Cl, G, O	E
22	1-279554	11:26:30.8	46:59:54.36	SB0a	10.43	0.025	$2\sigma?$	unclear	F, G, O	B, E
23	1-174429	11:33:23.0	49:02:16.96	Sc	10.11	0.031	2σ	outer	Cl, G, O	E
24	1-188177	11:44:31.1	53:40:57.79	S0a	10.30	0.027	CR-GS, 2σ	inner	F, P, G, O	...
25	1-189197	11:47:46.6	55:23:24.07	S0	10.15	0.026	2σ , NRR	unclear	Sh, G, O	...
26	1-280716	11:49:35.2	47:49:52.40	S0	10.39	0.025	Srot, 2σ	unclear	F, G	...
27	1-281935	12:12:31.6	43:22:01.34	Sbc	9.68	0.024	$2\sigma??$, NRR??	unclear	F, G	...
28	1-151418 [†]	12:27:58.0	53:02:34.21	Sab	10.04	0.030	CR-GS, $2\sigma?$	unclear	F, G	LSB, Sh
29	1-283130	12:36:14.4	42:38:12.27	S0a	9.83	0.028	2σ , Srot	unclear	Sh, G	...
30	1-456775	12:56:06.4	27:38:52.89	S0a	10.05	0.025	$2\sigma?$	unclear	Cl, G	E
31	1-152010	12:57:48.8	52:46:45.36	Sa	9.72	0.028	CR-GS, 2σ	inner	F, G	...
32	1-456731	12:58:00.8	27:27:14.29	S0	9.65	0.026	Srot, KDC?	unclear	Cl, G	...
33	1-284335	13:07:17.0	45:43:41.35	S0a	9.71	0.035	2σ , CR-GS	inner	F, G, O	E
34	1-421145	13:23:42.8	31:30:55.71	S0	10.10	0.018	2σ , Srot, KDC?	unclear	F, P, G, O	E
35	1-523154	13:38:23.3	23:58:19.72	S0a	10.20	0.028	CR-GS, 2σ	inner	F, G, O	...
36	1-418253	13:44:37.0	37:10:17.87	SB0	10.50	0.027	CR-GS, σ -elong.	unclear	F, G, O	B, T, Sh
37	1-537081	13:47:47.7	23:22:02.05	S0a	11.03	0.084	2σ , NRR	unclear	Cl, G	T, Sh
38	1-251198	13:58:33.5	41:43:27.06	Sab	10.10	0.043	2σ , CR-GS	inner	V, G, O	E
39	1-245176	13:59:35.4	55:35:33.12	Sa	10.16	0.041	2σ , NRR	unclear	F, G	Sh
40	1-251783	14:21:14.8	39:39:09.12	E	10.18	0.026	Srot, $2\sigma??$	unclear	F, G, O	...
41	1-266244	14:26:11.2	42:42:40.47	S0a	9.22	0.017	$2\sigma?$, Srot	unclear	F, G, O	T, LSB
42	1-235983	14:54:32.8	42:23:07.60	S0	9.79	0.018	gas-polar, Srot, KDC?	unclear	F, G, O	...
43	1-246484	14:55:27.9	51:02:51.85	S0a	9.72	0.030	gas-polar, 2σ	unclear	F, G, O	E
44	1-134361 [†]	16:00:53.7	47:11:49.26	Sa	10.42	0.046	2σ	outer	Sh, G	E
45	1-248410	16:04:50.0	42:02:08.91	Sa	9.59	0.025	2σ , NRR?	outer	F, G, O	E
46	1-318513	16:16:08.6	24:04:46.30	S0a	9.84	0.032	2σ	outer	Cl, G, O	E
47	1-323886	16:20:34.0	32:56:05.74	Sab	10.03	0.041	2σ	outer	Sh, G, O	E
48	1-323766	16:24:42.2	32:03:51.74	E	9.88	0.022	CR-GS, Srot, σ -elong.	inner	V, G, O	...
49	1-543599 [†]	16:41:07.3	26:03:39.05	Sab	10.60	0.055	$2\sigma?$	outer	F, G	...
50	1-113405	21:07:21.9	11:03:59.11	Sa	10.11	0.042	2σ , CR-GS	inner	V, G	E
51	1-635590 [†]	21:24:13.1	01:07:06.18	S0	11.22	0.049	2σ , NRR?	unclear	V, G	...
52	1-180900	21:41:28.6	00:36:29.67	Edc	10.73	0.055	2σ , Srot	unclear	V, G	...
53	1-106664	23:09:02.9	00:16:01.05	SBbc	10.16	0.033	2σ	unclear	V, G	B, E, T, Sh
54	1-29728	23:43:18.0	00:26:32.91	Sab	9.87	0.037	CR-GS, 2σ	unclear	V, G	E
55	1-29809	23:53:52.5	-00:05:55.43	S0a	9.56	0.022	$2\sigma?$, CR-GS, Srot?	inner	V, G	...

velocity dispersion map aligned along the major axis of the galaxy. This apparent structure results from modeling two stellar populations with distinct kinematics with a single spectral component (Krajnović et al. 2011; Rubino et al. 2021);

- σ -elongated σ -*elong.* (11 galaxies) — analogous to the 2σ type, but characterized by an elongated peak along the major axis observed in the stellar velocity dispersion map, formed by the merging of the two velocity dispersion peaks;
- S-rotation *Srot* (58 galaxies) — characterized by a change in the direction of stellar rotation between the inner and outer regions of the galaxy. So named because the stellar velocity profile along the major axis has a “S” shape;
- Non Regular (irregular) Rotation *NRR* (24 galaxies) — disk galaxies with stellar velocity maps that do not indicate regular rotation;
- Gas / Star Counter Rotation *CR-GS* (207 galaxies) — galaxies in which the gas and stars have different rotation patterns, as indicated by comparing their velocity maps. For galaxies with a prominent S-shaped rotation, the gas velocity map is compared to the outer regions of the stellar velocity map;
- *Gas-polar* (119 galaxies) — characterized by the major kinematic axis of the stellar velocity field being perpendicular to that of the gas velocity field;
- Gas misalignment *Gas-mis* (173 galaxies) — where the kinematic major axes of stellar and gas velocity fields are misaligned but neither perpendicular nor counter-rotating;
- *Star-polar* (2 galaxies) — the rare case where the stellar velocity map reveals a polar structure, typically associated with a morphological feature in the polar direction relative to the main disk, as detected in DECaLS images;
- Kinematically Decoupled Core *KDC* (8 galaxies) — galaxies with a physically small, kinematically distinct region in the central part of the galaxy (Efsthathiou et al. 1982); and
- *Other* (7 galaxies) — galaxies that exhibit irregular kinematics that does not fit into the above categories.

All the types mentioned above were initially identified through visual inspection without supplementary validation via non-parametric LOSVD analysis (Sec. 3.2). Therefore, this preliminary classification may not be perfect and minor variations in types may be present.

In total, we identified 588 unique galaxies exhibiting some form of kinematical misalignment, including some galaxies that could fit in multiple categories. We omitted clear cases of violent ongoing mergers involving decoupled stellar and gaseous subsystems in an unrelaxed state. While these systems could be studied with our methods (Mazzilli Ciraulo et al. 2021), they are beyond the scope of this work.

Our primary goal during the inspection was to identify galaxies with stellar CR. Therefore, we focused on the $2\sigma/\sigma$ -elongated, *Srot*, and *CR-GS* galaxies. However, due to the limited field of view of MaNGA observations, occasionally poor signal-to-noise ratio (SNR), an effective spatial resolution of ≈ 2.5 arcsec, for some cases we are uncertain of the presence of kinematic features (indicated by “?” in the feature type). The 66 galaxies where this was true are considered *probable* CR galaxies, with the other 49 in the galaxy types mentioned above being *reliable* CR galaxies. During the inspection process, we extensively used our web-based interactive service for the visualization of MaNGA data (<https://manga.voxastro.org>¹).

We then carried out a non-parametric analysis of the stellar LOSVD (see details in Sec. 3.2) for the complete sample of kinematically misaligned galaxies (588 galaxies). As expected, most reliable CR galaxies exhibited clear X-shaped structures in the position-velocity diagrams, suggesting two counter-rotating stellar disks (35 galaxies). Furthermore, we identified clear X-shaped structures in 15 probable CR candidates, which were subsequently reclassified into the reliable category (bold IDs in Tab. 2). Moreover, we found five galaxies in the total sample of kinematically misaligned galaxies that did not show obvious features in the kinematic maps but exhibited a possible X-shape in LOSVD diagrams. Of these, we added four to the probable CR category and reclassified one galaxy with the most noticeable X-shaped LOSVD (1-37478) into the reliable category. In summary, our sample now consists of 65 reliable and 55 probable stellar CR galaxies. The main properties of these galaxies are presented in Tab. 2 and 3. Fig. 2 shows the distributions of these galaxies across the Color-Magnitude Diagram (CMD) and star formation rate (SFR) — stellar mass diagram. Fig. 3 and 4 present color images and kinematic maps for our sample of CR galaxies.

The MVM-VAC includes 3576 early-type galaxies (ETGs; E, S0, and S0a) and 5720 late-type galaxies

¹ <https://manga.voxastro.org> is our first prototype service for the visualization of IFU data. <https://ifu.voxastro.org> (Katkov et al. 2024a) is the next generation of the service in the early stage of development which includes data from other spectroscopic surveys (SAMI, Califa, Atlas3D).

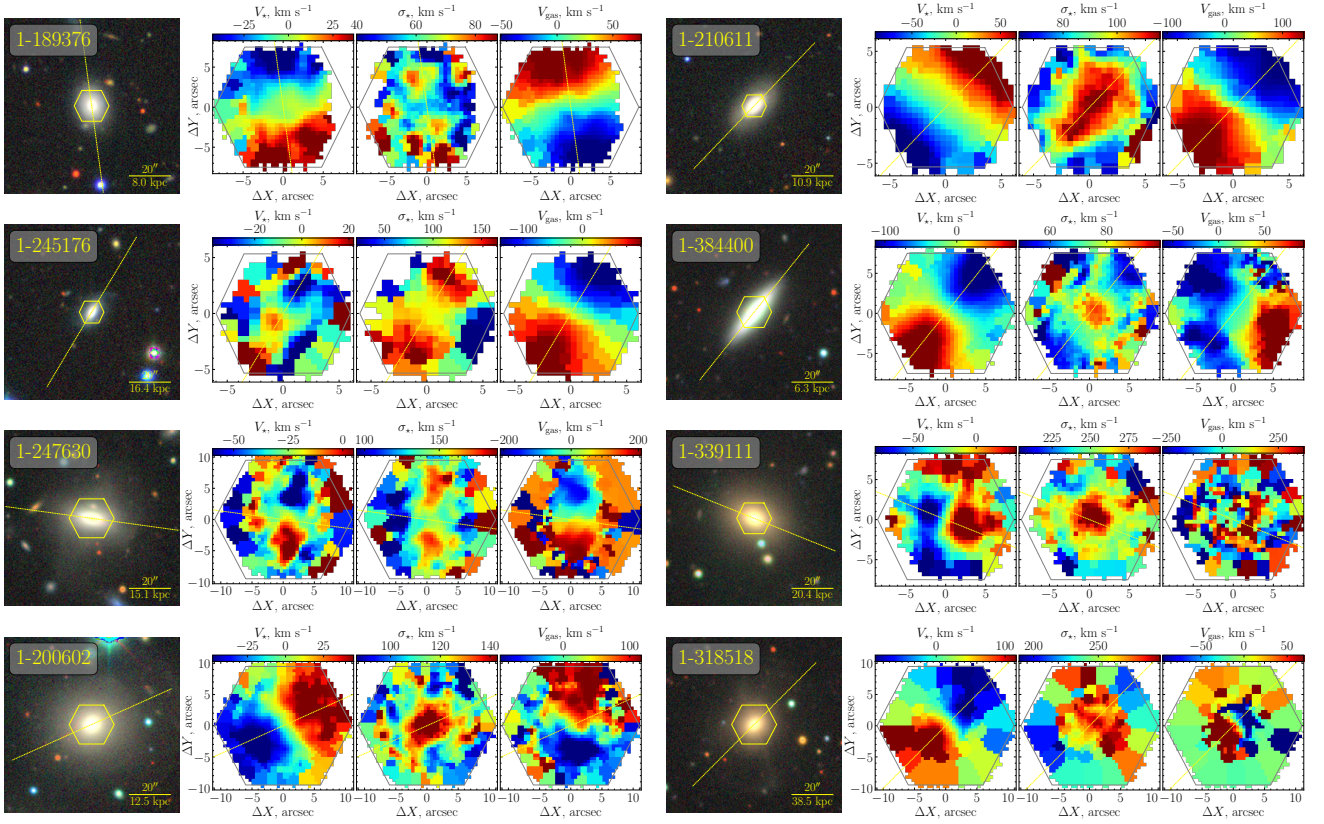


Figure 1. Eight examples of different types of kinematic misalignment. Each individual panel shows a composite RGB image of the galaxy taken from the Legacy Imaging Surveys (Dey et al. (2019), legacysurvey.org), kinematic maps are taken from MaNGA-DAP (stellar velocity V_* , dispersion of stellar velocity σ_* , and $H\alpha$ gas velocity V_{gas}), hexagon shows MaNGA FoV, dashed line lies along the major axis (by the position angle from the NSA catalog). From left to right, from top to bottom: **1-189376** — 2σ , Srot, CR-GS; **1-210611** — CR-GS, σ -elong.; **1-245176** — 2σ , NRR; **1-384400** — gas-polar; **1-247630** — 2σ , star-polar, gas-polar; **1-339111** — KDC; **1-200602** — Gas-mis; **1-318518** — other.

Table 4. Percentage of CR galaxies and those exhibiting any type of kinematic misalignment (All) across different morphological types. The “MaNGA” columns contain fractions relative to the corresponding morphological type in the entire MaNGA survey. The “Corr.” columns present volume-corrected fractions as derived in the MVM-VAC (Vázquez-Mata et al. submitted). The numbers in parentheses indicate the corresponding number of galaxies (targets with “Unsure” classification and irregular or “no classification” morphology were filtered out).

	S0/S0a (1797)		ETG (3576)		LTG (5720)		Total (9296)	
	MaNGA	Corr.	MaNGA	Corr.	MaNGA	Corr.	MaNGA	Corr.
CR (120)	3.1% (56)	2.9%	1.7% (61)	1.5%	0.8% (48)	0.8%	1.2% (109)	1.0%
All (588)	12.9% (231)	11.9%	10.6% (379)	7.9%	3.1% (178)	3.0%	6.0% (557)	4.9%

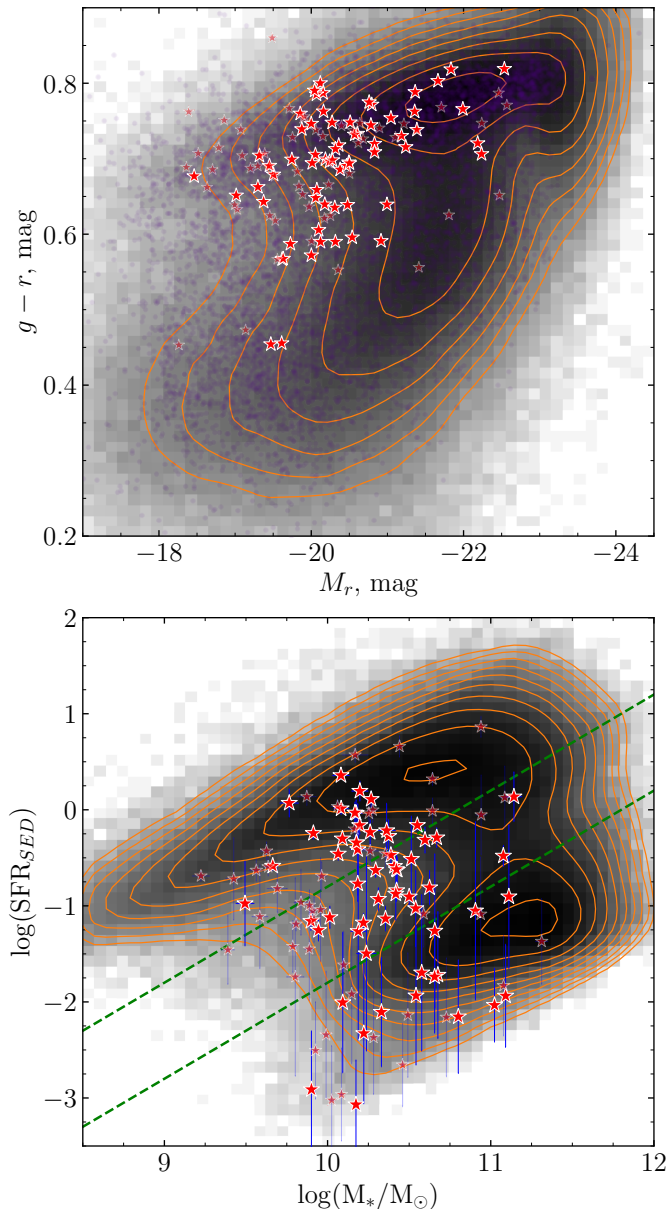


Figure 2. Top: Color-magnitude diagram for CR sample overlaid on a background computed from the RCSED catalog (rcsed.sai.msu.ru, [Chilingarian et al. 2017](#)). All MaNGA galaxies were cross-matched with the RCSED and are plotted as transparent purple dots. **Bottom:** M_* -SFR diagram with the CR galaxies. GSWLC catalog ([Salim et al. 2016](#)) was used to construct the grey background. The top and bottom green dashed lines correspond to specific star formation rates (sSFR) of $\log \text{sSFR} = -10.8 \text{ yr}^{-1}$ and $\log \text{sSFR} = -11.8 \text{ yr}^{-1}$, respectively. For both panels, the bright red stars denote the reliable CR sample (Tab. 2), while small red stars indicate the probable sample (Tab. 3).

(LTGs; Sa–Sm). Among them, 61 galaxies with stellar CR are classified as ETGs, accounting for $\approx 1.7\%$ of all ETGs and $\approx 3.1\%$ of S0/S0a galaxies. 48 CR galaxies are classified as LTGs, representing $\approx 0.8\%$ of all LTGs. The relatively high number of LTGs with stellar CR is not surprising, as many are Sa/Sab types that may be misclassified and share properties with ETGs. Considering the full sample of galaxies with kinematic misalignments, there are 379 ETGs ($\approx 10.6\%$, $\approx 12.9\%$ of S0/S0a galaxies), and 178 LTGs ($\approx 3.1\%$, primarily Sa/Sab/Sb types). These fractions, along with those adjusted for volume correction following Vázquez-Mata et al. (submitted, priv. comm.) are listed in Tab. 4. Galaxies classified as *unsure* and with a “T-type” code over 10 (Irregular and No classification) in MVM-VAC were excluded from the analysis. Several galaxies in the CR sample exhibit both stellar CR disks and bars. Some of these (1-178027, 1-245301, 1-298482, and 1-94773) have close companions that may induce bar-forming instabilities ([Izquierdo-Villalba et al. 2022](#)). In other cases (1-174947, 1-386154, 1-633000, and 1-635506), the mechanism responsible for bar formation remains unclear.

3. ANALYSIS

We examined the MaNGA spectra of all identified CR galaxies using a workflow similar to the one we previously used for detailed investigations of CR galaxies IC 719 ([Katkov et al. 2013](#)), NGC 448 ([Katkov et al. 2016](#)), and PGC 66551 ([Katkov et al. 2024b](#)). Hereafter, we present the details of our analysis.

3.1. Single-component full-spectrum fitting

The first step in analyzing the spectra of CR galaxies is single-component full-spectrum fitting using simple stellar population (SSP) models. We used the full spectral fitting package NBURSTS ([Chilingarian et al. 2007a,b](#)), which models the entire galaxy spectrum by effectively extracting the information encoded within an absorption-line spectrum. We used a grid of synthetic SSP models E-MILES ([Vazdekis et al. 2016](#)). The model spectrum was broadened by convolving it with the Gaussian stellar LOSVD. To account for discrepancies between the model spectrum and the observed spectrum due to imperfect calibration and dust extinction, we applied a multiplicative polynomial continuum represented by Legendre polynomials of the 19th degree. The model also includes a set of strong emission lines ($H\gamma$, $H\beta$, $[O III]$, $[O I]$, $[N II]$, $H\alpha$, $[S II]$) represented by a common parametric Gaussian LOSVD profile independent of stellar kinematics. These emission lines are treated as additive components, and their fluxes are determined by solving a constrained linear problem at each step of a non-linear minimization loop. Both emission line templates and SSP models were pre-convolved with the wavelength-dependent instrumental resolution prior to the main minimization process.

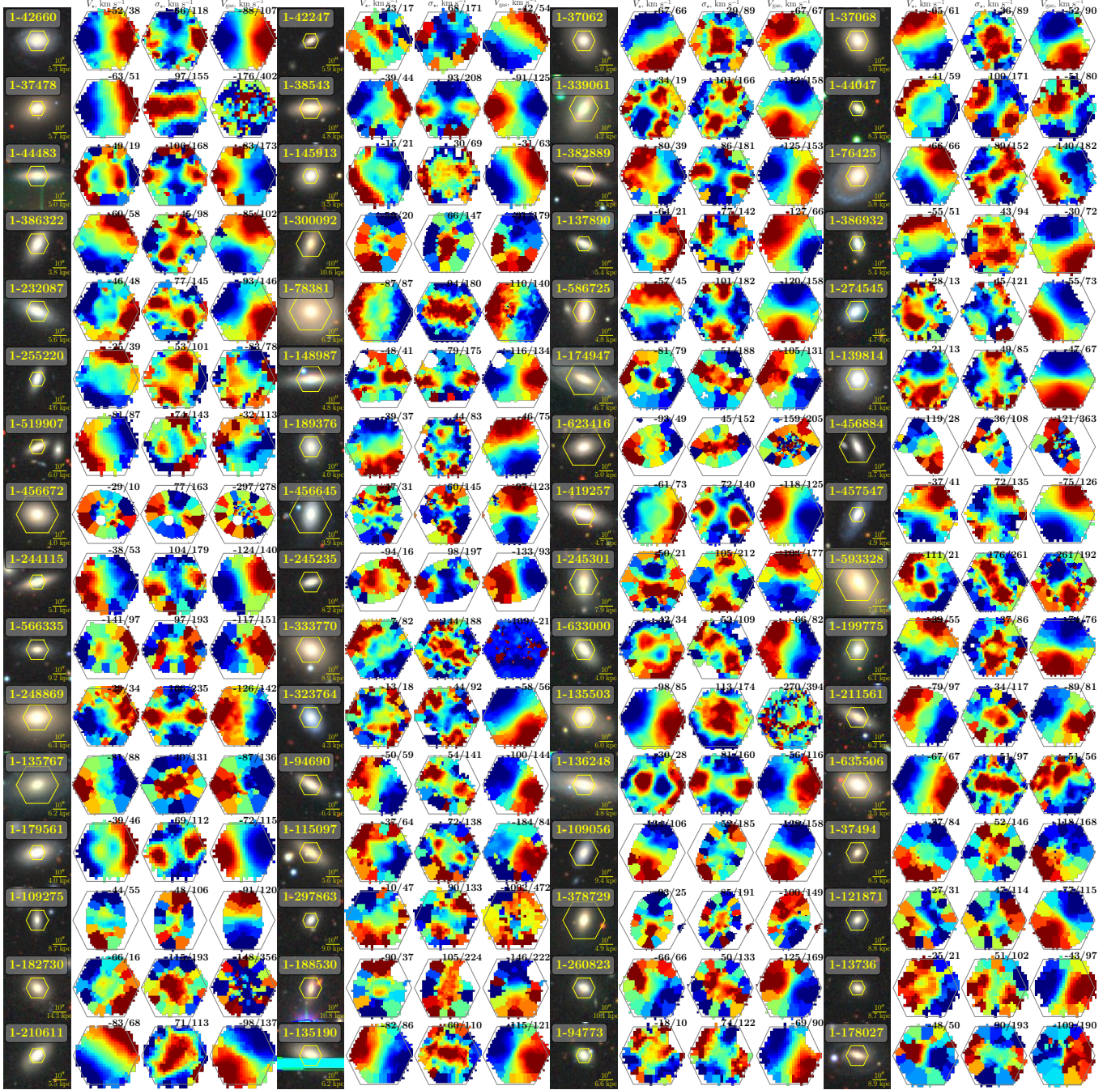


Figure 3. Sample of galaxies with reliable CR. The panel description is similar to Fig. 1. Numbers in the upper right corner of the maps indicate the minimum (blue) and maximum (red) values of the corresponding parameter.

We used these results to construct maps of the gas and stellar kinematics that include velocity and velocity dispersion. Additionally, we built maps of SSP-equivalent estimates of stellar population ages and metallicities, along with emission line flux maps for all galaxies in the sample that exhibit kinematic misalignment. To ensure consistency, we compared the derived kinematic maps with those provided in the DAP and confirmed the presence of kinematic misalignment in all selected galaxies.

3.2. Non-parametric stellar LOSVD analysis

To reveal the characteristic X-shaped stellar LOSVD indicative of CR disks, we applied the non-parametric LOSVD recovery approach successfully used in our previous studies (e.g., Katkov et al. 2016; Kasparova et al. 2020; Katkov et al. 2024b) which is described in detail by Gasymov & Katkov (2024). The properties of these X-shaped LOSVDs serve as a reliable initial estimate for

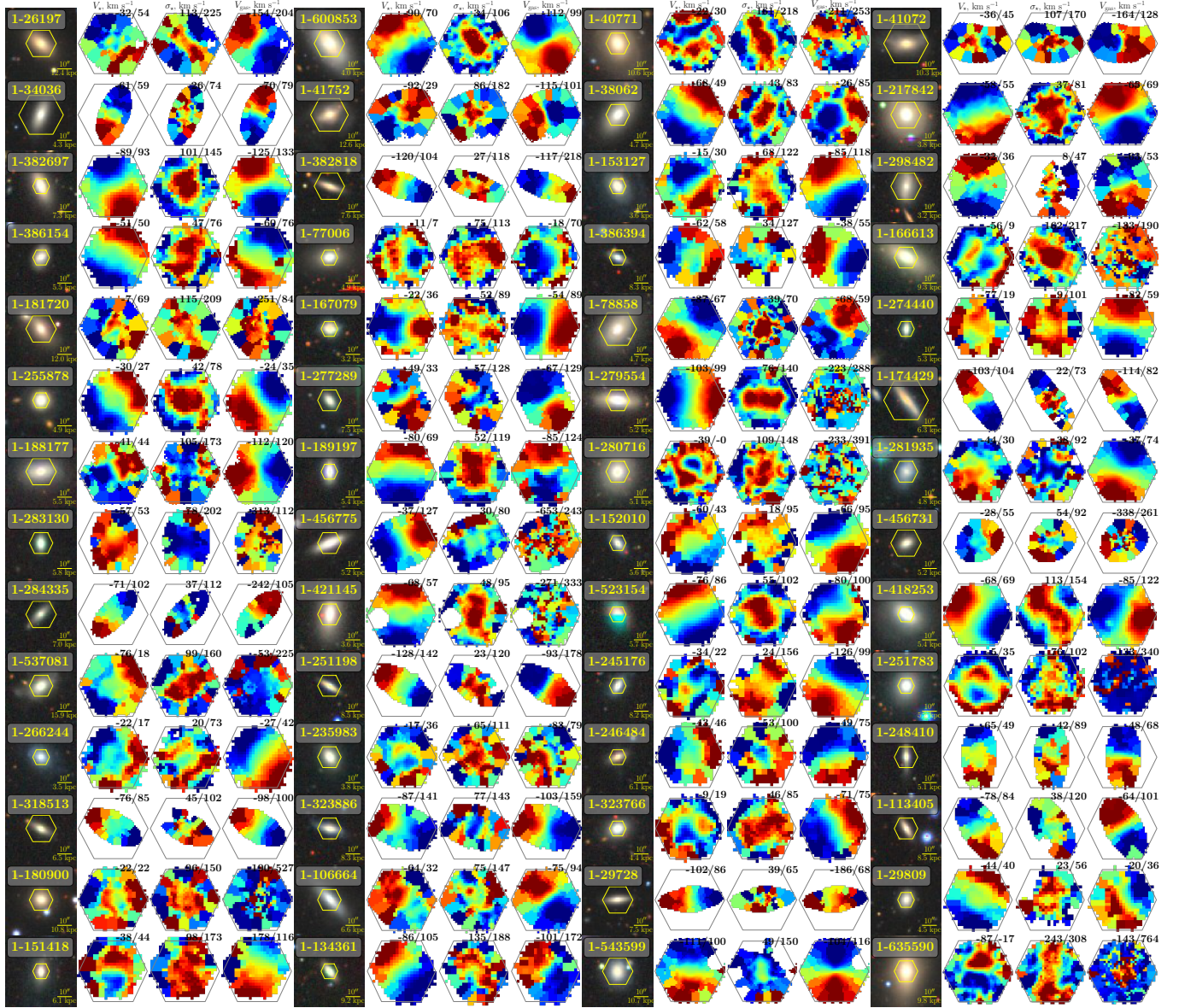


Figure 4. Same as Fig. 3, but for the probable sample of CR galaxies.

the kinematical parameters required for spectral decomposition.

The stellar spectrum of a galaxy, obtained as the difference between the observed and the emission line spectra, logarithmically binned in wavelength, can be modeled as the convolution of a high-resolution stellar population template with the stellar LOSVD. In our approach, we treat the deconvolution problem as an ill-posed linear problem whose solution is the desired LOSVD. We solve this problem using a linear least-squares method with L2 (Tikhonov) and “tail” regularization. The L2 regularization enforces smoothness in the LOSVD solution with different regularization coefficient settings: “weak” ($\lambda \sim 0.01$), “medium” ($\lambda \sim 0.2 - 0.3$), and “strong” ($\lambda \sim 4 - 5$), which encompass models with varying degrees of the influence of the

regularization on the solution. The “tail” regularization minimizes artifact peaks away from the systematic velocity. As a template, we used the unbroadened best-fit model of stellar population from the single-component fitting described in Sec. 3.1.

Instead of directly computing the full LOSVD, we reformulate the problem by expressing the solution as the sum of a predefined, peak-like LOSVD component and a minor correction vector. We then perform a linear least-squares fit to determine the correction vector, applying regularization to ensure its smoothness. In our iterative procedure, we start with an initial Gaussian LOSVD (obtained from single-component fitting) and, in subsequent iterations, use the full solution from the previous step as the fixed, predefined component.

Our method is provided as a Python package `SLA`². Additionally, a similar approach based on the Bayesian method for non-parametric stellar LOSVD recovery, `BAYES-LOSVD` by [Falc3n-Barroso & Martig \(2021\)](#), is also publicly accessible.

Following this analysis, we then determined the LOSVD for each spatial bin, yielding a three-dimensional model of the galaxy’s stellar kinematics (X-Y-V) from the IFU spectral cube. To facilitate subsequent analyses, we extracted a position-velocity (PV) diagram along the galaxy’s major axis in a 1 arc-sec pseudo-slit using `PVEXTRACTOR`³ ([Ginsburg et al. 2016](#)). We then modeled the LOSVD within the position-velocity coordinate frame.

Applying this analysis to the entire sample of galaxies with kinematical misalignment, we determined that although galaxy 1-37478 lacks clear CR features (first column in the second row of Fig. 3), it shows a clear X-shaped signature in the LOSVD (right column in the penultimate row of Fig. 5), indicating the presence of two counter-rotating components. Additionally, we up-ranked 15 galaxies from “probable” to “reliable” status based on their clear recovered X-shape LOSVDs. Four galaxies (1-151418, 1-134361, 1-543599, 1-635590) have noisy LOSVD patterns resembling an X-shape, though without strong symmetry. These galaxies were added in “probable” classification, with an additional note of potential CR disk presence.

Following this inspection, 51 out of the 120 galaxies in our CR sample exhibited clear X-shaped recovered LOSVDs within the MaNGA Field-of-View (the central panels of Fig. 5). These galaxies were chosen for further analysis of the recovered LOSVD to obtain kinematics and relative luminosity weights of both disks. We assumed that at any given position R the LOSVD could be parameterized by two Gaussians. These Gaussians are characterized by velocity dispersion (σ), intensity (I), and the velocity (v), which depend on the radial position R . Velocity v and velocity dispersion σ profiles are parametrized as follows:

$$v(R) = v_{\max} (\tanh(\pi|R|/R_0) + c|R|/R_0), \quad (1)$$

$$\sigma(R) = \max\{\sigma_0, \sigma_1 - k|R|\}, k > 0. \quad (2)$$

The fluxes of both disks were described by the standard disk exponential law ([Freeman 1970](#)):

$$I_i(R) = I_{0,i} \exp(-|R|/h_i). \quad (3)$$

By definition, the LOSVD is normalized to unity within each radial bin R . Therefore, we encountered a challenge due to degeneracy between the disk scale lengths h_i and their central intensities $I_{0,i}$. To break this degeneracy,

we simplified the analysis to fit only two parameters: the relative intensity $I_0 = I_{01}/I_{02}$ and the relative scale $h_0 = \frac{h_1 h_2}{h_1 - h_2}$. Utilizing these parameters, we computed the relative weight profiles within each radial bin of the LOSVD:

$$W_1(R) = \frac{I_1(R)}{I_1(R) + I_2(R)} = \frac{1}{I_0 \exp(-|R|/h_0) + 1}, \quad (4)$$

$$W_2(R) = 1 - W_1(R). \quad (5)$$

However, using only these two parameters does not allow us to determine the total weight of the counter-rotating disk W_{CR} . To compute this parameter, we introduced the total weight of the disk as defined by the following equation:

$$W_{\text{CR}} = \frac{\int I_{\text{CR}} R dR}{\int I_{\text{CR}} R dR + \int I_{\text{m}} R dR} = \frac{1}{1 + I_0 (h_{\text{CR}}/h_{\text{m}})^2}. \quad (6)$$

This formulation implies that we need to determine the relative intensity I_0 and the scale h_0 , along with at least one physical scale, either h_{CR} or h_{m} . We multiplied the model profiles $W_i(R)$ by the flux measured along the slice in the SDSS g -band MaNGA intensity map and fitted the resulting profiles with exponential laws $I_i(R)$ (Eq. 3) using the I_0 and h_0 parameters obtained from kinematic analysis. Finally, we recalculated the $I_{0,i}$ and h_i parameters to derive W_{CR} . These steps are illustrated in Fig. 6.

One limitation of our LOSVD reconstruction method is its reliance on a single stellar template to recover the complex LOSVD shape formed by two distinct stellar disks. The analysis assumes that both stellar components have similar stellar population properties, allowing them to be accurately represented by the same template. However, if this assumption does not hold, it may introduce distortions in the recovered LOSVD. We estimate that our analysis has a detection sensitivity threshold of approximately 10% in terms of luminosity weight, consistent with the detection limits reported by [Kuijken et al. \(1996\)](#); [Pizzella et al. \(2004\)](#); [Rubino et al. \(2021\)](#).

3.3. Two component full-spectrum fitting

LOSVD analysis provided precise estimates of the kinematics and weights for both disks, which we used as priors for a two-component SSP fitting using the NBURSTS technique. This method, known as spectral decomposition ([Chilingarian et al. 2011](#); [Coccatto et al. 2011](#); [Johnston et al. 2013](#); [Katkov et al. 2013](#)), was previously applied for several CR galaxies shown in Tab. 1. The essence of this approach is that the observed galaxy spectrum is modeled as a combination of two SSPs with individual properties, each convolved with an independent Gaussian LOSVD and assigned a free relative weight.

The quality of spectral decomposition depends on SNR, spectral resolution, and the physical separation of

² <https://pypi.org/project/sla/>, <https://github.com/gasymovdf/sla>

³ <https://pvextractor.readthedocs.io/>

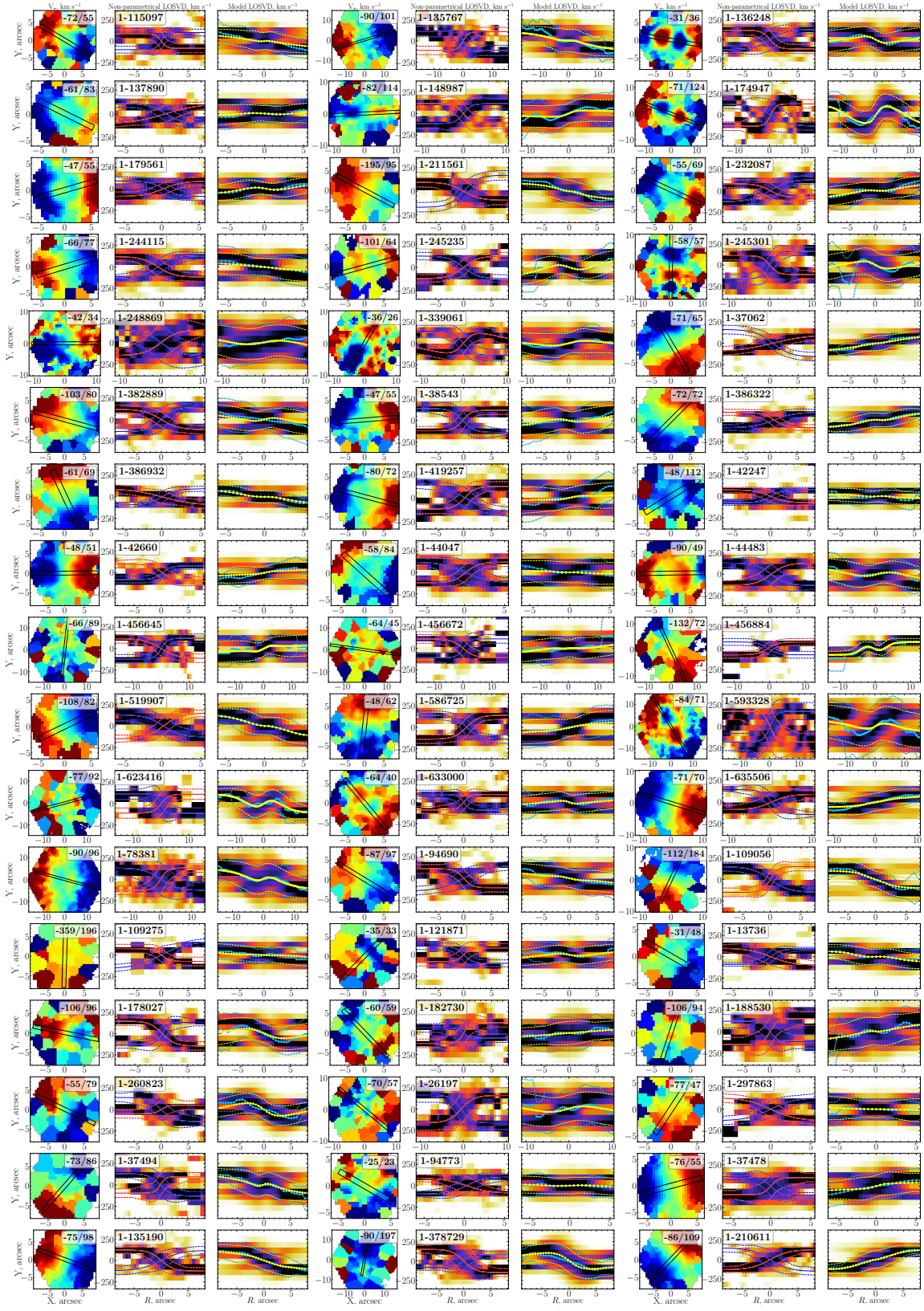


Figure 5. Subset of CR galaxies with distinct X-shaped structures in the non-parametrically recovered stellar LOSVD. The left panel displays the stellar velocity field derived from MaNGA spectra using a single-component NBURSTS analysis, with the pseudo-slit oriented along the major axis. The central panel presents the LOSVD extracted from the pseudo-slit, where dashed lines indicate the model velocities $v_i \pm \sigma_i$ and the corresponding velocity dispersions $v_i \pm \sigma_i$ for both disks (red and blue lines represent the main and CR disks, respectively). A negative radius corresponds to the left side of the map (the region with negative X-coordinates). The right panel displays a 2D representation of the LOSVD model. Cyan lines indicate v_i and $v_i \pm \sigma_i$ from the single-component NBURSTS analysis of the MaNGA spectrum, while the yellow lines are derived from the LOSVD model.

the LOS velocities between components. With MaNGA spectra, distinguishing two stellar components is challenging in the galaxy center (minimal kinematic separation) and near the IFU edge (low SNR). Therefore, we performed spectral decomposition in two optimal Voronoi bins selected from both sides of the galaxy along the major kinematic axis at the radius where the rotation curve reaches a plateau (largest ΔV) and the component weights are roughly equal. Typically, these bins correspond to the location of the 2σ peaks. Fig. 6 demonstrates an example of spectral decomposition for 1-38543. Consistent parameters from two independent bins confirm the reliability of the fit, while the discrepancies between them allow us to estimate the output errors.

In Tab. 5, we report the ages and metallicities as averages over the two bins, with uncertainties calculated by combining the standard deviation (for two bins, half of the difference between the values) and the individual errors of the bins. The kinematics and relative weights of the components fitted within selected bins are consistent with estimates obtained from non-parametric LOSVD analyses. All disk components co-rotating with the ionized gas consistently exhibit younger ages than the main disk. Additionally, we computed the stellar mass-to-light ratio $(M/L)_*$, denoted as μ , for the derived SSP parameters using photometric models calculated with the PEGASE.2 code (Fioc & Rocca-Volmerange 1997) based on the low-resolution BaSeL synthetic stellar library (Lejeune et al. 1997) and assuming a Kroupa Initial Mass Function (Kroupa 2001). We then recalibrated the total luminosity weight of the CR disk W_{CR} into its corresponding total mass weight $W_{\text{m,CR}}$ using the following equation:

$$W_{\text{m,CR}} = \frac{1}{1 + (1/W_{\text{CR}} - 1) \mu_{\text{m}}/\mu_{\text{CR}}}, \quad (7)$$

where μ_{m} and μ_{CR} are the $(M/L)_*$ ratios for the main and CR components, respectively.

Additionally, by combining the $(M/L)_*$ values with our model of the radial structure of the stellar LOSVD (see Sec. 3.2), we estimated the angular momentum of both the CR and main disks. We consider a simple model for a disk with velocity profile $v(R)$ (Eq. 1) obtained from LOSVD analysis and an exponential density profile $\Sigma(R)$ characterized by scale length h and central density Σ_0 . In this model, the total angular momentum is given by:

$$J_{\text{disk}} = \int Rv(R)dM = \Sigma_0 \int_0^{\infty} v(R) \exp\left(-\frac{R}{h}\right) 2\pi R^2 dR. \quad (8)$$

Central density Σ_0 can be calculated from total mass of the exponential disk: $M_0 = 2\pi\Sigma_0h^2$. The parameters

V_0 , R_0 , c and h were taken from the LOSVD model (Sec. 3.2), and the velocity amplitude was corrected for inclination i estimated as follows:

$$\cos i = \frac{(1-e)^2 - (1-0.8)^2}{1 - (1-0.8)^2}, \quad (9)$$

where ellipticity e was taken from the MaNGA DAP (parameter ECOEELL).

3.4. Ionized gas

Most CR galaxies in our sample show strong ionized gas emission lines. We have already used kinematic maps derived from emission line spectra to supplement our analysis of stellar populations. In this section, we discuss the sources of ionization and gas-phase metallicity.

To identify the mechanisms driving gas excitation, we employed Baldwin-Phillips-Terlevich diagrams (BPT, Baldwin et al. 1981), incorporating the demarcation lines of Kewley et al. (2001) and Kauffmann et al. (2003). For each galaxy in our sample, we computed the integrated line flux within the effective radius R_{eff} using line flux maps from the MaNGA DAP. We then filtered out faint detections by requiring that the mean GANR within R_{eff} exceeds 2 and calculated the corresponding line ratios to construct the BPT diagrams (Fig. 7). In the DAP, GANR is defined as the amplitude of the Gaussian fit of an emission line relative to the median noise measured in two sidebands near the line. Our analysis indicates that CR galaxies are evenly distributed across SF, Composite, and AGN/LINER regions (see Tab. 6).

Interestingly, when moving from stellar CR to pure gas/star CR (excluding cases with stellar CR), the distribution across BPT-[N II] classes changes, gas/star CR galaxies tending to populate the AGN region rather than the SF one (see Tab. 6). This trend is stronger in galaxies with off-plane gas/star misalignment, and particularly in polar gas disks, which we identified during sample construction (see Sec. 2.2). This implies that accretion and collisions with pre-existing gas may amplify the impact of shocks on gas ionization and potentially trigger AGN activity, as it was already demonstrated in previous work on spatially resolved spectroscopy (Egorov & Moiseev 2019), numerical simulations (Khrapov & Khoperskov 2024) and statistical study (Smirnov & Reshetnikov 2020) of polar-ring galaxies.

Gas-phase metallicity is an important observable for discussing the sources of the accreted material that forms CR disks (see discussion in Sec. 4). For galaxies with SF dominated excitation, we estimated oxygen abundances using R-calibration (Pilyugin & Grebel 2016) after preliminary correcting the fluxes for extinction using the Balmer decrement and Fitzpatrick (1999) extinction curve. The results of our analysis are shown on the Mass-Metallicity (MZR) diagram (Fig. 8). For reference, we also analyzed all SF-dominated MaNGA

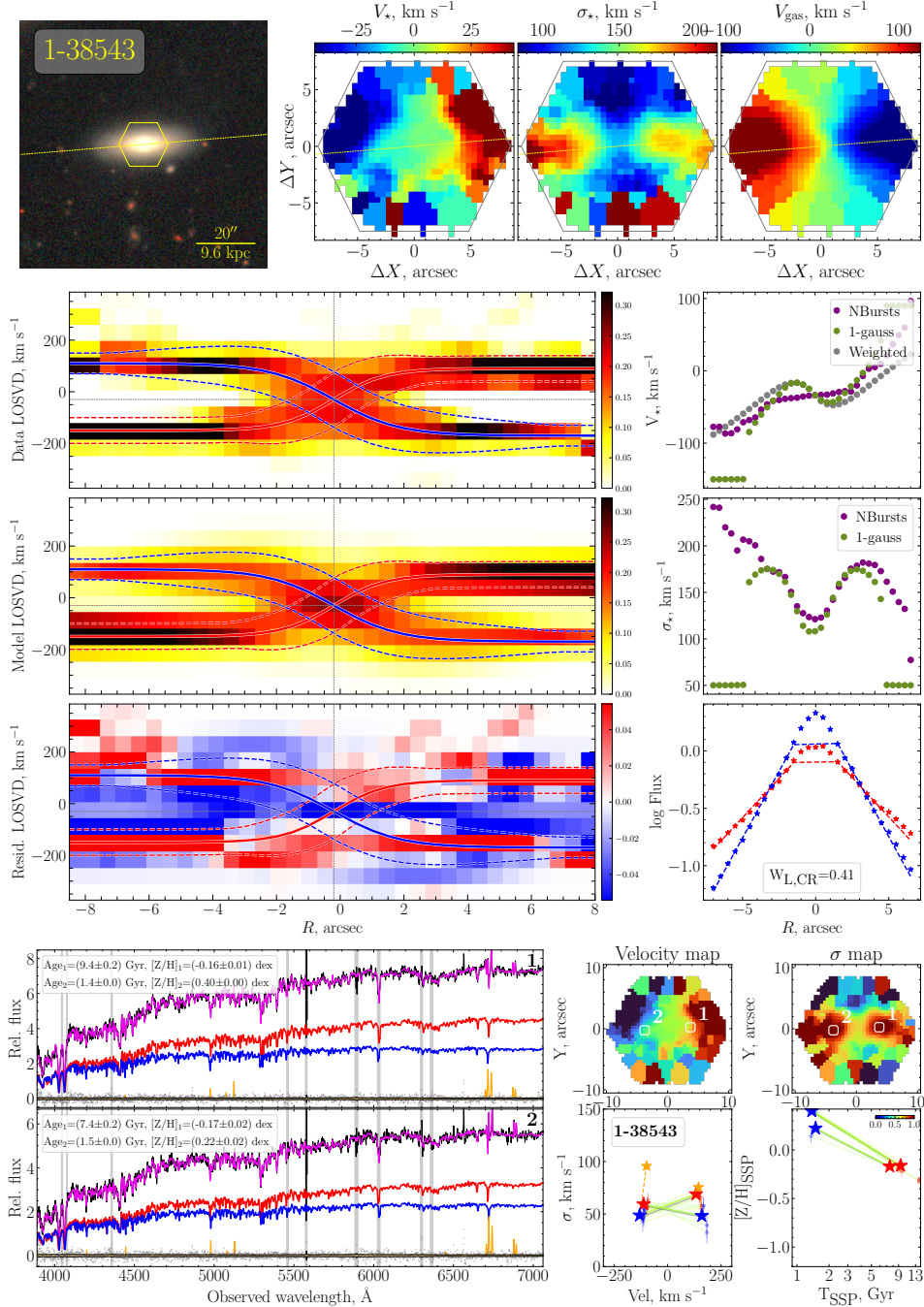


Figure 6. Example of all analysis steps for **1-38543**. We prepared similar plots for all CR galaxies (Sec. C). **Top part:** Description is similar to Fig. 1. **Middle part:** Non-parametrically recovered stellar LOSVD and its analysis. The first column shows the extracted non-parametric stellar LOSVD along the major axis, along with its model and the residuals between them. The second column displays the weighted stellar velocity from the model ($W_1 \times V_1 + (1 - W_1) \times V_2$), compared to a single-component NBURSTS fit and a pure Gaussian fitting for each spatial bin. A similar comparison is provided for the velocity dispersion σ_* . The bottom plot shows the extracted stellar intensity in the SDSS g-band along the major axis, with each disk weighted according to its exponential shape in LOSVD modeling. **Bottom part:** Two-component spectral decomposition. The left two plots display the decomposition of bins 1 and 2, whose positions are shown on the stellar velocity and velocity dispersion maps derived from single-component fitting (top central and right panels). Black lines represent the observed spectra and thin black lines show the error of these spectra. The magenta line is the sum of two stellar components and emission lines, red indicates the old main component, and blue – the young CR component. Emission lines are shown in orange, while gray dots indicate the residuals between the observed spectrum and the full model. The bottom middle and right panels show the kinematic and stellar population parameters for the old (red marks) and young (blue) components, with orange stars representing gas kinematics correlated with the young component. Transparent symbols show obtained parameters for each unbinned spaxel within the large bins. The color of the connecting marks reflects the mean weight of the old component at $\lambda = 5100 \pm 50 \text{Å}$. The color bar of this weight is shown in the top right angle of the stellar population plot.

Table 5. Table with parameters from non-parametric LOSVD and 2-component NBURSTS analysis.

ID	CR loc.	$\log(M_*/M_\odot)$	W_{LOSVD}	$T_{\text{SSP,m}}$	$[Z/H]_{\text{SSP,m}}$	$T_{\text{SSP,CR}}$	$[Z/H]_{\text{SSP,CR}}$	μ_m	μ_{CR}	W_{mass}	$\log \frac{M_{*,\text{CR}}}{M_\odot}$
(1)	(2)	(3)	(4)	(5)	(6)	(7)	(8)	(9)	(10)	(11)	(12)
1-42660	outer	10.27	73%	9.6 ± 0.6	-0.20 ± 0.03	1.3 ± 0.2	-0.03 ± 0.00	4.33	0.89	36%	9.83
1-42247	inner	9.71	39%
1-37062	inner	10.19	8%	3.2 ± 0.4	-0.01 ± 0.10	1.7 ± 0.4	-1.13 ± 0.15	2.15	0.65	3%	8.59
1-37478	inner	10.46	29%
1-38543	inner	10.36	41%	8.4 ± 1.0	-0.17 ± 0.03	1.4 ± 0.1	0.31 ± 0.09	4.06	1.27	18%	9.62
1-339061	inner	10.32	33%	6.8 ± 0.4	0.00 ± 0.04	1.7 ± 0.2	-0.73 ± 0.10	4.12	0.77	8%	9.24
1-44047	outer	10.22	61%	13.7 ± 0.9	-0.40 ± 0.12	1.7 ± 0.2	0.38 ± 0.06	4.91	1.60	34%	9.75
1-44483	outer	10.12	67%	12.9 ± 0.7	-0.36 ± 0.04	1.5 ± 0.2	0.18 ± 0.23	4.84	1.25	34%	9.65
1-382889	inner	10.37	32%	4.3 ± 0.4	-0.08 ± 0.07	1.7 ± 0.3	-0.83 ± 0.09	2.69	0.73	11%	9.42
1-386322	outer	9.94	79%	13.0 ± 1.2	-0.16 ± 0.08	3.8 ± 0.4	-0.25 ± 0.05	5.72	2.13	58%	9.70
1-137890	inner	9.89	41%	3.8 ± 1.6	-0.12 ± 0.08	1.5 ± 0.3	-1.29 ± 0.08	2.37	0.59	15%	9.07
1-386932	inner	9.87	20%	6.0 ± 0.7	-0.25 ± 0.09	2.1 ± 0.1	-0.94 ± 0.06	2.88	0.84	7%	8.71
1-232087	outer	10.28	71%	11.2 ± 1.6	-0.44 ± 0.07	1.0 ± 0.0	-0.25 ± 0.03	4.02	0.64	28%	9.73
1-78381	outer	10.96	78%	14.0 ± 0.8	0.15 ± 0.06	11.0 ± 0.7	-0.57 ± 0.08	8.08	3.63	61%	10.75
1-586725	inner	10.37	33%	6.4 ± 1.3	-0.13 ± 0.07	1.2 ± 0.1	-0.37 ± 0.14	3.42	0.67	9%	9.31
1-148987	inner	10.34	65%	9.5 ± 3.4	-0.32 ± 0.07	2.3 ± 0.1	-0.12 ± 0.04	3.92	1.52	42%	9.96
1-174947	outer	10.68	60%	12.5 ± 1.8	-0.46 ± 0.20	4.6 ± 2.9	-0.84 ± 1.04	4.36	1.66	37%	10.25
1-519907	outer	10.09	85%	14.0 ± 1.5	-0.23 ± 0.11	8.2 ± 0.2	-0.17 ± 0.03	5.75	3.98	79%	9.99
1-623416	outer	10.16	44%	13.7 ± 0.7	-0.32 ± 0.06	2.8 ± 0.3	-0.40 ± 0.17	5.27	1.44	18%	9.41
1-456884	inner	9.54	51%	10.0 ± 2.5	-0.69 ± 0.09	6.5 ± 0.6	0.01 ± 0.09	3.10	3.95	57%	9.30
1-456672	outer	10.13	49%
1-456645	outer	9.96	57%	4.3 ± 1.3	-0.19 ± 0.25	1.9 ± 0.4	-0.97 ± 0.12	2.49	0.77	29%	9.42
1-419257	inner	10.31	37%	6.4 ± 2.3	-0.02 ± 0.08	1.3 ± 0.1	-0.58 ± 0.09	3.78	0.63	9%	9.26
1-244115	inner	10.14	31%	8.7 ± 1.4	-0.09 ± 0.10	1.4 ± 0.2	-0.36 ± 0.14	4.45	0.73	7%	8.98
1-245235	inner	10.15	40%	5.0 ± 1.0	-0.05 ± 0.09	2.0 ± 0.1	-0.84 ± 0.15	3.06	0.84	15%	9.34
1-245301	outer	10.75	33%
1-593328	inner	11.20	48%	9.8 ± 0.7	-0.03 ± 0.10	1.8 ± 0.6	-0.13 ± 0.11	5.14	1.18	17%	10.44
1-633000	inner	10.06	48%	10.7 ± 2.5	-0.33 ± 0.07	1.0 ± 0.0	-0.18 ± 0.08	4.25	0.66	13%	9.16
1-248869	outer	10.85	49%	13.5 ± 0.9	-0.15 ± 0.05	3.8 ± 0.9	-0.10 ± 0.12	5.97	2.37	27%	10.28
1-211561	inner	10.27	11%	7.3 ± 0.5	-0.24 ± 0.06	1.9 ± 0.4	-0.95 ± 0.29	3.42	0.78	3%	8.70
1-135767	outer	10.55	68%	14.0 ± 0.7	-0.34 ± 0.07	3.5 ± 0.5	-0.05 ± 0.13	5.24	2.29	49%	10.24
1-94690	inner	10.22	32%	7.6 ± 3.3	-0.18 ± 0.11	2.1 ± 0.2	-0.81 ± 0.10	3.77	0.92	10%	9.23
1-136248	outer	10.52	65%	8.9 ± 1.7	-0.35 ± 0.06	3.6 ± 0.3	-0.04 ± 0.06	3.61	2.32	54%	10.26
1-635506	inner	10.21	14%	6.2 ± 1.1	-0.08 ± 0.04	3.0 ± 0.3	-0.58 ± 0.08	3.54	1.33	6%	8.98
1-179561	inner	10.09	37%
1-115097	inner	10.23	24%	8.4 ± 0.4	-0.41 ± 0.06	2.8 ± 0.3	-0.02 ± 0.07	3.29	1.91	16%	9.43
1-109056	outer	10.41	84%
1-37494	outer	10.18	66%
1-109275	inner	10.05	39%
1-297863	inner	10.25	46%	7.7 ± 1.9	-0.55 ± 0.10	2.0 ± 0.3	0.31 ± 0.14	2.77	1.81	36%	9.80
1-378729	undef	10.20	16%
1-121871	inner	10.11	45%
1-182730	inner	11.05	54%	11.9 ± 2.3	-0.27 ± 0.16	2.9 ± 0.5	-0.06 ± 0.19	4.82	1.92	32%	10.55
1-188530	inner	10.66	38%
1-260823	outer	10.47	68%
1-13736	inner	10.08	32%	10.6 ± 3.7	-0.35 ± 0.13	3.2 ± 1.2	-0.77 ± 0.32	4.13	1.23	12%	9.18
1-210611	inner	10.30	14%	6.5 ± 0.3	-0.17 ± 0.04	1.7 ± 0.4	-0.64 ± 0.19	3.36	0.78	4%	8.86
1-135190	inner	10.47	20%	6.9 ± 0.9	-0.02 ± 0.04	1.4 ± 0.0	-0.58 ± 0.13	4.04	0.66	4%	9.07
1-94773	inner	10.18	44%	6.0 ± 1.0	-0.20 ± 0.09	3.5 ± 1.5	-0.76 ± 0.21	3.07	1.37	26%	9.59
1-178027	outer	10.44	32%	13.5 ± 1.1	-0.22 ± 0.07	3.0 ± 0.6	0.03 ± 0.19	5.63	2.10	15%	9.62
1-26197	outer	10.93	44%	14.0 ± 1.3	-0.07 ± 0.12	2.7 ± 0.3	-0.34 ± 0.17	6.53	1.48	15%	10.11

NOTE: (1) The MaNGA-ID of the galaxy. (2) The location of the CR disk, assuming a connection between its kinematics and the gas or, where possible, the location of the younger component. (3) The stellar mass from NSA, corrected to H_0^2 . (4) The weight of the CR disk in the total luminosity of the galaxy (Sec. 3.2). (5) and (7) are the SSP-equivalent ages of the main and CR disks in Gyr, respectively. “...” means failure of the two-component analysis. (6) and (8) are the SSP-equivalent stellar metallicities of the main and CR disks in dex. (9) and (10) are the (M/L) ratio in the SDSS g -band for the main and CR disks. (11) CR disk stellar mass fraction (Eq. 7). (12) The estimated stellar mass of the CR disk.

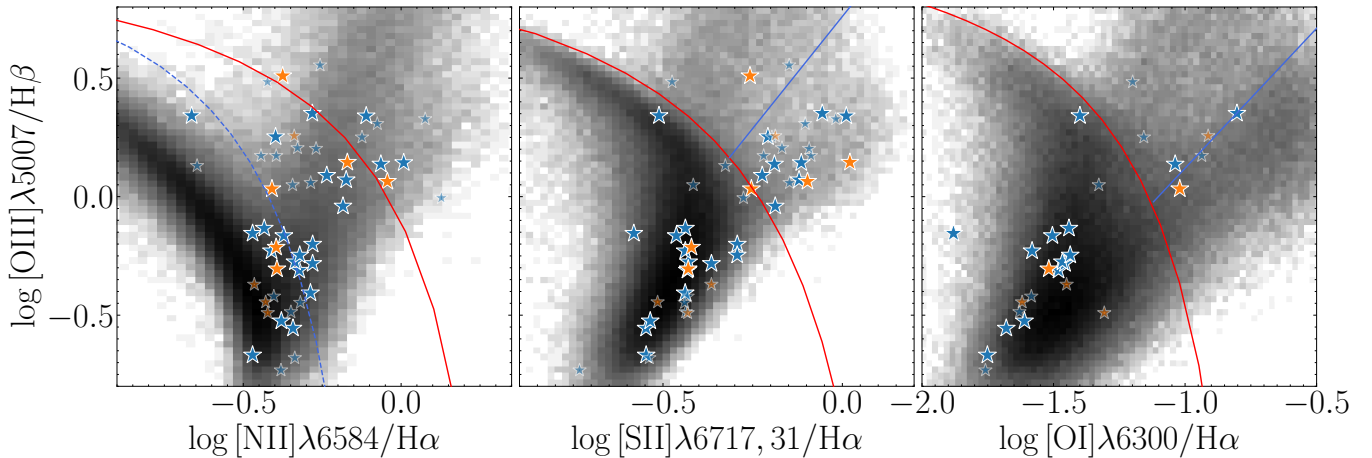


Figure 7. BPT-[N II], -[S II] and -[O I] diagrams for the sample of CR galaxies. Bright and small stars show **reliable** and **probable** CR galaxies. Blue and orange colors show **inner** and **outer** configurations of CR disk (Sec. 4.1). The blue dashed line in the BPT-[N II] plot represents the demarcation line introduced by [Kauffmann et al. \(2003\)](#), which distinguishes between the star-forming and the so-called composite regions. The additional demarcation lines taken from [Kewley et al. \(2001\)](#). They separate composite and AGN regions on the BPT-[N II] diagram and categorize star-forming, Seyfert/LINER regions in the BPT-[O I] and BPT-[S II] diagrams. The distribution of emission line measurements from the RCSED ([rcsed.sai.msu.ru](#), [Chilingarian et al. 2017](#)) is represented in grey.

Table 6. Percentage of galaxies in different regions of the BPT-[N II] by type of kinematic misalignment. Galaxies with stellar CR were excluded from the pure gas-star misalignment categories (CR-GS, Gas-Polar, Gas-Mis.). The “Weak lines” designates galaxies with too weak emission lines to be used in the BPT-[N II] diagram. The number of galaxies of each type is given in the table head.

	CR (120)	CR-GS (145)	Gas-Polar (116)	Gas-Mis. (172)
SF	29%	21%	8%	9%
Comp.	28%	26%	20%	22%
AGN	24%	34%	43%	34%
Weak lines	19%	19%	29%	35%

galaxies using the same method, displaying them as grey background in Fig. 8. For clarity, we computed a second-degree polynomial fit for these MaNGA galaxies (shown as the thick blue line) that closely matches the MZR shape reported by [Duarte Puertas et al. \(2022\)](#) with a deviation of only 0.04 dex. We observe that the majority of stellar CR galaxies have ionized gas metallicities higher than those predicted by their stellar masses.

We evolutionarily link the ionized gas component to the formation of the CR disk, dismissing any substantial contribution from the pre-existing ISM. If the CR disk is viewed as an individual galaxy formed apart from its host, we would assign it a much lower stellar mass for the measured gas metallicity, which would increase its devi-

ation from the mean MZR. The gas-phase metallicity we observe today reflects the cumulative metal enrichment during CR disk formation and depends on both the metallicity of the accreted material and the efficiency of the enrichment process. The enhanced metallicity in CR galaxies may indicate that the accreted material was already pre-enriched and/or that SF was highly efficient, leading to rapid metal enrichment. These scenarios can be tested through chemical evolution models, as demonstrated in our study of PGC 66551 ([Katkov et al. 2024b](#)).

Our approach to use emission lines and oxygen abundance calibration follows the same methodology by [Zinchenko \(2023\)](#) in their studies of counter-rotating gas in MaNGA galaxies. They found that red star/gas CR galaxies have lower oxygen abundances for a given mass, while blue ones have typical or higher values. The findings for our stellar CR galaxies are consistent with those for blue galaxies. In fact, our targets with reliable gas metallicities are classified as SF on the BPT and exhibit blue colors on the CMD. However, neither our stellar CR sample nor the larger group of galaxies with gas misalignments (aside from galaxy 1-72211) deviates notably from the MZR toward lower metallicities, as reported by [Zinchenko \(2023\)](#) for red gas/star CR galaxies. We suspect that ongoing mergers, excluded during visual inspection and sample construction, may be responsible for this discrepancy.

4. DISCUSSION

4.1. Dichotomy between inner and outer CR

Table 7. Schema of kinematic diversity of stellar counter-rotation configurations

Dominance of external (E) over pre-existing (P) gas	Angular momentum of externally accreted material	
	Low	High
$E \gg P$	inner	outer
$E \gtrsim P$	AGN, central SB / inner	inner / outer
$E < P$	No CR	external CR ring

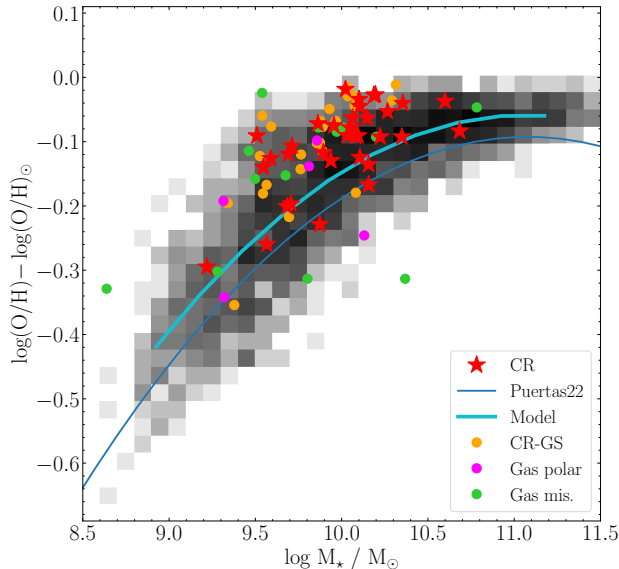


Figure 8. Stellar mass – gas-phase metallicity relation (MZR). Metallicity is given relative to $12 + \log(\text{O}/\text{H})_{\odot} = 8.69$ (Asplund et al. 2021). The background represents all MaNGA galaxies classified as SF based on the BPT-[N II] diagram. Red stars denote gas in CR galaxies, while orange, purple, and lime dots correspond to galaxies with CR-GS, gas-polar, and gas misalignment, respectively. The light blue line shows a second-degree polynomial fit to all MaNGA galaxies, while the blue line is taken from (Duarte Puertas et al. 2022).

Due to the large statistical sample, the MaNGA IFU survey has successfully detected numerous CR galaxies. The growing number of identified CR galaxies, as demonstrated in this paper and previous studies, reveals that the family of CR galaxies is not uniform. Instead, it comprises two distinct kinematic configurations: *inner* and *outer*. Inner CR galaxies exhibit younger CR components, associated with gas kinematics, that are compact and predominantly concentrated in the central regions. In contrast, outer CR galaxies display counter-rotating components that are more extended than the main stellar body.

Fig. 9 illustrates the differences in the parameters observed between inner and outer stellar CR in galaxies, which can be summarized as follows:

1. In galaxies with outer CR configuration, the stellar populations of both the CR and main disk are moderately older than those in galaxies with inner CR (see panels *a* and *c*).
2. Panel *b* shows that the metallicity distributions suggest inner CR disks generally have lower metallicity compared to outer CR disks.
3. The separation in stellar metallicities for main disks is weak, if it exists (panel *d*).
4. Panel *h* shows that the luminosity contribution of CR disks is significantly larger for outer configurations, confirming our earlier preliminary conclusion based on a smaller sample of CR galaxies Gasymov & Katkov (2022). Nonetheless, our current analysis based on an extended sample does not reveal a significant difference in the total stellar masses of galaxies with inner and outer CR (see Fig. 10)
5. The parameters $Q_{\text{tidal},1\text{Mpc}}$ and $Q_{\text{tidal},5\text{Mpc}}$ (panels *i* and *j*), which measures the averaged tidal gravitational strength from neighboring galaxies within 1 or 5 Mpc and characterizes the environmental density, do not show a statistically significant difference between inner and outer CR galaxies. However, there is a weak tendency for inner CR galaxies to be found in sparser environments, particularly in the peaks of the distribution.
6. Galaxies with inner CR tend to exhibit slightly higher specific star formation rates (sSFR, panel *g*) and demonstrate more prominent difference in the atomic phase gas content (panel *f*).
7. Finally, we computed the angular momentum of the stellar main and CR disks (see panels *k* and *l*) and found that the momentum of the CR disk’s inner and outer configurations are clearly distinguished by this parameter, whereas the momentum of the main disk is quite similar in both outer and inner configurations.

We inspected deep images from DECaLS and the Hyper Suprime-Cam Subaru Strategic Program (Miyazaki et al. 2018; Aihara et al. 2019) and identified another

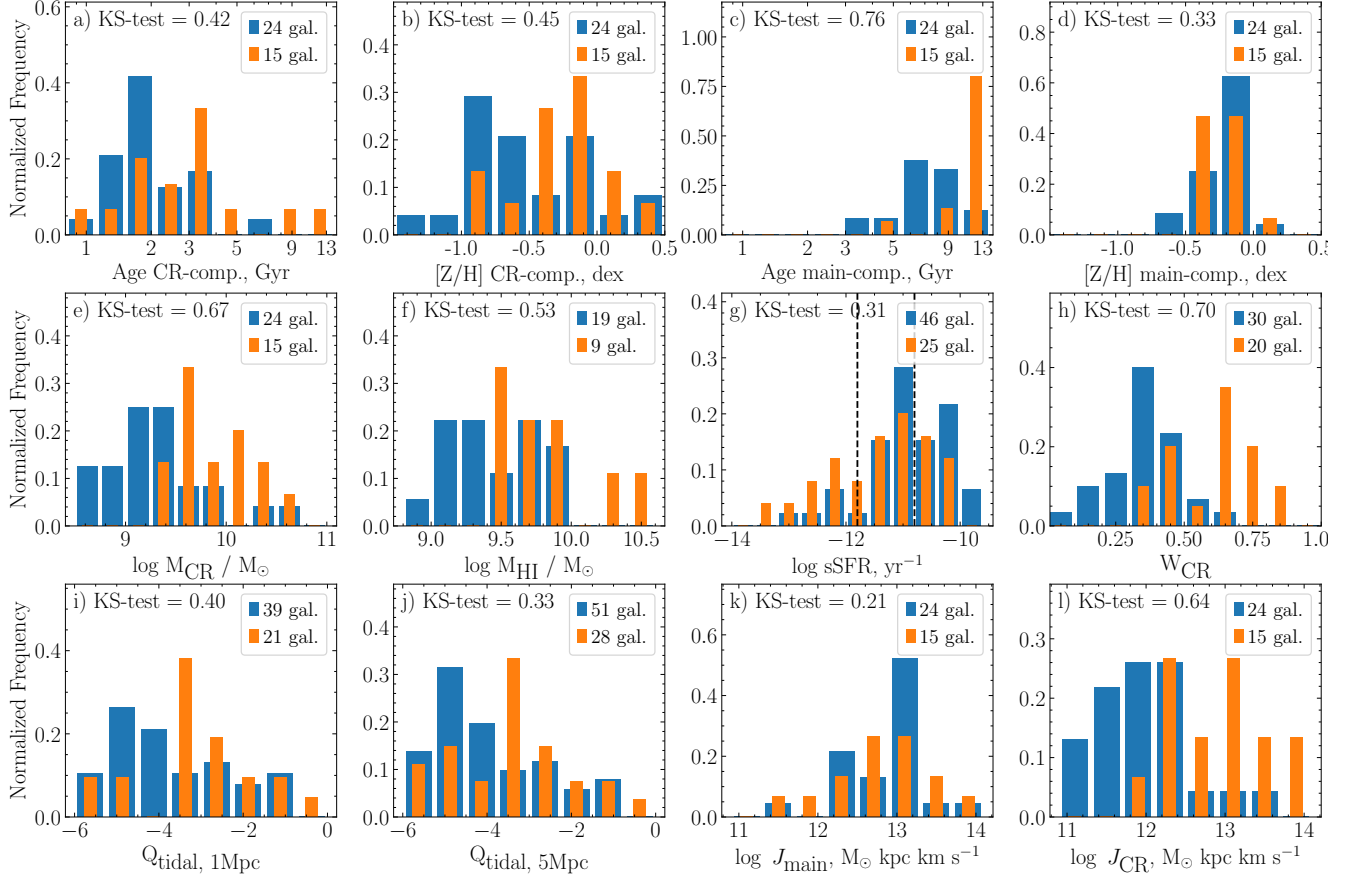


Figure 9. Comparison of inner and outer configurations of stellar CR disk. Orange histograms show outer CR galaxies and blue — inner CR. The description of parameters can be found in Sec. 4.1. The number in the top left corner represents the Kolmogorov-Smirnov test probability.

difference between the outer and inner CR configurations. In general, outer CR galaxies more frequently exhibit morphological peculiarities: low-surface brightness (LSB) structures in galaxy periphery (6 outer vs. 2 inner), tidal tails (4 outer vs. 3 inner). Also, only outer CR galaxies demonstrate clear spiral structures (1-174947, 1-135767, 1-178027). Notably, the asymmetrical two-arm spiral pattern in galaxy 1-178027 might be a result of tidal interaction. Given the lower detection rate of outer CR galaxies in our sample – 29 outer compared to 53 inner CR galaxies – the relative frequency of morphological features indicative of possible past interactions is significantly higher among outer CR galaxies. In Sec. 4.2, we discuss in-depth the connection between CR galaxies and LSB galaxies.

We propose the following schema for the kinematic diversity of CR galaxies based on two principal parameters: the angular momentum of the externally accreted material and the ratio of mass (or density) of pre-existing and infalling gas. This schema is summarized in the Tab. 7. When external material dominates, it forms either an inner or an outer CR configuration, depending on whether the angular momentum is low or high,

respectively. Such a scenario naturally results in the observed separation between inner and outer CR configurations in the angular momentum histograms shown in Fig. 9, panel *k* and *l*. If the pre-existing gas dominates, then no CR formation occurs in the case of low momentum accretion, and possibly an external CR ring can form in the case of high momentum accretion (similar to that formed in NGC 254 (Katkov et al. 2022)). In scenarios where the mass of the external and pre-existing materials is comparable, the picture can be more complex. With low momentum accretion, the infalling gas collides with the pre-existing gas, losing momentum and spiraling toward the galaxy center, potentially forming an inner CR. This process is also likely to result in substantial gas deposition at the center, which could trigger AGN activity or a central starburst. Numerical simulations (Cenci et al. 2024; Peirani et al. 2025) suggest that, at this stage, a significant fraction of the pre-existing gas can be converted into stars, facilitating subsequent external gas accretion. In the case of high momentum accretion, both inner and outer CR configurations might emerge.

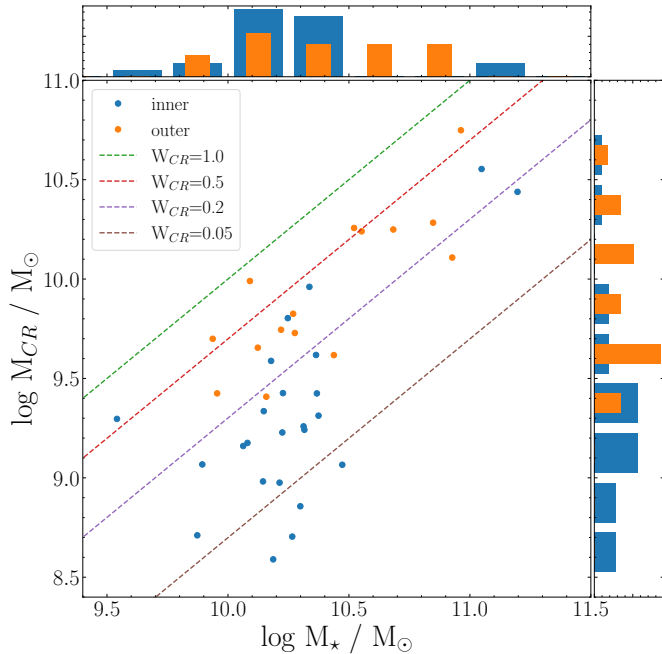


Figure 10. Galaxy stellar mass vs. stellar mass of CR disk. Blue dots correspond to the inner configuration of the CR disk, while orange dots to the outer one. The lines represent different mass fractions of CR disks.

The accretion scenario underlying our proposed schema aligns with the results of cosmological TNG100 simulations (Khoperskov et al. 2021). According to the study of the galaxies with stellar CR found in the results of TNG100 the CR components could be formed by gas accretion from cosmological filaments or gas-rich CGM in the outskirts. Also according to this study 88 percent of the models with CR show the CR components as more extended than the host ones, with the CR components consistently younger than the host components across all considered models. In contrast, our sample reveals a significantly lower fraction of outer CR. This discrepancy may be partly explained by the selection criterion used in Khoperskov et al. (2021), where models were chosen if at least 30% of their stars rotated in the opposite direction to the main stellar disc. At the same time, our study suggests that inner CR galaxies tend to have a lower mass for the CR components (see Fig. 10), therefore, such strict criteria for identifying CR galaxies in simulation might overlook some inner CR. Another potential explanation for the difference lies in the nature of the data: observations provide luminosity-weighted stellar properties, whereas simulations deal with stellar mass particles. Additionally, the limited field of view of MaNGA spectra ($\approx 1.5 - 2.5 R_{\text{eff}}$) may result in some unclear cases actually being outer CR.

In a more recent study based on the high-resolution zoom-in simulation NEWHORIZON, focused on field environments, Peirani et al. (2025) identified ten CR galaxies

whose CR stars are typically more metal-rich than the co-rotating counterparts and concentrated in the inner regions. These CR galaxies formed through interactions with satellite galaxies and closely resemble our inner CR systems located at the metal-rich end of the distribution. Outer CR configurations are also reproduced in these simulations and, in most cases, are associated with major or multiple mergers.

4.2. On the CR galaxies with LSB structures

Among the galaxies identified with kinematically misaligned subsystems in our initial inspection (Sec. 2.2), we detected extended LSB structures in 20 misaligned galaxies. Specifically, among galaxies with stellar CR disks, we observed such structures in 2 inner and 6 outer systems.

These galaxies with LSB peripheries morphologically resemble giant low-surface brightness galaxies (gLSBGs) — systems with highly extended LSB disks, reaching radii of up to 130 kpc and containing dynamical masses of up to $10^{12} M_{\odot}$ within these disks (Boissier et al. 2016). The formation of gLSBGs remains a topic of debate (see, e.g., Lelli et al. 2010; Boissier et al. 2016; Hagen et al. 2016; Saburova et al. 2021, 2023; Junais et al. 2024). The observed data support an external origin for the material forming the giant disks, likely stemming from either mergers or accretion from cosmic filaments.

The similarity between gLSBGs and galaxies with CR and LSB structures becomes even more striking, as some gLSBGs also exhibit CR (Saburova et al. 2021). UGC 1382 (1-35391), a well-known gLSBG also identified during the inspection of MaNGA data in this paper, exhibits global counter-rotation of ionized gas and neutral hydrogen relative to its inner stellar component. To investigate whether star formation in the CR gaseous disk has produced enough stars to be detected, Saburova et al. (2021) applied a non-parametric method to recover the stellar LOSVD, following a similar approach used in this paper. However, they did not detect clear signs of the stellar CR, finding only a slightly non-Gaussian shape and a peaked structure of the LOSVD that varies insignificantly from one spatial bin to another. This suggests that CR stars in the LSB disk are too faint to be detected in the region dominated by the high surface brightness disk, where spectra were obtained. UGC 1922 is another gLSBG that hosts kinematically decoupled structures but does not show clear evidence of stellar CR (Saburova et al. 2018).

Low star formation efficiency may explain why LSB disks retain their low brightness (even in the presence of cold gas as in UGC 1382 (Saburova et al. 2021)), and consequently fail to exhibit stellar CR despite the presence of CR gas. Although measurements of metal content in the ISM of gLSBGs galaxies are limited, the available data indicate a metal deficiency (Saburova et al. 2024) supporting this idea. Recently studied in Katkov et al. (2022) NGC 254, not a gLSBG, but

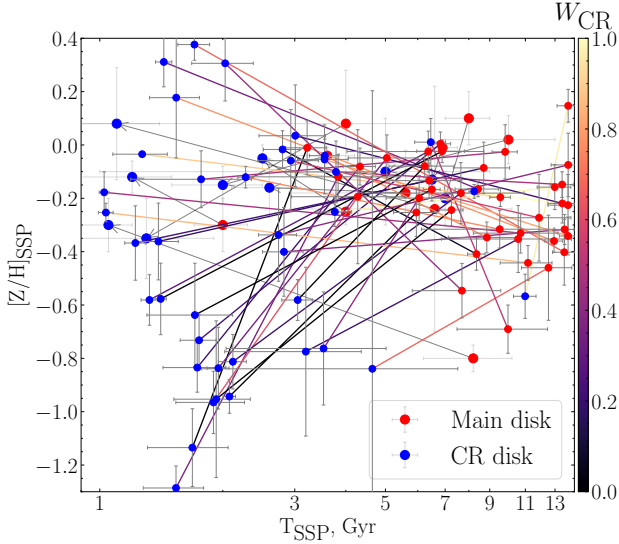


Figure 11. SSP-equivalent age — stellar metallicity diagram for the main and CR disks. Color represents the luminosity weight of the CR disk (Tab. 5), while previously studied CR galaxies (see Tab. 1) are shown in the background with gray lines.

this galaxy hosted an extended outer ring with global gaseous counter-rotation is an example of how low star formation ($\text{SFR} \approx 0.02 M_{\odot} \text{ yr}^{-1}$) can result in a hidden CR stellar population with a mass fraction of about 1%, making it nearly impossible to detect purely spectroscopically.

Saburova et al. (2023) proposed that gLSBGs may not represent a distinct class of peculiar systems but rather an extension of normal-sized spirals toward larger radii. This idea is also supported by Mancera Piña et al. (2021), who found that gLSBGs are not outliers and follow the same relationship between baryonic specific angular momentum, mass and gas fraction as other disk galaxies, despite their notably high angular momentum. As illustrated in Fig. 9 (l), outer CR components exhibit the highest angular momentum, further emphasizing a possible evolutionary link between gLSBGs and stellar CR galaxies.

4.3. The origin of accreted material

External accretion of significant amounts of gas is the primary mechanism proposed for the formation of kinematically misaligned components. This accreted gas may originate from cosmic filaments (Algorry et al. 2014b; Khoperskov et al. 2021), mergers with gas-rich companions (Thakar & Ryden 1996b, 1998; Khim et al. 2021; Lu et al. 2021), or tidal interactions and gas exchange with neighboring galaxies (Khim et al. 2021; Sil’chenko et al. 2023). In this section, we aim to determine the most likely origin of the accreted gas responsible for forming the CR components in our sample.

Gas-phase metallicity and stellar metallicity are the key parameters for determining the origin of the accreted gas. Low stellar metallicity in the CR disk is expected if it formed from gas supplied by cosmic filaments. These filaments deliver extremely metal-poor, pristine gas to a galaxy. While the accreting cosmic streams may become slightly enriched through interactions with pre-enriched hot halo gas or outflowing winds (van de Voort & Schaye 2012; Hafen et al. 2017), the gas that ultimately settles into the disk and forms the CR disk should largely retain its low metallicity. The accreted material from other galaxies is expected to be pre-enriched, with gas-rich small companions generally exhibiting low metallicities, while major tidal gas exchanges involve material from massive galaxies that might have approximately solar metallicity.

To constrain the gas source, a detailed chemical evolution model with many parameters is required, such as the toy model applied to galaxy 1-179561 (PGC066551, Katkov et al. 2024b). However, such analysis is beyond the scope of the current study and will be addressed in future papers. Here, we note that gas-phase metallicity measurement reflects the current chemical abundance of the gas, while the stellar metallicity of the CR disk corresponds to a luminosity-weighted average of the gas-phase metallicity over the disk’s star formation history.

In our sample of CR galaxies, the stellar metallicity of the CR component lies within a broad range, from extremely metal-poor (≈ -1.2 dex) to super-solar (≈ 0.4 dex) values (Fig. 11). In contrast, the gas-phase metallicity shows a much narrower range, from ≈ -0.3 dex to ≈ 0 dex (Fig. 8 and Fig. 12). For most galaxies, the gas-phase metallicity is noticeably higher than the stellar metallicity in the CR disk. This configuration is a natural result of the chemical evolution and enrichment of metal-poor gas accreted in the past. However, for a few galaxies, which turned out to be outer CR galaxies, the gas-phase metallicity is comparable to or even lower than the stellar population metallicity in the CR disk. This strongly suggests recent or ongoing accretion of low-metallicity gas into these galaxies. It is important to note that this conclusion is based on a small number of outer CR galaxies with available ionized gas measurements. However, in general, the wide range of observed metallicities indicates that no single external gas source can universally explain the accretion history of all studied galaxies.

4.3.1. Galaxy environments

The environmental properties of our galaxies provide additional constraints on possible accretion sources. Cosmic filaments are viable accretion sources primarily in sparse environments. Conversely, gas exchange with neighboring galaxies requires an intermediate-density environment, as high-density regions are dominated by ram-pressure stripping, which prohibits gas transfer.

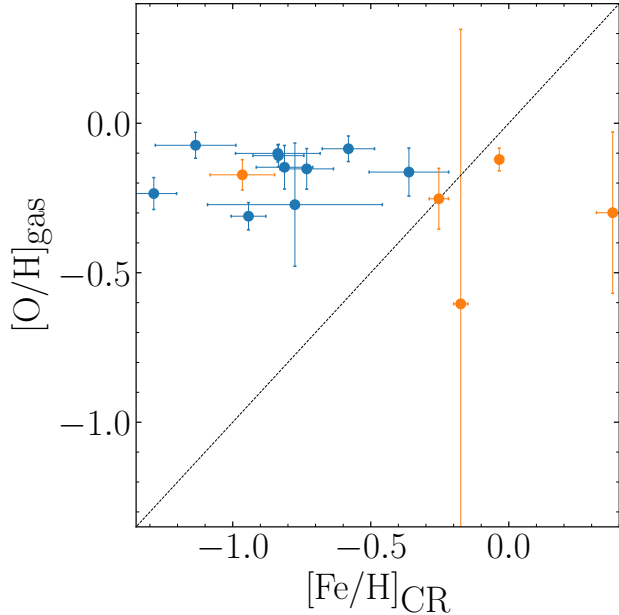


Figure 12. Stellar vs. gas-phase metallicity of CR disks. Metallicity is given relative to $12 + \log(\text{O}/\text{H})_{\odot} = 8.69$ dex (Asplund et al. 2021). Blue and orange symbols represent inner and outer configurations, respectively. Stellar metallicity is derived from two-component decomposition (Sec. 3.3). For consistency, gas-phase metallicity was calculated using the R-calibration (Pilyugin & Grebel 2016) in the same spatial bins where two-component decomposition was conducted, rather than within R_{eff} as used in Sec. 3.4.

We cross-matched our CR sample with the GEMAVAC, utilizing several parameters to assess environmental density. These parameters include $Q_{1\text{Mpc}}$ (the logarithm of the ratio between the tidal gravitational strength from neighbors within 1 Mpc and the galaxy’s internal binding forces), $Q_{5\text{Mpc}}$ (similar to $Q_{1\text{Mpc}}$ but considering neighbors within 5 Mpc), and $\log 1 + \delta$ (where $\delta = \frac{\rho_{5\text{th}} - \rho_{\text{m}}}{\rho_{\text{m}}}$ represents the difference between the mean density ρ_{m} around the galaxy and the environmental density $\rho_{5\text{th}}$ to the 5th nearest neighbor; see details in Etherington & Thomas (2015)). The galaxies in our CR sample are generally found in slightly sparser environments than those in the overall MaNGA sample (see Fig. 13), which aligns with our earlier findings of a high incidence of kinematic misalignments in isolated lenticular galaxies (Katzkov et al. 2014, 2015). However, the broad environmental distribution prevents us from conclusively ruling out any of the proposed above gas sources.

The distributions of $Q_{\text{tidal},1\text{Mpc}}$ and $Q_{\text{tidal},5\text{Mpc}}$ (Fig. 13) show distinct peaks, with one peak associated with galaxies hosting inner CR disk configurations and the other with outer configurations. We propose that

these peaks reflect different dominant accretion scenarios. For inner CR disks, accretion of pristine gas from the circumgalactic medium (CGM) in low-density environments could explain the observed peak. This scenario involves the accretion of low-angular-momentum gas, which facilitates the formation of inner disks and leads to the low stellar metallicities observed in these configurations. In contrast, some outer CR disks are likely formed through tidal gas exchange with a nearby massive galaxy, a process occurring in intermediate-density environments. This gas exchange delivers high-angular-momentum material, facilitating the formation of an outer CR disk or a blue star-forming ring. The accretion of pre-enriched gas leads to the formation of more metal-rich CR disks, which we generally observe in outer CR configurations compared to their inner counterparts.

Summarizing, the sample of CR galaxies displays a wide range of parameters, making it challenging to pinpoint one preferred mechanism for CR disk formation. While accretion from cosmic filaments and tidal interactions may play important roles in sparse and intermediate-density environments, respectively, we highlight gas-rich companion accretion as a versatile mechanism capable of operating across a wide range of environments – excluding regions of extreme overdensity, which lack CR galaxies.

5. CONCLUSIONS

In this paper, we present a comprehensive study of stellar counter-rotation in galaxies using the MaNGA spectroscopic survey. Through a combination of visual inspection and analysis of non-parametric recovered stellar LOSVD, we identified a significantly expanded sample of 120 counter-rotating (CR) galaxies, including 65 *reliable* and 55 *probable* systems. New CR galaxies account for $\approx 1.5\%$ of all ETGs ($\approx 2.9\%$ of S0 galaxies) and $\approx 0.8\%$ of all LTGs in the Near Universe. Our conclusions can be summarized as follows:

1. Despite the limitations of MaNGA spectral data, we successfully performed spectral decomposition and derived the luminosity-weighted stellar population properties (ages and metallicities) for both disks in 39 out of 120 identified CR galaxies. Our analysis revealed that CR galaxies form a diverse family, exhibiting a wide range of ages and metallicities. However, in all cases, the gas component was found co-rotated with the younger stellar population, reinforcing their evolutionary connection.
2. We demonstrated the bimodality of kinematic configurations in CR galaxies: *inner*, where the CR disk associated with ionized gas and dominates in the central part of the galaxy, and *outer*, where CR stars dominate in the galaxy disk periphery.

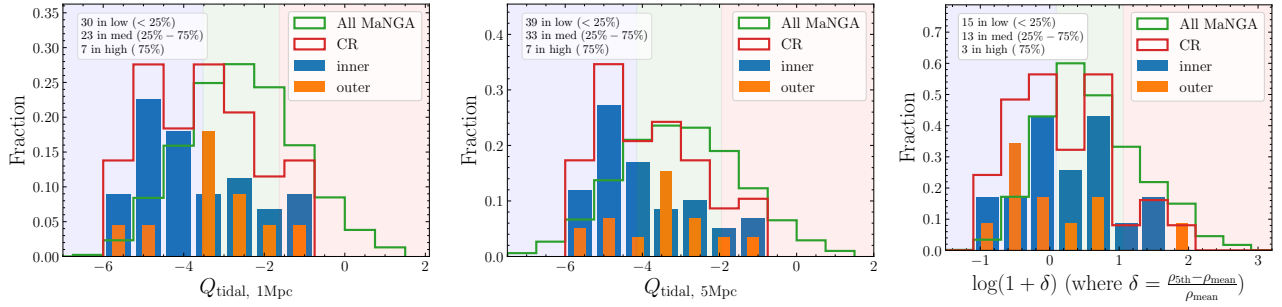


Figure 13. Distribution of the environmental parameters from GEMA-VAC (at 1, 5 Mpc, and overdensity). Blue, green, and red zones show sparse, moderate, and dense environments, divided by 25th and 75th percentiles of the parameters. Green histograms represent the properties of all MaNGA galaxies, while red histograms correspond to CR galaxies. Blue and orange histograms show the properties of the inner and outer configurations of the CR disk, respectively. They are normalized to the total number of CR galaxies.

Through stellar population analysis, we clearly established a distinction in stellar mass and angular momentum between the inner and outer CR disks.

3. We detected extended LSB features in 20 kinematically misaligned galaxies (11 with stellar CR). Among them, some systems with stellar CR predominantly showing the outer CR configuration. These galaxies show morphological similarities with the gLSBGs – systems with very large low-surface brightness disks exhibiting outer configuration in the known cases with counter-rotation. It can indicate that similar processes may drive the formation of both giant disks and CR systems with LSB features.
4. CR galaxies are found in diverse environments but generally tend to reside in sparse environments. The stellar metallicities of CR disks span a broad range. These observational properties make it challenging to identify a single external source of material responsible for CR disk formation. Possible scenarios include accretion from cosmological

filaments, mergers with gas-rich satellites, and material exchange with neighboring galaxies. However, mergers with gas-rich satellites may represent a more universal mechanism, as they can occur across different environments and, depending on the prior history of metal enrichment, can produce a wide range of final metallicities in the CR disk.

5. In addition to the CR galaxies, we identified 588 galaxies with kinematic misalignments (including 120 galaxies with stellar CR). This entire sample includes 207 galaxies with gas-star counter-rotation (145 excluding stellar CR systems), 119 with polar gas disks (116 excluding stellar CR systems), and 173 with intermediate gas misalignments (172 excluding stellar CR galaxies). Of these kinematically misaligned galaxies, approximately 68% are early-type galaxies (ETGs), accounting for about 10.6% of all ETGs in the MaNGA. The remaining 32% are late-type galaxies (LTGs), corresponding to roughly 3.1% of all LTGs in MaNGA.

APPENDIX

A. ACKNOWLEDGMENTS

We thank Andrea Macciò and Michael Blanton for valuable comments and discussion on this study. Authors acknowledge the support from the Russian Science Foundation grant No. 21-72-00036 and the Interdisciplinary Scientific and Educational School of Moscow University “Fundamental and Applied Space Research.” DG and ER research on the analysis, comparison with LSB galaxies, and interpretation of the properties of stellar populations in CR galaxies was supported by the Russian Science Foundation (RSCF) grants No. 23-12-00146. Spectral observations reported in this paper were obtained with the Southern African Large Telescope (program 2020-1-SCI-002) supported by the National Research Foundation (NRF) of South Africa. AYK acknowledges the Ministry of Science and Higher Education of the Russian Federation grant 075-15-2022-262 (13.MNPMU.21.0003). This material is based upon work supported by Tamkeen under the NYU Abu Dhabi Research Institute grant CASS. Funding for the Sloan Digital Sky Survey IV has been provided by the Alfred P. Sloan Foundation, the U.S. Department of Energy Office of Science, and

the Participating Institutions. SDSS-IV acknowledges support and resources from the Center for High-Performance Computing at the University of Utah. The SDSS website is www.sdss.org.

SDSS-IV is managed by the Astrophysical Research Consortium for the Participating Institutions of the SDSS Collaboration including the Brazilian Participation Group, the Carnegie Institution for Science, Carnegie Mellon University, the Chilean Participation Group, the French Participation Group, Harvard-Smithsonian Center for Astrophysics, Instituto de Astrofísica de Canarias, The Johns Hopkins University, Kavli Institute for the Physics and Mathematics of the Universe (IPMU) / University of Tokyo, the Korean Participation Group, Lawrence Berkeley National Laboratory, Leibniz Institut für Astrophysik Potsdam (AIP), Max-Planck-Institut für Astronomie (MPIA Heidelberg), Max-Planck-Institut für Astrophysik (MPA Garching), Max-Planck-Institut für Extraterrestrische Physik (MPE), National Astronomical Observatories of China, New Mexico State University, New York University, University of Notre Dame, Observatório Nacional / MCTI, The Ohio State University, Pennsylvania State University, Shanghai Astronomical Observatory, United Kingdom Participation Group, Universidad Nacional Autónoma de México, University of Arizona, University of Colorado Boulder, University of Oxford, University of Portsmouth, University of Utah, University of Virginia, University of Washington, University of Wisconsin, Vanderbilt University, and Yale University.

This work made use of Astropy:⁴ a community-developed core Python package and an ecosystem of tools and resources for astronomy (Astropy Collaboration et al. 2013, 2018, 2022).

This research has made use of the NASA/IPAC Extragalactic Database (NED), which is funded by the National Aeronautics and Space Administration and operated by the California Institute of Technology. This research has made use of NASA’s Astrophysics Data System Bibliographic Services.

Facilities: SDSS(MaNGA)

Software: Astropy (Astropy Collaboration et al. 2013, 2018, 2022), lmfit (v1.0.3, Newville et al. 2014)

REFERENCES

- Abdurro’uf, Accetta, K., Aerts, C., et al. 2022, ApJS, 259, 35, doi: [10.3847/1538-4365/ac4414](https://doi.org/10.3847/1538-4365/ac4414)
- Aihara, H., AIsayyad, Y., Ando, M., et al. 2019, PASJ, 71, 114, doi: [10.1093/pasj/psz103](https://doi.org/10.1093/pasj/psz103)
- Algorry, D. G., Navarro, J. F., Abadi, M. G., et al. 2014a, MNRAS, 437, 3596, doi: [10.1093/mnras/stt2154](https://doi.org/10.1093/mnras/stt2154)
- . 2014b, MNRAS, 437, 3596, doi: [10.1093/mnras/stt2154](https://doi.org/10.1093/mnras/stt2154)
- Argudo-Fernández, M., Verley, S., Bergond, G., et al. 2015, A&A, 578, A110, doi: [10.1051/0004-6361/201526016](https://doi.org/10.1051/0004-6361/201526016)
- Asplund, M., Amarsi, A. M., & Grevesse, N. 2021, A&A, 653, A141, doi: [10.1051/0004-6361/202140445](https://doi.org/10.1051/0004-6361/202140445)
- Astropy Collaboration, Robitaille, T. P., Tollerud, E. J., et al. 2013, A&A, 558, A33, doi: [10.1051/0004-6361/201322068](https://doi.org/10.1051/0004-6361/201322068)
- Astropy Collaboration, Price-Whelan, A. M., Sipőcz, B. M., et al. 2018, AJ, 156, 123, doi: [10.3847/1538-3881/aabc4f](https://doi.org/10.3847/1538-3881/aabc4f)
- Astropy Collaboration, Price-Whelan, A. M., Lim, P. L., et al. 2022, apj, 935, 167, doi: [10.3847/1538-4357/ac7c74](https://doi.org/10.3847/1538-4357/ac7c74)
- Baldwin, J. A., Phillips, M. M., & Terlevich, R. 1981, PASP, 93, 5, doi: [10.1086/130766](https://doi.org/10.1086/130766)
- Bao, M., Chen, Y., Yang, M., et al. 2024, MNRAS, 528, 2643, doi: [10.1093/mnras/stae243](https://doi.org/10.1093/mnras/stae243)
- Bao, M., Chen, Y., Zhu, P., et al. 2022, ApJL, 926, L13, doi: [10.3847/2041-8213/ac52ad](https://doi.org/10.3847/2041-8213/ac52ad)
- Barnes, J. E. 1988, ApJ, 331, 699, doi: [10.1086/166593](https://doi.org/10.1086/166593)
- Belfiore, F., Westfall, K. B., Schaefer, A., et al. 2019, AJ, 158, 160, doi: [10.3847/1538-3881/ab3e4e](https://doi.org/10.3847/1538-3881/ab3e4e)
- Bender, R. 1988, A&A, 202, L5
- Beom, M., Walterbos, R. A. M., & Bizyaev, D. 2024, AJ, 168, 197, doi: [10.3847/1538-3881/ad6f0b](https://doi.org/10.3847/1538-3881/ad6f0b)
- Bertola, F., Buson, L. M., & Zeilinger, W. W. 1992, ApJL, 401, L79, doi: [10.1086/186675](https://doi.org/10.1086/186675)
- Bertola, F., Cinzano, P., Corsini, E. M., et al. 1996, ApJL, 458, L67, doi: [10.1086/309924](https://doi.org/10.1086/309924)
- Bevacqua, D., Cappellari, M., & Pellegrini, S. 2022, MNRAS, 511, 139, doi: [10.1093/mnras/stab3732](https://doi.org/10.1093/mnras/stab3732)
- Blanton, M. R., Kazin, E., Muna, D., Weaver, B. A., & Price-Whelan, A. 2011, AJ, 142, 31, doi: [10.1088/0004-6256/142/1/31](https://doi.org/10.1088/0004-6256/142/1/31)
- Boissier, S., Boselli, A., Ferrarese, L., et al. 2016, A&A, 593, A126, doi: [10.1051/0004-6361/201629226](https://doi.org/10.1051/0004-6361/201629226)
- Bundy, K., Bershady, M. A., Law, D. R., et al. 2015, ApJ, 798, 7, doi: [10.1088/0004-637X/798/1/7](https://doi.org/10.1088/0004-637X/798/1/7)
- Cenci, E., Feldmann, R., Gensior, J., et al. 2024, ApJL, 961, L40, doi: [10.3847/2041-8213/ad1ffb](https://doi.org/10.3847/2041-8213/ad1ffb)
- Chang, Y.-Y., van der Wel, A., da Cunha, E., & Rix, H.-W. 2015, ApJS, 219, 8, doi: [10.1088/0067-0049/219/1/8](https://doi.org/10.1088/0067-0049/219/1/8)
- Chilingarian, I., Prugniel, P., Sil’chenko, O., & Koleva, M. 2007a, in IAU Symposium, Vol. 241, Stellar Populations as Building Blocks of Galaxies, ed. A. Vazdekis & R. Peletier, 175–176, doi: [10.1017/S1743921307007752](https://doi.org/10.1017/S1743921307007752)

⁴ <http://www.astropy.org>

- Chilingarian, I. V., Mieske, S., Hilker, M., & Infante, L. 2011, *MNRAS*, 412, 1627, doi: [10.1111/j.1365-2966.2010.18000.x](https://doi.org/10.1111/j.1365-2966.2010.18000.x)
- Chilingarian, I. V., Prugniel, P., Sil'chenko, O. K., & Afanasiev, V. L. 2007b, *MNRAS*, 376, 1033, doi: [10.1111/j.1365-2966.2007.11549.x](https://doi.org/10.1111/j.1365-2966.2007.11549.x)
- Chilingarian, I. V., Zolotukhin, I. Y., Katkov, I. Y., et al. 2017, *ApJS*, 228, 14, doi: [10.3847/1538-4365/228/2/14](https://doi.org/10.3847/1538-4365/228/2/14)
- Coccatto, L., Morelli, L., Corsini, E. M., et al. 2011, *MNRAS*, 412, L113, doi: [10.1111/j.1745-3933.2011.01016.x](https://doi.org/10.1111/j.1745-3933.2011.01016.x)
- Coccatto, L., Morelli, L., Pizzella, A., et al. 2013, *A&A*, 549, A3, doi: [10.1051/0004-6361/201220460](https://doi.org/10.1051/0004-6361/201220460)
- Coccatto, L., Fabricius, M., Morelli, L., et al. 2015, *A&A*, 581, A65, doi: [10.1051/0004-6361/201526560](https://doi.org/10.1051/0004-6361/201526560)
- Combes, F. 2014, in *Astronomical Society of the Pacific Conference Series*, Vol. 480, *Structure and Dynamics of Disk Galaxies*, ed. M. S. Seigar & P. Treuthardt, 211, doi: [10.48550/arXiv.1309.1603](https://doi.org/10.48550/arXiv.1309.1603)
- Crocker, A. F., Jeong, H., Komugi, S., et al. 2009, *MNRAS*, 393, 1255, doi: [10.1111/j.1365-2966.2008.14295.x](https://doi.org/10.1111/j.1365-2966.2008.14295.x)
- Dey, A., Schlegel, D. J., Lang, D., et al. 2019, *AJ*, 157, 168, doi: [10.3847/1538-3881/ab089d](https://doi.org/10.3847/1538-3881/ab089d)
- Drory, N., MacDonald, N., Bershady, M. A., et al. 2015, *AJ*, 149, 77, doi: [10.1088/0004-6256/149/2/77](https://doi.org/10.1088/0004-6256/149/2/77)
- Duarte Puertas, S., Vilchez, J. M., Iglesias-Páramo, J., et al. 2022, *A&A*, 666, A186, doi: [10.1051/0004-6361/202141571](https://doi.org/10.1051/0004-6361/202141571)
- Efstathiou, G., Ellis, R. S., & Carter, D. 1982, *MNRAS*, 201, 975, doi: [10.1093/mnras/201.4.975](https://doi.org/10.1093/mnras/201.4.975)
- Egorov, O. V., & Moiseev, A. V. 2019, *MNRAS*, 486, 4186, doi: [10.1093/mnras/stz1112](https://doi.org/10.1093/mnras/stz1112)
- Etherington, J., & Thomas, D. 2015, *MNRAS*, 451, 660, doi: [10.1093/mnras/stv999](https://doi.org/10.1093/mnras/stv999)
- Evans, N. W., & Collett, J. L. 1994, *ApJL*, 420, L67, doi: [10.1086/187164](https://doi.org/10.1086/187164)
- Falcón-Barroso, J., & Martig, M. 2021, *A&A*, 646, A31, doi: [10.1051/0004-6361/202039624](https://doi.org/10.1051/0004-6361/202039624)
- Fioc, M., & Rocca-Volmerange, B. 1997, *A&A*, 500, 507, <https://arxiv.org/abs/astro-ph/9707017>
- Fitzpatrick, E. L. 1999, *PASP*, 111, 63, doi: [10.1086/316293](https://doi.org/10.1086/316293)
- Franx, M., Illingworth, G., & Heckman, T. 1989, *ApJ*, 344, 613, doi: [10.1086/167830](https://doi.org/10.1086/167830)
- Franx, M., & Illingworth, G. D. 1988, *ApJL*, 327, L55, doi: [10.1086/185139](https://doi.org/10.1086/185139)
- Freeman, K. C. 1970, *ApJ*, 160, 811, doi: [10.1086/150474](https://doi.org/10.1086/150474)
- Gasymov, D., & Katkov, I. 2024, in *Astronomical Society of the Pacific Conference Series*, Vol. 535, *Astromical Data Analysis Software and Systems XXXI*, ed. B. V. Hugo, R. Van Rooyen, & O. M. Smirnov, 279
- Gasymov, D. F. O., & Katkov, I. 2022, in *The Multifaceted Universe: Theory and Observations - 2000*, 17, doi: [10.48550/arXiv.2209.11240](https://doi.org/10.48550/arXiv.2209.11240)
- Ginsburg, A., Robitaille, T., & Beaumont, C. 2016, *pvextractor: Position-Velocity Diagram Extractor*, *Astrophysics Source Code Library*, record ascl:1608.010
- Graham, M. T., Cappellari, M., Li, H., et al. 2018, *MNRAS*, 477, 4711, doi: [10.1093/mnras/sty504](https://doi.org/10.1093/mnras/sty504)
- Gunn, J. E., Siegmund, W. A., Mannery, E. J., et al. 2006, *AJ*, 131, 2332, doi: [10.1086/500975](https://doi.org/10.1086/500975)
- Hafen, Z., Faucher-Giguère, C.-A., Anglés-Alcázar, D., et al. 2017, *MNRAS*, 469, 2292, doi: [10.1093/mnras/stx952](https://doi.org/10.1093/mnras/stx952)
- Hagen, L. M. Z., Seibert, M., Hagen, A., et al. 2016, *ApJ*, 826, 210, doi: [10.3847/0004-637X/826/2/210](https://doi.org/10.3847/0004-637X/826/2/210)
- Haynes, M. P., Giovanelli, R., Kent, B. R., et al. 2018, *ApJ*, 861, 49, doi: [10.3847/1538-4357/aac956](https://doi.org/10.3847/1538-4357/aac956)
- Hinshaw, G., Larson, D., Komatsu, E., et al. 2013, *ApJS*, 208, 19, doi: [10.1088/0067-0049/208/2/19](https://doi.org/10.1088/0067-0049/208/2/19)
- Izquierdo-Villalba, D., Bonoli, S., Rosas-Guevara, Y., et al. 2022, *MNRAS*, 514, 1006, doi: [10.1093/mnras/stac1413](https://doi.org/10.1093/mnras/stac1413)
- Jedrzejewski, R., & Schechter, P. L. 1988, *ApJL*, 330, L87, doi: [10.1086/185211](https://doi.org/10.1086/185211)
- Jin, Y., Chen, Y., Shi, Y., et al. 2016, *MNRAS*, 463, 913, doi: [10.1093/mnras/stw2055](https://doi.org/10.1093/mnras/stw2055)
- Johnston, E. J., Merrifield, M. R., Aragón-Salamanca, A., & Cappellari, M. 2013, *MNRAS*, 428, 1296, doi: [10.1093/mnras/sts121](https://doi.org/10.1093/mnras/sts121)
- Jore, K. P., Broeils, A. H., & Haynes, M. P. 1996, *AJ*, 112, 438, doi: [10.1086/118027](https://doi.org/10.1086/118027)
- Junais, Weilbacher, P. M., Epinat, B., et al. 2024, *A&A*, 681, A100, doi: [10.1051/0004-6361/202347669](https://doi.org/10.1051/0004-6361/202347669)
- Kasparova, A. V., Katkov, I. Y., & Chilingarian, I. V. 2020, *MNRAS*, 493, 5464, doi: [10.1093/mnras/staa611](https://doi.org/10.1093/mnras/staa611)
- Katkov, I., Gasymov, D., Gelfand, J. D., et al. 2024a, in *Astronomical Society of the Pacific Conference Series*, Vol. 535, *Astromical Data Analysis Software and Systems XXXI*, ed. B. V. Hugo, R. Van Rooyen, & O. M. Smirnov, 239, doi: [10.48550/arXiv.2112.03291](https://doi.org/10.48550/arXiv.2112.03291)
- Katkov, I. Y., Gasymov, D., Kniazev, A. Y., et al. 2024b, *ApJ*, 962, 27, doi: [10.3847/1538-4357/ad1331](https://doi.org/10.3847/1538-4357/ad1331)
- Katkov, I. Y., Kniazev, A. Y., & Sil'chenko, O. K. 2015, *AJ*, 150, 24, doi: [10.1088/0004-6256/150/1/24](https://doi.org/10.1088/0004-6256/150/1/24)
- Katkov, I. Y., Kniazev, A. Y., Sil'chenko, O. K., & Gasymov, D. 2022, *A&A*, 658, A154, doi: [10.1051/0004-6361/202141934](https://doi.org/10.1051/0004-6361/202141934)
- Katkov, I. Y., Sil'chenko, O. K., & Afanasiev, V. L. 2013, *ApJ*, 769, 105, doi: [10.1088/0004-637X/769/2/105](https://doi.org/10.1088/0004-637X/769/2/105)
- . 2014, *MNRAS*, 438, 2798, doi: [10.1093/mnras/stt2365](https://doi.org/10.1093/mnras/stt2365)

- Katkov, I. Y., Sil'chenko, O. K., Chilingarian, I. V., Uklein, R. I., & Egorov, O. V. 2016, *MNRAS*, 461, 2068, doi: [10.1093/mnras/stw1452](https://doi.org/10.1093/mnras/stw1452)
- Kauffmann, G., Heckman, T. M., Tremonti, C., et al. 2003, *MNRAS*, 346, 1055, doi: [10.1111/j.1365-2966.2003.07154.x](https://doi.org/10.1111/j.1365-2966.2003.07154.x)
- Kewley, L. J., Dopita, M. A., Sutherland, R. S., Heisler, C. A., & Trevena, J. 2001, *ApJ*, 556, 121, doi: [10.1086/321545](https://doi.org/10.1086/321545)
- Khim, D. J., Yi, S. K., Pichon, C., et al. 2021, *ApJS*, 254, 27, doi: [10.3847/1538-4365/abf043](https://doi.org/10.3847/1538-4365/abf043)
- Khoperskov, S., Zinchenko, I., Avramov, B., et al. 2021, *MNRAS*, 500, 3870, doi: [10.1093/mnras/staa3330](https://doi.org/10.1093/mnras/staa3330)
- Khrapov, S. S., & Khoperskov, A. V. 2024, *Open Astronomy*, 33, 20220231, doi: [10.1515/astro-2022-0231](https://doi.org/10.1515/astro-2022-0231)
- Krajnović, D., Emsellem, E., Cappellari, M., et al. 2011, *MNRAS*, 414, 2923, doi: [10.1111/j.1365-2966.2011.18560.x](https://doi.org/10.1111/j.1365-2966.2011.18560.x)
- Kroupa, P. 2001, *MNRAS*, 322, 231, doi: [10.1046/j.1365-8711.2001.04022.x](https://doi.org/10.1046/j.1365-8711.2001.04022.x)
- Kuijken, K., Fisher, D., & Merrifield, M. R. 1996, *MNRAS*, 283, 543, doi: [10.1093/mnras/283.2.543](https://doi.org/10.1093/mnras/283.2.543)
- Law, D. R., Yan, R., Bershad, M. A., et al. 2015, *AJ*, 150, 19, doi: [10.1088/0004-6256/150/1/19](https://doi.org/10.1088/0004-6256/150/1/19)
- Law, D. R., Cherinka, B., Yan, R., et al. 2016, *AJ*, 152, 83, doi: [10.3847/0004-6256/152/4/83](https://doi.org/10.3847/0004-6256/152/4/83)
- Law, D. R., Westfall, K. B., Bershad, M. A., et al. 2021, *AJ*, 161, 52, doi: [10.3847/1538-3881/abcaa2](https://doi.org/10.3847/1538-3881/abcaa2)
- Lejeune, T., Cuisinier, F., & Buser, R. 1997, *A&AS*, 125, 229, doi: [10.1051/aas:1997373](https://doi.org/10.1051/aas:1997373)
- Lelli, F., Fraternali, F., & Sancisi, R. 2010, *A&A*, 516, A11, doi: [10.1051/0004-6361/200913808](https://doi.org/10.1051/0004-6361/200913808)
- Lu, S., Xu, D., Wang, Y., et al. 2021, *MNRAS*, 503, 726, doi: [10.1093/mnras/stab497](https://doi.org/10.1093/mnras/stab497)
- Mancera Piña, P. E., Posti, L., Pezzulli, G., et al. 2021, *A&A*, 651, L15, doi: [10.1051/0004-6361/202141574](https://doi.org/10.1051/0004-6361/202141574)
- Mazzilli Ciraulo, B., Melchior, A.-L., Maschmann, D., et al. 2021, *A&A*, 653, A47, doi: [10.1051/0004-6361/202141319](https://doi.org/10.1051/0004-6361/202141319)
- Merrifield, M. R., & Kuijken, K. 1994, *ApJ*, 432, 575, doi: [10.1086/174596](https://doi.org/10.1086/174596)
- Mitzkus, M., Cappellari, M., & Walcher, C. J. 2017, *MNRAS*, 464, 4789, doi: [10.1093/mnras/stw2677](https://doi.org/10.1093/mnras/stw2677)
- Miyazaki, S., Komiyama, Y., Kawanomoto, S., et al. 2018, *PASJ*, 70, S1, doi: [10.1093/pasj/psx063](https://doi.org/10.1093/pasj/psx063)
- Morelli, L., Pizzella, A., Coccato, L., et al. 2017, *A&A*, 600, A76, doi: [10.1051/0004-6361/201630046](https://doi.org/10.1051/0004-6361/201630046)
- Newville, M., Stensitzki, T., Allen, D. B., & Ingargiola, A. 2014, *LMFIT: Non-Linear Least-Square Minimization and Curve-Fitting for Python, 0.8.0*, Zenodo, Zenodo, doi: [10.5281/zenodo.11813](https://doi.org/10.5281/zenodo.11813)
- Peirani, S., Suto, Y., Han, S., et al. 2025, arXiv e-prints, arXiv:2502.17902, doi: [10.48550/arXiv.2502.17902](https://doi.org/10.48550/arXiv.2502.17902)
- Pilyugin, L. S., & Grebel, E. K. 2016, *MNRAS*, 457, 3678, doi: [10.1093/mnras/stw238](https://doi.org/10.1093/mnras/stw238)
- Pizzella, A., Corsini, E. M., Vega Beltrán, J. C., & Bertola, F. 2004, *A&A*, 424, 447, doi: [10.1051/0004-6361:20047183](https://doi.org/10.1051/0004-6361:20047183)
- Pizzella, A., Morelli, L., Coccato, L., et al. 2018, *A&A*, 616, A22, doi: [10.1051/0004-6361/201731712](https://doi.org/10.1051/0004-6361/201731712)
- Pizzella, A., Morelli, L., Corsini, E. M., et al. 2014, *A&A*, 570, A79, doi: [10.1051/0004-6361/201424746](https://doi.org/10.1051/0004-6361/201424746)
- Puerari, I., & Pfenniger, D. 2001, *Ap&SS*, 276, 909, doi: [10.1023/A:1017581325673](https://doi.org/10.1023/A:1017581325673)
- Putman, M. E. 2017, in *Astrophysics and Space Science Library*, Vol. 430, Gas Accretion onto Galaxies, ed. A. Fox & R. Davé, 1, doi: [10.1007/978-3-319-52512-9_1](https://doi.org/10.1007/978-3-319-52512-9_1)
- Rix, H.-W., Franx, M., Fisher, D., & Illingworth, G. 1992, *ApJL*, 400, L5, doi: [10.1086/186635](https://doi.org/10.1086/186635)
- Rubin, V. C. 1994, *AJ*, 108, 456, doi: [10.1086/117083](https://doi.org/10.1086/117083)
- Rubin, V. C., Graham, J. A., & Kenney, J. D. P. 1992, *ApJL*, 394, L9, doi: [10.1086/186460](https://doi.org/10.1086/186460)
- Rubino, M., Pizzella, A., Morelli, L., et al. 2021, *A&A*, 654, A30, doi: [10.1051/0004-6361/202140702](https://doi.org/10.1051/0004-6361/202140702)
- Saburova, A. S., Chilingarian, I. V., Kasparova, A. V., et al. 2021, *MNRAS*, 503, 830, doi: [10.1093/mnras/stab374](https://doi.org/10.1093/mnras/stab374)
- Saburova, A. S., Chilingarian, I. V., Katkov, I. Y., et al. 2018, *MNRAS*, 481, 3534, doi: [10.1093/mnras/sty2519](https://doi.org/10.1093/mnras/sty2519)
- Saburova, A. S., Chilingarian, I. V., Kulier, A., et al. 2023, *MNRAS*, 520, L85, doi: [10.1093/mnrasl/slاد005](https://doi.org/10.1093/mnrasl/slاد005)
- Saburova, A. S., Gasymov, D., Rubtsov, E. V., et al. 2024, *ApJ*, 973, 167, doi: [10.3847/1538-4357/ad67e0](https://doi.org/10.3847/1538-4357/ad67e0)
- Salim, S., Lee, J. C., Janowiecki, S., et al. 2016, *ApJS*, 227, 2, doi: [10.3847/0067-0049/227/1/2](https://doi.org/10.3847/0067-0049/227/1/2)
- Sancisi, R., Fraternali, F., Oosterloo, T., & van der Hulst, T. 2008, *A&A Rv*, 15, 189, doi: [10.1007/s00159-008-0010-0](https://doi.org/10.1007/s00159-008-0010-0)
- Sil'chenko, O., Moiseev, A. V., Smirnova, A., & Uklein, R. 2023, *Galaxies*, 11, 119, doi: [10.3390/galaxies11060119](https://doi.org/10.3390/galaxies11060119)
- Smee, S. A., Gunn, J. E., Uomoto, A., et al. 2013, *AJ*, 146, 32, doi: [10.1088/0004-6256/146/2/32](https://doi.org/10.1088/0004-6256/146/2/32)
- Smirnov, D. V., & Reshetnikov, V. P. 2020, *Astronomy Letters*, 46, 501, doi: [10.1134/S1063773720080046](https://doi.org/10.1134/S1063773720080046)
- Stark, D. V., Masters, K. L., Avila-Reese, V., et al. 2021, *MNRAS*, 503, 1345, doi: [10.1093/mnras/stab566](https://doi.org/10.1093/mnras/stab566)
- Thakar, A. R., & Ryden, B. S. 1996a, *ApJ*, 461, 55, doi: [10.1086/177037](https://doi.org/10.1086/177037)
- . 1996b, *ApJ*, 461, 55, doi: [10.1086/177037](https://doi.org/10.1086/177037)
- . 1998, *ApJ*, 506, 93, doi: [10.1086/306223](https://doi.org/10.1086/306223)
- Toomre, A., & Toomre, J. 1972, *ApJ*, 178, 623, doi: [10.1086/151823](https://doi.org/10.1086/151823)

- van de Voort, F., & Schaye, J. 2012, MNRAS, 423, 2991,
doi: [10.1111/j.1365-2966.2012.20949.x](https://doi.org/10.1111/j.1365-2966.2012.20949.x)
- Vazdekis, A., Koleva, M., Ricciardelli, E., Röck, B., &
Falcón-Barroso, J. 2016, MNRAS, 463, 3409,
doi: [10.1093/mnras/stw2231](https://doi.org/10.1093/mnras/stw2231)
- Vázquez-Mata, J. A., Hernández-Toledo, H. M.,
Avila-Reese, V., et al. 2022, MNRAS, 512, 2222,
doi: [10.1093/mnras/stac635](https://doi.org/10.1093/mnras/stac635)
- Wake, D. A., Bundy, K., Diamond-Stanic, A. M., et al.
2017, AJ, 154, 86, doi: [10.3847/1538-3881/aa7ecc](https://doi.org/10.3847/1538-3881/aa7ecc)
- Wang, H., Mo, H. J., Yang, X., et al. 2016, ApJ, 831, 164,
doi: [10.3847/0004-637X/831/2/164](https://doi.org/10.3847/0004-637X/831/2/164)
- Westfall, K. B., Cappellari, M., Bershady, M. A., et al.
2019, AJ, 158, 231, doi: [10.3847/1538-3881/ab44a2](https://doi.org/10.3847/1538-3881/ab44a2)
- Yan, R., Bundy, K., Law, D. R., et al. 2016, AJ, 152, 197,
doi: [10.3847/0004-6256/152/6/197](https://doi.org/10.3847/0004-6256/152/6/197)
- Zinchenko, I. A. 2023, A&A, 674, L7,
doi: [10.1051/0004-6361/202346846](https://doi.org/10.1051/0004-6361/202346846)

APPENDIX

A. COMPARISON WITH OTHER SEARCHES

In this section, we compare our sample with previous studies [Graham et al. \(2018\)](#), [Bevacqua et al. \(2022\)](#), [Bao et al. \(2022, 2024\)](#), and [Beom et al. \(2024\)](#).

A.1. *Graham et al. (2018)*

The first extensive analysis of angular momentum in the MaNGA SDSS-IV sample (~ 2300 targets) was conducted by [Graham et al. \(2018\)](#). A total of 22 2σ galaxies were identified. Of these, 12 galaxies are included in our sample, while galaxy 1-113520 was classified as a gas-polar system. The remaining galaxies do not exhibit clear CR features.

A.2. *Bevacqua et al. (2022)*

The next sample of galaxies with the stellar counter-rotation phenomenon was selected from MaNGA DR16 (~ 4600 targets) by [Bevacqua et al. \(2022\)](#). Limiting our sample to MaNGA DR16 leaves 63 galaxies (64 in the [Bevacqua et al. \(2022\)](#)). Of these, 35 galaxies match between the samples, while 29 are found only in the [Bevacqua et al. \(2022\)](#) sample. Among these 29, four exhibit kinematic misalignment between gas and stars (Sec. B). The remaining 25 galaxies were rechecked, revealing no signs of 2σ , S-rotation, or CR-GS features, except for one (1-549076), which exhibits a strong 2σ feature. We analyzed this galaxy using our pipeline, but the recovered non-parametric LOSVD did not show any noticeable X-shape.

We expect counter-rotating disks to be younger than the main component and to co-rotate with the gaseous component, as found in all our galaxies with two-component spectral decomposition. [Bevacqua et al. \(2022\)](#) identified two galaxies (1-38543 and 1-248410) where the gas co-rotates with an older disk. We fitted the first galaxy (1-38543) using a two-component NBURSTS decomposition, confirming co-rotation between the gas and a younger component (Fig. 6). The next galaxy (1-248410) is a part of our probable sample (Tab. 3). Due to low SNR, our pipeline retrieves only the luminosity-weighted SSP equivalent age, which does not exhibit a reliable gradient from the center to the outer regions. This does not allow us to determine whether the gas disk is associated with a younger or older component.

A.3. *Bao et al. (2022, 2024)*

The sample from [Bao et al. \(2022\)](#), based on MaNGA DR17 ($\sim 10,000$ galaxies), includes 101 galaxies exhibiting stellar counter-rotation with a regularly rotating gas disk. Our sample is slightly larger (120 galaxies), but after filtering out those without ionized gas, 101 counter-rotating galaxies remain.

The [Bao et al. \(2022\)](#) sample was categorized into four types (Types 1 and 2, each with subtypes a and b). Type “1” in their classification corresponds to S-rotation in our notation, while Type “2” lacks this feature but exhibits either 2σ or σ -elongated structures. Subtypes “1a” and “2b” indicate cases where the ionized gas rotates in the opposite direction to the outer regions (CR-GS feature in our notation), whereas “1b” and “2a” denote gas co-rotation with the outer parts. In our classification scheme, the former represents inner counter-rotation, while the latter corresponds to outer counter-rotation.

A key aspect highlighted by [Bao et al. \(2022\)](#) is the distinction between “a” and “b” types based on their specific star formation rate (sSFR) distributions. These galaxies were divided into three categories: the blue cloud (BC, $\log \text{sSFR} > -11 \text{ yr}^{-1}$), the red sequence (RS, $\log \text{sSFR} < -14 \text{ yr}^{-1}$), and the green valley (GV), where sSFR lies between these limits. The fraction of “b” type galaxies increases from the BC to RS populations, whereas the “a” type decreases. However, in our sample, where sSFR data is taken from GSWLC ([Salim et al. 2016](#)), this correlation is absent. Notably, we lack RS galaxies, as the minimum sSFR in our sample is $\log \text{sSFR} \approx -13.3 \text{ yr}^{-1}$. To assess consistency, we cross-matched the sSFR estimates from Salim ([Salim et al. 2016](#)) and Chang ([Chang et al. 2015](#)), finding general agreement within the margin of error. However, Chang’s estimates for $\log \text{sSFR} < -11 \text{ yr}^{-1}$ exhibit significant uncertainties, with large 1σ errors of about 1–1.5 dex. We used demarcation values of $\log \text{sSFR} = -10.8 \text{ yr}^{-1}$ and $\log \text{sSFR} = -11.8 \text{ yr}^{-1}$ (Fig. 2) and confirmed sSFR differences between the “a” and “b” types, consistent with findings in [Bao et al. \(2022\)](#) (Fig. 2):

Table 8. Population difference on SFR– M_* diagram (Fig. 2) in “a” and “b” types of CR.

	1a	1b	2a	2b
BC	100%	0%	62%	38%
GV	62%	38%	25%	75%
RS	43%	57%	29%	71%

The galaxy 1-339061, which hosts an inner CR disk, was studied in detail by Bao et al. (2024). The flux ratio between the primary and secondary disks is about 1.8, which could be converted to a CR disk luminosity weight of $1/(1+1.8) \approx 36\%$, close to our estimate of $W_{L, CR} \approx 33\%$. The parameters of stellar populations of both disks agree within error bounds (Tab. 5 and Fig. 9 in Bao et al. (2024)). Mass-weight estimates differ (16% compared to our $\approx 8\%$), but this discrepancy arises from variations in the definition of mass-to-light ratios. However, the CR disk masses in this galaxy converge because we applied a $(100/H_0)^2$ correction to NSA masses, which increased the stellar mass of the galaxy by a factor of ~ 2 .

A.4. Beom et al. (2024)

Beom et al. (2024) focused on galaxies exhibiting gaseous CR, though they also marked galaxies with stellar CR (type “CS”). This sample contains 29 CR galaxies, of which 25 have inner CR (ICS, in their notation) and 4 have outer (OCS, in their notation). 20 galaxies match our sample, but one galaxy (1-26197) does not conform to our CR disk configuration. In the Beom et al. (2024) sample, this galaxy is marked as ICS, but the recovered LOSVD clearly shows a large-scale CR disk (third row from the bottom in the central column of Fig. 5). The remaining nine galaxies are included in the full sample of kinematically decoupled galaxies (Tab. 9): 1-195979 (CR-GS), 1-295542 (CR-GS, NRR), 1-92702 (CR-GS), 1-246298 (CR-GS, NRR), 1-261386 (Gas-mis), 1-546345 (CR-GS), 1-294016 ($2\sigma?$), 1-35832 (CR-GS), 1-634718 (Srot, CR-GS), but they do not show clear CR features. We have rechecked their kinematic maps and recovered LOSVDs, confirming our classification and the absence of CR.

B. EXTENDED SAMPLE OF GALAXIES WITH DECOUPLED KINEMATICS

Table 9. Table with kinematically decoupled galaxies (excluding stellar CR). Description is similar to Tab. 2.

No.	ID	R.A.	Dec.	Type	$\log M_*$	z	Features	Environment	Morphology
(1)	(2)	(3)	(4)	(5)	(6)	(7)	(8)	(9)	(10)
1	1-178443	17:23:01.1	27:34:10.10	SABbc	10.22	0.048	2σ	Cl, G	...
2	1-209407	15:53:02.8	46:46:04.79	SABbc	9.40	0.020	2σ	Cl, G	E
3	1-248565	16:10:50.2	38:42:29.67	SABa	9.83	0.038	2σ	Cl, G	...
4	1-269886	16:33:59.1	26:53:52.71	Edc	10.95	0.071	2σ	Cl, G	...
5	1-282020	12:18:39.6	43:32:19.40	SBd	9.61	0.024	2σ	F, G	B
6	1-603965	03:07:32.3	-00:57:52.40	Edc	11.40	0.039	2σ	V, G	Sh
7	1-78294	09:48:16.2	03:54:21.08	Sbc	10.08	0.024	2σ	F, G	E
8	1-97176	21:13:09.8	-07:37:54.36	Sa	10.44	0.028	2σ	V, G	Sh
9	12-84617	15:25:54.9	41:54:35.18	SABa	9.13	0.023	2σ	Sh, G, O	...
10	1-60334	09:58:22.5	01:35:04.95	Sb	9.97	0.028	2σ	F, G	...
11	1-594318	16:11:58.1	29:50:18.73	Edc	11.62	0.050	2σ , NRR	Cl, G	T, Sh, C
12	1-179395	21:05:00.4	-00:55:59.82	SABab	9.26	0.018	2σ , other	V, G	LSB
13	1-247630	15:39:45.2	46:01:30.01	Sa	10.76	0.038	2σ , star/gas-polar	Cl, P, G	T, Sh, P
14	1-131278	15:00:40.2	55:29:19.41	S0	9.83	0.026	$2\sigma?$	Sh, G	...
15	1-135772	16:41:32.5	37:15:59.02	Edc	11.27	0.101	$2\sigma?$	Cl, G	T
16	1-135949	16:49:29.4	36:02:22.16	SABb	9.91	0.031	$2\sigma?$	F, G	E

Table 9 continued

Table 9 (continued)

No.	ID	R.A.	Dec.	Type	log M_*	z	Features	Environment	Morphology
(1)	(2)	(3)	(4)	(5)	(6)	(7)	(8)	(9)	(10)
17	1-294016	16:57:17.0	19:20:22.14	Sa	9.61	0.033	2 σ ?	Sh, G	E
18	1-301360	09:46:51.9	35:15:03.96	Scd	9.61	0.039	2 σ ?	Cl, G	E
19	1-420979	13:35:04.9	31:00:41.61	S0a	9.61	0.017	2 σ ?	F, G	...
20	1-60713	10:05:35.0	03:03:13.01	SABbc	10.12	0.024	2 σ ?	Sh, G	...
21	1-151914	12:45:45.4	52:57:03.22	Sd	9.43	0.023	2 σ ?	Sh, G	E
22	1-109392	03:23:41.4	-00:07:01.32	Edc	11.20	0.051	CR-GS	V, P, G	T, C
23	1-115650	22:18:59.4	13:11:14.93	Edc	10.45	0.027	CR-GS	V, G	C
24	1-118363	23:24:54.1	14:12:54.72	Sb	9.89	0.026	CR-GS	V, G	...
25	1-118369	23:26:03.1	14:37:46.61	Sab	10.12	0.042	CR-GS	V, G	...
26	1-118383	23:24:52.2	14:08:20.19	S0	10.05	0.040	CR-GS	V, G	...
27	1-118456	23:24:48.2	15:00:00.23	SB0a	10.89	0.031	CR-GS	V, G	B
28	1-122057	08:03:29.5	38:26:32.21	S0	9.94	0.040	CR-GS	F, G, O	...
29	1-133944	15:55:39.1	47:39:42.93	SABab	9.44	0.019	CR-GS	Cl, P, G	...
30	1-135165	16:28:36.2	40:41:08.00	Edc	11.08	0.076	CR-GS	F, G	...
31	1-135177	16:25:52.1	41:03:28.05	S0a	9.57	0.029	CR-GS	Cl, G	...
32	1-135239	16:25:56.9	41:31:19.43	E	10.01	0.043	CR-GS	V, P, G, O	...
33	1-135568	16:30:52.3	41:17:10.15	S0	11.21	0.094	CR-GS	V, P, G, O	T, C
34	1-135577	16:30:56.0	40:26:31.38	Sb	9.61	0.027	CR-GS	Cl, G	...
35	1-135773	16:41:49.4	37:18:33.34	Sab	11.38	0.099	CR-GS	Cl, G	LSB
36	1-138140	09:41:13.9	47:41:18.96	Edc	10.50	0.047	CR-GS	Sh, G, O	...
37	1-146344	08:00:16.1	29:28:17.17	Sb	10.14	0.045	CR-GS	Sh, G, O	E
38	1-149871	11:33:57.0	51:14:59.20	S0	10.68	0.026	CR-GS	Cl, G, O	...
39	1-153077	07:56:53.3	32:20:44.13	S0	10.27	0.043	CR-GS	Sh, G, O	E
40	1-156061	09:34:47.3	48:44:51.27	S0	9.91	0.026	CR-GS	F, G, O	...
41	1-167141	10:00:54.8	44:45:53.26	S0	9.84	0.028	CR-GS	Sh, G, O	...
42	1-177203	17:03:06.7	34:38:16.64	SAB0a	10.81	0.058	CR-GS	F, G	...
43	1-177610	17:09:44.2	32:09:38.84	Sa	9.63	0.037	CR-GS	V, G	C
44	1-178790	20:41:29.5	00:07:56.12	Sa	10.04	0.027	CR-GS	V, G	E
45	1-195979	13:28:49.0	53:26:34.51	E	10.00	0.025	CR-GS	F, G	...
46	1-197573	14:44:54.0	48:38:30.93	S0	10.53	0.050	CR-GS	F, P, G	...
47	1-199340	15:32:39.6	44:32:03.06	S0a	9.85	0.038	CR-GS	Cl, G, O	...
48	1-201364	07:48:47.9	28:14:23.07	Sa	9.96	0.028	CR-GS	V, O	...
49	1-201936	08:02:18.4	32:32:07.81	Sa	10.47	0.038	CR-GS	F, G	T, C
50	1-210863	16:24:17.6	39:12:39.75	E	10.84	0.030	CR-GS	Cl, G, O	...
51	1-217050	09:06:52.8	41:24:29.71	S0	10.82	0.027	CR-GS	Cl, P, G, O	...
52	1-217537	07:48:49.6	21:43:57.40	S0a	9.83	0.024	CR-GS	F, P, G, O	C
53	1-225	09:43:23.4	00:40:32.64	Sa	9.93	0.027	CR-GS	V, G	E
54	1-22572	17:16:15.3	64:29:41.30	S0	9.67	0.035	CR-GS	Sh, G	...
55	1-229012	03:48:27.0	-00:47:19.43	SAB0	10.95	0.040	CR-GS	V, G	...
56	1-235307	14:05:54.8	45:38:40.83	S0	9.96	0.040	CR-GS	Sh, G, O	...
57	1-235530	14:17:41.3	45:27:56.95	SAB0	10.32	0.027	CR-GS	Sh, G, O	T, LSB
58	1-23568	17:03:09.9	59:39:36.80	Edc	10.73	0.055	CR-GS	F, G	...
59	1-236099	15:00:56.7	41:33:58.55	SBab	9.94	0.020	CR-GS	Sh, G, O	B, E
60	1-24055	17:08:33.4	57:28:36.13	Sa	9.64	0.030	CR-GS	F, G	...
61	1-245088	14:10:26.9	54:37:10.47	S0a	10.15	0.040	CR-GS	Cl, P, G, O	E
62	1-24547	17:25:52.6	53:32:22.01	S0a	10.49	0.030	CR-GS	F, P, G	E, C
63	1-247223	15:21:22.2	48:24:56.86	Sa	10.51	0.027	CR-GS	F, G	E
64	1-248133	15:51:38.8	43:38:22.54	S0	9.98	0.040	CR-GS	Cl, G, O	E
65	1-248443	16:09:16.5	41:44:44.62	SB0	10.64	0.026	CR-GS	F, G, O	B
66	1-248618	16:12:37.2	39:25:08.49	SB0a	10.61	0.032	CR-GS	F, G	B, Sh
67	1-249383	16:39:08.6	34:15:44.48	Edc	11.47	0.097	CR-GS	Cl, G	T
68	1-251067	13:49:54.7	43:28:56.06	Sab	10.28	0.045	CR-GS	Sh, G, O	...
69	1-256234	11:08:14.2	43:37:29.34	E	11.38	0.076	CR-GS	Cl, G, O	...

Table 9 continued

Table 9 (continued)

No.	ID	R.A.	Dec.	Type	log M_*	z	Features	Environment	Morphology
(1)	(2)	(3)	(4)	(5)	(6)	(7)	(8)	(9)	(10)
70	1-256283	11:11:35.7	43:35:28.72	S0	10.87	0.061	CR-GS	F, G, O	...
71	1-256819	11:17:24.9	44:33:47.87	S0	10.94	0.066	CR-GS	Cl, G, O	...
72	1-25725	17:31:59.2	59:58:17.90	E	10.34	0.029	CR-GS	F, G	T, Sh
73	1-261224	14:12:55.3	39:18:45.55	Sb	10.11	0.025	CR-GS	F, G	E
74	1-26587	22:04:25.3	00:42:55.49	SAB0	11.13	0.043	CR-GS	V, G	...
75	1-269212	16:09:57.0	30:06:23.50	S0	10.40	0.048	CR-GS	V, P, O	E
76	1-271717	16:12:15.2	31:49:07.41	S0a	10.46	0.049	CR-GS	F, G	...
77	1-272473	16:25:40.3	29:08:51.39	Sc	10.29	0.044	CR-GS	F, G, O	E
78	1-279532	11:23:14.0	46:59:52.09	SBa	10.33	0.025	CR-GS	F, G, O	B, E
79	1-283580	12:43:41.0	41:09:16.27	Sb	9.90	0.023	CR-GS	F, G	E
80	1-283903	12:51:04.5	48:24:30.86	Edc	10.34	0.049	CR-GS	F, P, G	T
81	1-284321	13:07:01.2	46:18:33.96	S0	10.11	0.024	CR-GS	F, G, O	E
82	1-293928	16:57:16.2	18:27:09.51	Edc	9.55	0.033	CR-GS	Sh, G	...
83	1-296799	16:11:47.6	28:23:40.89	SABa	9.69	0.031	CR-GS	F, G	...
84	1-301495	09:45:14.9	35:22:09.50	S0	10.60	0.051	CR-GS	F, G	...
85	1-317979	16:03:57.2	24:24:08.07	S0a	9.82	0.037	CR-GS	V, G	...
86	1-318434	16:12:07.7	23:43:05.32	S0a	10.57	0.032	CR-GS	Cl, G	T, Sh
87	1-319646	13:34:41.8	50:27:51.01	Sa	10.28	0.029	CR-GS	Sh, G	E
88	1-319706	13:23:22.8	50:10:12.56	E	10.41	0.048	CR-GS	Sh, G	T
89	1-322240	15:16:02.3	42:08:46.46	Sa	11.02	0.075	CR-GS	Cl, G, O	E
90	1-325871	16:57:15.0	26:50:10.82	S0	10.68	0.036	CR-GS	F, G	T, Sh
91	1-326103	17:05:38.5	25:12:30.08	SBa	11.03	0.038	CR-GS	Cl, G	B
92	1-333290	15:01:51.7	09:43:33.38	Sab	10.66	0.034	CR-GS	F, G	Sh
93	1-336458	15:45:04.4	08:33:34.78	S0	9.97	0.042	CR-GS	Cl, G	...
94	1-337237	15:58:54.1	09:31:19.70	SAB0a	9.92	0.040	CR-GS	F, G	...
95	1-338746	07:47:25.2	43:55:07.04	E	10.48	0.032	CR-GS	Cl, G, O	...
96	1-339094	07:49:53.4	45:14:54.53	S0a	10.48	0.031	CR-GS	Cl, G, O	...
97	1-351572	07:50:09.8	48:28:43.97	S0a	10.00	0.022	CR-GS	Cl, G, O	E
98	1-35391	01:54:41.0	-00:08:36.03	SBa	10.69	0.019	CR-GS	V, G	B, LSB
99	1-35832	02:04:30.5	00:25:52.20	SAB0a	9.14	0.019	CR-GS	V, G	E
100	1-379008	07:55:02.7	52:13:38.77	Sab	9.67	0.023	CR-GS	V, G, O	E
101	1-380032	08:11:56.4	56:58:44.43	SB0a	10.63	0.027	CR-GS	F, G	B
102	1-38510	03:32:05.6	00:28:45.81	Sb	9.59	0.022	CR-GS	V, G	E
103	1-38887	03:36:21.4	00:11:12.81	Sb	9.63	0.024	CR-GS	V, G	E
104	1-397739	12:25:15.3	40:23:47.93	Edc	11.22	0.067	CR-GS	Cl, G	T
105	1-404060	12:31:25.2	36:49:34.00	Sab	9.40	0.022	CR-GS	F, G	E
106	1-405760	13:04:24.7	36:28:47.82	Sb	10.18	0.023	CR-GS	F, G, O	E, T, Sh
107	1-409368	13:07:38.4	31:29:13.10	Sa	9.98	0.026	CR-GS	F, G	E
108	1-40992	01:27:25.2	14:03:16.30	SABab	10.47	0.024	CR-GS	V, G	...
109	1-412566	08:15:08.3	20:09:49.79	S0a	10.28	0.044	CR-GS	F, G	...
110	1-412833	08:25:38.4	21:08:33.21	S0	9.85	0.023	CR-GS	V, G, O	...
111	1-415354	13:18:42.2	32:55:07.19	Sa	9.76	0.036	CR-GS	Cl, G, O	E
112	1-415754	13:39:52.8	29:22:46.92	S0	10.01	0.044	CR-GS	Cl, P, G	E, C
113	1-419380	12:12:01.9	35:24:15.84	Sa	9.98	0.024	CR-GS	V, G, O	...
114	1-42255	01:49:41.7	13:05:49.64	S0	9.47	0.034	CR-GS	V, G	...
115	1-424438	13:54:05.4	24:57:59.86	S0	10.23	0.030	CR-GS	Cl, G, O	E
116	1-42583	01:57:03.8	13:10:01.41	S0	10.72	0.032	CR-GS	V, P, G	...
117	1-42626	01:54:14.5	13:40:43.29	SABa	10.14	0.021	CR-GS	V, G	...
118	1-43717	07:48:22.5	43:46:49.78	Edc	10.06	0.031	CR-GS	Cl, G, O	Sh, P
119	1-445333	16:26:37.4	13:41:00.32	Edc	10.68	0.034	CR-GS	F, G	T, Sh
120	1-458301	13:39:33.9	25:33:21.96	SAB0	10.36	0.026	CR-GS	F, G, O	...
121	1-48136	08:51:39.1	57:06:26.72	E	10.17	0.026	CR-GS	F, G, O	...
122	1-487046	11:03:34.3	21:02:58.10	Sb	9.29	0.021	CR-GS	F, G, O	E

Table 9 continued

Table 9 (continued)

No.	ID	R.A.	Dec.	Type	log M_*	z	Features	Environment	Morphology
(1)	(2)	(3)	(4)	(5)	(6)	(7)	(8)	(9)	(10)
123	1-519412	13:35:06.5	22:39:42.60	S0a	10.07	0.032	CR-GS	F, G, O	E
124	1-53278	09:02:49.2	01:01:14.22	Sa	10.71	0.053	CR-GS	F, G	...
125	1-546345	16:17:03.9	19:00:26.81	SBb	9.67	0.036	CR-GS	F, G	B
126	1-547295	17:16:44.0	32:48:22.56	S0a	9.85	0.041	CR-GS	Sh, G, O	E
127	1-556703	08:27:26.4	23:34:07.59	SABa	10.22	0.018	CR-GS	F, P, G	T, Sh, C
128	1-561039	17:13:05.1	35:16:07.02	Sb	10.29	0.026	CR-GS	F	E
129	1-564487	16:13:02.2	39:14:13.67	E	10.54	0.033	CR-GS	F, G	C
130	1-575704	13:11:34.0	44:55:59.08	SBab	10.24	0.025	CR-GS	Sh, G	B, T
131	1-576335	15:00:14.5	53:06:03.13	E	11.11	0.086	CR-GS	Cl, P, G	C
132	1-576537	13:12:34.0	48:21:59.82	Sb	10.66	0.056	CR-GS	F, P, G	E, C
133	1-593898	15:32:45.3	08:15:18.26	E	11.19	0.043	CR-GS	F, G	T, C
134	1-594098	15:55:43.3	47:52:02.20	Edc	11.15	0.020	CR-GS	Cl, G	T
135	1-627331	13:46:12.7	23:03:13.81	S0	10.73	0.027	CR-GS	Cl, G	...
136	1-636700	22:57:53.0	12:57:34.43	Sb	9.79	0.026	CR-GS	V, G	E
137	1-66669	13:13:52.4	02:07:57.23	Sab	10.57	0.030	CR-GS	F, G	T, Sh
138	1-71956	07:53:46.0	38:52:08.52	S0	9.86	0.040	CR-GS	Cl, G, O	...
139	1-76744	08:53:06.7	03:48:52.74	Sa	9.87	0.028	CR-GS	F, G	E
140	1-76995	09:02:06.6	03:29:51.73	Edc	10.14	0.027	CR-GS	Sh, G	...
141	1-77738	09:34:21.1	03:06:34.08	S0a	9.58	0.028	CR-GS	Sh, G	...
142	1-78715	10:04:03.9	04:16:53.20	Sa	10.66	0.054	CR-GS	Sh, G	E, C
143	1-79648	10:28:50.0	04:57:38.03	SB0	10.21	0.023	CR-GS	F, G	B
144	1-91923	15:55:32.4	50:28:42.93	S0a	10.24	0.044	CR-GS	F, G	C
145	1-92702	16:08:23.9	48:56:40.25	Edc	10.24	0.044	CR-GS	F, G	...
146	1-92908	16:16:06.0	50:54:55.66	Edc	11.03	0.047	CR-GS	F, G	...
147	1-95058	16:47:00.8	39:03:40.83	S0a	10.49	0.029	CR-GS	F, G	...
148	12-129608	13:40:10.7	26:50:27.75	Sb	9.78	0.032	CR-GS	F, G, O	E
149	12-84677	15:28:37.9	42:26:31.26	SB0a	11.21	0.075	CR-GS	Cl, G, O	B, T
150	1-113242	21:06:50.3	09:11:50.53	Edc	11.20	0.044	CR-GS	V, G	...
151	1-401759	13:21:13.4	30:28:41.20	Sb	9.79	0.037	CR-GS	F, G	E
152	1-547402	17:13:59.0	33:36:25.69	Sb	9.95	0.039	CR-GS	F, G, O	E
153	1-244629	13:44:21.6	55:51:21.45	SBb	10.80	0.037	CR-GS	F, G	B, E
154	1-201392	07:51:26.5	28:14:03.18	Sa	10.32	0.023	CR-GS	F, O	E
155	1-145920	07:57:25.6	27:26:25.36	S0	9.71	0.027	CR-GS	Cl, G, O	...
156	1-251374	14:15:05.4	40:20:23.51	SAB0a	9.92	0.042	CR-GS, $2\sigma?$	Sh, G	...
157	1-44113	08:00:49.5	44:41:28.21	S0	11.41	0.102	CR-GS, $2\sigma?$	Cl, G, O	T, Sh, C
158	1-149329	11:13:26.8	51:47:23.43	S0a	10.13	0.026	CR-GS, NRR	F, G	C
159	1-246298	14:49:44.8	50:42:39.21	SAB0	9.63	0.013	CR-GS, NRR	F, G, O	...
160	1-284174	12:57:55.3	42:56:14.23	S0	9.74	0.035	CR-GS, NRR	Sh, G, O	...
161	1-295542	16:25:01.4	24:15:47.36	Edc	10.45	0.050	CR-GS, NRR	Sh, G, O	...
162	1-151874	12:49:27.1	51:34:54.87	S0	10.29	0.032	CR-GS, σ -elong.	F, G	T
163	1-385167	08:34:30.9	25:47:31.76	Sb	9.76	0.029	CR-GS?	Cl, G, O	E
164	1-201307	07:47:59.5	29:11:26.48	S0	9.55	0.027	Gas-mis	V, O	...
165	1-114820	22:01:41.6	11:51:24.44	Sa	10.93	0.030	Gas-mis	V, G	T, Sh
166	1-118427	23:25:13.0	15:47:39.51	Edc	11.24	0.105	Gas-mis	V, G	T
167	1-121648	07:58:52.3	35:02:33.59	S0a	11.07	0.083	Gas-mis	F, G	...
168	1-131060	14:58:11.3	57:00:03.47	SAB0a	9.83	0.028	Gas-mis	Sh, G	...
169	1-134004	15:53:47.7	47:24:17.84	Sa	9.54	0.019	Gas-mis	Cl, G, O	...
170	1-135056	16:31:08.1	40:23:17.10	SABa	10.07	0.029	Gas-mis	Cl, G	...
171	1-135101	16:29:55.3	40:39:35.85	Sa	10.00	0.029	Gas-mis	Cl, P, G, O	...
172	1-135517	16:33:49.6	39:15:47.54	Sab	10.84	0.032	Gas-mis	Cl, P, G, O	LSB
173	1-135664	16:37:20.5	41:11:20.31	S0	10.67	0.032	Gas-mis	F, G, O	T, Sh
174	1-135794	16:39:04.8	39:17:26.82	S0	10.67	0.030	Gas-mis	F, G, O	E
175	1-146292	08:02:47.9	29:28:11.38	S0a	10.34	0.046	Gas-mis	F, G, O	E

Table 9 continued

Table 9 (continued)

No.	ID	R.A.	Dec.	Type	log M_*	z	Features	Environment	Morphology
(1)	(2)	(3)	(4)	(5)	(6)	(7)	(8)	(9)	(10)
176	1-148949	11:00:47.6	49:54:06.76	SAB0	9.97	0.026	Gas-mis	F, G, O	...
177	1-149496	11:30:29.3	50:45:54.97	SB0a	10.11	0.026	Gas-mis	F, G, O	B
178	1-152632	07:45:58.2	29:42:55.44	Sa	10.19	0.024	Gas-mis	V, G, O	E
179	1-152700	07:46:08.3	31:01:11.80	E	10.79	0.059	Gas-mis	Cl, G, O	...
180	1-153254	07:56:05.5	33:44:40.35	Edc	11.35	0.074	Gas-mis	Cl, G, O	...
181	1-153402	08:07:57.2	34:13:38.37	S0	9.80	0.022	Gas-mis	Sh, P, G	T, LSB
182	1-1655	10:10:16.1	-00:04:29.25	E	11.26	0.096	Gas-mis	Cl, G	T, Sh
183	1-167582	10:17:55.4	46:36:11.83	SABab	10.10	0.030	Gas-mis	Sh, G, O	...
184	1-174119	11:17:08.9	48:32:19.51	S0	10.09	0.025	Gas-mis	F, G, O	...
185	1-1756	10:21:44.5	-00:40:19.76	Edc	11.45	0.096	Gas-mis	F, G	T, Sh
186	1-175911	12:18:59.7	51:16:42.32	E	11.13	0.047	Gas-mis	Cl, G	C
187	1-176422	16:56:13.0	33:35:26.10	E	10.74	0.056	Gas-mis	F, G, O	...
188	1-177974	17:18:24.1	29:42:20.77	Edc	10.15	0.029	Gas-mis	F, G	...
189	1-178824	20:46:38.1	00:20:21.69	SB0	9.77	0.013	Gas-mis	V, G	B
190	1-180080	21:35:00.4	-00:30:41.20	Edc	10.60	0.030	Gas-mis	V, G	T, Sh
191	1-180163	21:29:48.5	-00:18:48.80	S0	10.54	0.030	Gas-mis	V	T, Sh
192	1-180208	21:29:12.5	-00:37:18.33	S0	10.59	0.030	Gas-mis	V, G	E, T
193	1-189283	11:55:07.0	55:14:33.84	S0	9.86	0.020	Gas-mis	Cl, G	...
194	1-195282	13:07:27.1	54:02:15.72	S0	10.54	0.030	Gas-mis	Cl, G	...
195	1-195623	13:16:29.8	52:56:01.03	S0a	11.02	0.033	Gas-mis	Cl, P, G	LSB
196	1-195763	13:07:21.8	53:35:12.62	E	10.83	0.029	Gas-mis	Cl, G	T, Sh
197	1-196372	13:36:29.0	52:25:13.01	SBa	10.67	0.029	Gas-mis	F, G	B, Sh
198	1-198052	14:45:25.0	49:07:40.37	S0a	9.89	0.037	Gas-mis	Sh, P, G	...
199	1-198125	14:53:33.9	48:41:55.65	SAB0	10.44	0.036	Gas-mis	F, G, O	Sh
200	1-198182	14:58:59.9	48:24:35.48	S0	11.03	0.036	Gas-mis	Cl, G, O	T, Sh
201	1-198212	15:09:30.4	46:29:33.63	E	11.12	0.038	Gas-mis	V, G, O	T, Sh
202	1-198238	15:05:44.7	46:47:18.94	S0a	9.95	0.038	Gas-mis	V, G, O	...
203	1-199415	15:37:51.1	43:30:04.61	SABab	9.19	0.017	Gas-mis	V, G, O	...
204	1-200602	16:15:52.7	36:59:50.87	E	10.83	0.031	Gas-mis	F	T, Sh
205	1-210774	16:27:55.2	39:15:31.76	Edc	10.92	0.029	Gas-mis	Cl, P, G, O	C
206	1-211165	16:34:30.9	37:41:43.59	S0	11.15	0.099	Gas-mis	Cl, G	T, Sh
207	1-211277	16:30:32.7	39:23:03.06	Sa	10.60	0.030	Gas-mis	Cl, G	...
208	1-213422	08:36:57.8	03:42:26.84	Sa	10.30	0.029	Gas-mis	Sh, G	E
209	1-213820	08:39:39.2	03:49:42.77	SABa	10.02	0.027	Gas-mis	F, P, G	...
210	1-214335	08:55:42.0	04:59:41.25	Edc	10.69	0.028	Gas-mis	F, G	...
211	1-217500	09:45:05.6	45:35:13.33	Sb	9.54	0.016	Gas-mis	Sh, G, O	E
212	1-217662	07:48:05.3	22:54:02.83	SB0a	10.61	0.029	Gas-mis	F, G	B, C
213	1-218808	08:29:41.4	30:41:16.71	Edc	11.22	0.048	Gas-mis	Cl, G	T, Sh
214	1-22298	16:53:42.6	62:25:11.99	SAB0	10.83	0.061	Gas-mis	F, G	T
215	1-229879	08:04:08.9	24:33:31.00	Sa	10.31	0.044	Gas-mis	F, G	LSB
216	1-230100	08:10:56.5	25:41:04.97	SB0	10.53	0.025	Gas-mis	F, G, O	B
217	1-230867	08:40:02.4	29:49:02.81	Sa	11.34	0.065	Gas-mis	Cl, G	T, Sh
218	1-234004	13:14:58.4	48:11:40.63	SB0	10.46	0.049	Gas-mis	Sh, G, O	B
219	1-234172	13:06:04.0	50:14:59.01	Edc	11.12	0.047	Gas-mis	Cl, G	Sh
220	1-234980	14:00:13.2	46:25:55.94	E	10.71	0.053	Gas-mis	F, G, O	...
221	1-236175	15:09:32.9	42:29:23.70	E	10.78	0.059	Gas-mis	Sh, G, O	...
222	1-24018	17:10:19.7	56:45:26.11	S0	10.70	0.033	Gas-mis	V, G	Sh
223	1-24104	17:11:49.8	57:35:22.37	Edc	11.01	0.030	Gas-mis	Cl, G	T
224	1-24295	17:30:42.3	56:38:21.80	S0	10.77	0.029	Gas-mis	F, G	...
225	1-24476	17:38:43.3	57:14:21.15	Sa	10.67	0.030	Gas-mis	F, G	T, Sh
226	1-247300	15:23:59.1	48:47:34.28	Sa	11.18	0.074	Gas-mis	Cl, G	T, Sh
227	1-247628	15:40:04.5	46:06:21.39	S0	10.79	0.037	Gas-mis	Cl, G, O	...
228	1-259091	12:42:19.8	45:26:16.32	SAB0a	10.50	0.047	Gas-mis	F, P, G, O	...

Table 9 continued

Table 9 (continued)

No.	ID	R.A.	Dec.	Type	log M_*	z	Features	Environment	Morphology
(1)	(2)	(3)	(4)	(5)	(6)	(7)	(8)	(9)	(10)
229	1-261386	14:16:59.9	39:39:59.98	Sa	9.72	0.025	Gas-mis	F, G	...
230	1-263219	15:21:55.9	33:30:54.23	S0	10.85	0.062	Gas-mis	Cl, G, O	E
231	1-26462	22:11:27.4	-00:03:02.16	S0	11.12	0.052	Gas-mis	V, G	T, Sh
232	1-265671	16:05:00.7	27:15:29.66	E	10.25	0.046	Gas-mis	F, G	...
233	1-272299	16:14:12.5	31:29:25.62	S0	10.32	0.031	Gas-mis	F, P, G	...
234	1-273282	16:54:36.2	24:03:49.08	E _{dc}	10.95	0.035	Gas-mis	Cl, G	T, Sh
235	1-27571	22:40:28.1	-00:14:57.81	SOa	11.26	0.058	Gas-mis	V	T
236	1-279073	11:22:21.2	46:25:49.81	SB0a	10.74	0.032	Gas-mis	F, G, O	B, T, Sh
237	1-281439	12:09:25.5	46:32:57.69	E	10.97	0.069	Gas-mis	F, G, O	...
238	1-281927	12:12:14.0	43:21:22.64	SB0a	10.30	0.024	Gas-mis	F, G	B
239	1-284349	13:05:28.5	45:34:54.75	S0	10.53	0.051	Gas-mis	F, G, O	...
240	1-286746	14:02:00.1	45:33:42.87	E	11.25	0.065	Gas-mis	F, P, G	T, Sh
241	1-28715	23:07:48.9	00:56:25.96	SOa	11.30	0.042	Gas-mis	V, G	T, Sh
242	1-294189	16:50:54.1	20:31:22.58	S0	10.74	0.055	Gas-mis	F, G	...
243	1-295474	16:30:39.1	25:36:33.97	S0	10.97	0.042	Gas-mis	Cl, P, G, O	...
244	1-295721	16:23:13.8	26:28:45.46	E	11.13	0.064	Gas-mis	F, G, O	T, Sh
245	1-295996	16:17:31.2	24:17:23.74	SABa	10.84	0.067	Gas-mis	Cl, G, O	...
246	1-296316	16:19:15.0	25:08:41.12	E _{dc}	10.99	0.068	Gas-mis	F, G, O	...
247	1-296801	16:12:17.6	28:25:46.38	E	11.28	0.053	Gas-mis	F, G	T
248	1-296812	16:12:45.8	28:06:30.12	E	10.42	0.030	Gas-mis	F, G	T
249	1-29721	23:43:47.1	00:42:21.07	E _{dc}	11.13	0.093	Gas-mis	V, G	T, Sh
250	1-297924	07:47:04.6	18:35:26.27	SABa	10.52	0.051	Gas-mis	Cl, G, O	E
251	1-298319	08:13:17.0	22:38:53.95	Sa	10.10	0.022	Gas-mis	V, P, G	T, Sh
252	1-298835	08:24:19.5	25:40:28.10	Sa	9.87	0.028	Gas-mis	F, G, O	...
253	1-299496	08:44:49.1	28:18:53.59	Sa	9.39	0.021	Gas-mis	F, G	...
254	1-300663	09:17:35.7	33:39:13.79	S0	9.57	0.023	Gas-mis	Cl, G	...
255	1-301609	09:46:38.5	35:59:42.68	E _{dc}	10.11	0.022	Gas-mis	F, G	...
256	1-31432	00:25:37.7	00:02:12.20	E _{dc}	11.05	0.042	Gas-mis	V, P, G	...
257	1-315134	15:12:05.6	30:50:23.41	Sa	11.50	0.090	Gas-mis	V, G, O	T, Sh
258	1-320340	14:06:19.2	48:33:27.48	E _{dc}	10.89	0.063	Gas-mis	Cl, G	T
259	1-320543	14:12:02.4	50:08:13.55	SB0	10.54	0.049	Gas-mis	F, G	B
260	1-321127	14:26:55.0	48:05:59.64	SABa	10.20	0.026	Gas-mis	Sh, G	Sh
261	1-321221	14:38:54.4	46:39:56.21	E	10.96	0.036	Gas-mis	Cl, P, G, O	T, Sh, C
262	1-323420	16:18:26.9	33:42:52.57	E	10.53	0.048	Gas-mis	F, G	T
263	1-351790	08:04:35.5	50:42:30.81	S0	9.99	0.023	Gas-mis	Cl, P, G, O	...
264	1-35876	02:08:15.6	01:11:43.59	S	11.10	0.042	Gas-mis	V	T, Sh
265	1-35937	02:17:35.8	-00:29:36.92	S0	11.03	0.041	Gas-mis	V, G	...
266	1-363769	15:03:48.3	08:25:47.23	E	10.11	0.028	Gas-mis	F, G	...
267	1-37036	02:46:48.0	00:25:17.68	E _{dc}	10.80	0.028	Gas-mis	V, G	T, Sh
268	1-374549	15:24:36.4	28:46:30.07	E	11.12	0.087	Gas-mis	F, G, O	...
269	1-375532	15:36:39.0	25:54:24.57	E	11.43	0.095	Gas-mis	Cl, G	T, Sh
270	1-37754	03:09:17.0	-00:54:23.95	E	10.92	0.039	Gas-mis	V, G	...
271	1-379124	08:02:11.4	51:44:05.56	S0	10.68	0.055	Gas-mis	F, G, O	...
272	1-38041	03:17:49.8	-00:33:16.77	Sab	10.11	0.021	Gas-mis	V, G	...
273	1-382284	07:52:44.3	16:42:34.20	Sa	10.97	0.072	Gas-mis	Cl, G	T
274	1-386903	09:11:35.7	30:04:39.13	SBb	10.68	0.026	Gas-mis	F, G	B, E
275	1-386962	09:13:39.5	29:59:34.57	E _{dc}	11.18	0.023	Gas-mis	Cl, G	T, Sh, C
276	1-39480	00:42:21.5	14:15:15.70	SOa	10.73	0.055	Gas-mis	V, G	T
277	1-39922	01:06:17.8	14:03:54.02	S0	10.03	0.038	Gas-mis	V, G	...
278	1-402487	13:33:06.0	37:58:00.26	E _{dc}	10.67	0.053	Gas-mis	F, G, O	...
279	1-402576	13:34:06.2	39:41:18.19	SOa	10.37	0.046	Gas-mis	Sh, G, O	...
280	1-409482	13:02:44.6	32:05:06.04	S0	10.09	0.024	Gas-mis	F, G	E
281	1-412272	08:04:07.6	16:49:08.08	E	10.35	0.045	Gas-mis	F, G	...

Table 9 continued

Table 9 (continued)

No.	ID	R.A.	Dec.	Type	log M_*	z	Features	Environment	Morphology
(1)	(2)	(3)	(4)	(5)	(6)	(7)	(8)	(9)	(10)
282	1-42250	01:51:22.3	13:03:37.21	Sa	11.18	0.064	Gas-mis	V, G	T, Sh
283	1-42862	01:57:13.0	14:44:07.71	E	10.50	0.026	Gas-mis	V, P, G	...
284	1-43718	07:47:07.8	43:18:50.67	Edc	11.15	0.042	Gas-mis	Cl, G, O	T
285	1-43741	07:49:12.9	44:03:54.13	Edc	10.44	0.030	Gas-mis	Cl, G, O	...
286	1-43773	07:49:39.0	42:58:01.47	Edc	10.74	0.031	Gas-mis	Cl, P, G, O	...
287	1-43933	07:47:08.6	40:23:34.59	E	11.03	0.076	Gas-mis	Sh, G, O	T
288	1-44163	07:54:35.8	44:09:06.53	E	10.79	0.031	Gas-mis	Cl, G, O	...
289	1-44726	08:02:51.6	46:09:25.32	Edc	10.87	0.061	Gas-mis	F, G, O	T
290	1-456285	12:59:54.3	26:49:11.90	SABa	9.82	0.027	Gas-mis	Cl, G	...
291	1-457771	13:24:46.5	26:44:18.31	E	10.45	0.023	Gas-mis	F, G	T, Sh
292	1-458692	07:56:16.4	15:14:24.28	SBab	10.36	0.029	Gas-mis	Cl, G	B, LSB, Sh
293	1-462984	08:59:47.2	20:35:43.01	S0a	9.68	0.025	Gas-mis	Sh, P, G	...
294	1-474828	09:59:05.4	18:39:15.67	E	10.20	0.025	Gas-mis	F, G	C
295	1-487267	11:05:19.0	21:37:12.47	SABab	9.39	0.021	Gas-mis	F, G, O	...
296	1-50622	02:54:05.3	-07:20:42.26	Edc	10.78	0.031	Gas-mis	V, G	...
297	1-516559	12:00:27.8	23:37:31.39	Edc	10.68	0.053	Gas-mis	F, G	...
298	1-53060	08:49:33.1	01:43:40.91	Edc	11.16	0.069	Gas-mis	F, G	T, Sh
299	1-54435	09:30:16.1	01:27:47.73	SABab	11.12	0.083	Gas-mis	F, G	Sh
300	1-54497	09:26:23.2	01:34:54.36	E	10.67	0.056	Gas-mis	F, G	T, C
301	1-546250	16:07:09.9	18:38:28.54	S0	11.08	0.039	Gas-mis	Cl, P, G	C
302	1-547039	17:12:01.0	34:57:40.17	Edc	11.36	0.086	Gas-mis	F, G, O	T, Sh
303	1-54784	09:33:29.4	00:39:32.85	Edc	11.11	0.051	Gas-mis	Cl, G	T, Sh
304	1-550578	21:39:20.1	10:32:26.76	Edc	11.34	0.077	Gas-mis	V, G	...
305	1-556749	08:00:04.1	23:26:16.26	Edc	10.65	0.029	Gas-mis	Cl, P, G	T, C
306	1-558242	09:08:16.7	42:09:50.91	E	10.17	0.025	Gas-mis	F	...
307	1-560759	15:59:39.2	31:46:29.33	E	11.19	0.055	Gas-mis	Cl, G	T, C
308	1-563951	01:17:29.3	14:42:09.07	E	10.83	0.038	Gas-mis	V, G	T, C
309	1-575668	12:37:35.5	44:48:03.66	E	11.34	0.060	Gas-mis	F	T, Sh
310	1-576094	12:00:54.7	51:58:38.88	E	10.96	0.067	Gas-mis	F, G	...
311	1-584723	08:01:37.2	15:42:35.09	Sa	10.92	0.015	Gas-mis	F, G	T, Sh
312	1-585149	08:35:47.9	28:45:11.31	SBa	10.43	0.026	Gas-mis	Sh, G	B
313	1-591420	13:07:28.4	26:43:31.82	E	10.75	0.038	Gas-mis	F, P, G	C
314	1-593533	14:54:12.5	04:45:00.57	S0	11.32	0.028	Gas-mis	Cl, G	T
315	1-595166	17:22:38.3	30:52:12.17	S0	11.27	0.045	Gas-mis	F, G	T, C
316	1-604907	07:59:41.0	50:50:23.90	Edc	10.48	0.054	Gas-mis	Cl, G, O	...
317	1-606806	10:01:11.6	00:13:32.42	SABa	10.95	0.033	Gas-mis	Cl, G	T, Sh
318	1-612698	11:06:10.2	03:19:14.57	S0a	10.84	0.031	Gas-mis	F, P, G	T, C
319	1-617445	11:51:06.9	55:04:43.38	S-merger	10.96	0.019	Gas-mis	Cl, P, G	T, Sh
320	1-631803	15:04:39.8	53:49:23.14	S0	11.13	0.038	Gas-mis	F, G	...
321	1-641156	13:24:51.7	-01:02:06.30	SABa	11.26	0.107	Gas-mis	F, G	T, Sh
322	1-72211	08:04:25.4	39:55:50.25	S0a	10.24	0.040	Gas-mis	Cl, P, G, O	...
323	1-72595	08:16:19.9	43:26:51.49	S0a	10.43	0.024	Gas-mis	F, P, G	T, Sh
324	1-76813	08:58:05.3	03:45:23.37	SBa	9.91	0.027	Gas-mis	Sh, G	B
325	1-78200	09:56:58.7	03:46:40.66	SBa	10.99	0.035	Gas-mis	Cl, G	B, T
326	1-79976	10:37:23.3	05:26:18.70	S0	10.25	0.029	Gas-mis	F, G	...
327	1-92	09:44:55.6	00:04:05.59	SB0a	10.61	0.022	Gas-mis	Sh, G	B
328	1-95223	16:52:29.1	40:18:43.01	SAB0a	10.49	0.029	Gas-mis	F, G	...
329	1-96324	20:37:01.0	-05:59:49.45	S0	11.22	0.036	Gas-mis	V, G	T, Sh
330	1-605311	08:33:22.1	25:06:17.73	Edc	11.41	0.087	Gas-mis	F, G	...
331	1-94228	16:32:04.4	47:45:53.13	Sa	10.60	0.049	Gas-mis	Cl, P, G, O	...
332	1-523211	13:42:45.7	24:35:24.19	S0	10.24	0.027	Gas-mis	F, G, O	...
333	1-195176	12:51:54.4	54:57:40.06	S0	11.07	0.083	Gas-mis	Cl, G	T, Sh
334	1-114465	21:39:34.0	10:29:00.53	S0	10.97	0.079	Gas-mis, $2\sigma?$	V, G	T, Sh

Table 9 continued

Table 9 (continued)

No.	ID	R.A.	Dec.	Type	log M _*	z	Features	Environment	Morphology
(1)	(2)	(3)	(4)	(5)	(6)	(7)	(8)	(9)	(10)
335	1-201217	07:44:51.3	26:34:44.54	Edc	9.96	0.024	Gas-mis?	V, O	...
336	1-113520	21:10:00.5	11:30:38.33	S0	9.76	0.017	gas-polar	V, G	P
337	1-114245	21:31:37.6	11:49:53.97	Edc	10.97	0.029	gas-polar	V, G	T
338	1-114252	21:31:44.0	11:22:52.32	E	10.51	0.048	gas-polar	V, G	T
339	1-114818	22:01:20.9	12:11:48.09	SBa	10.54	0.029	gas-polar	V, G	B
340	1-114928	22:04:19.4	12:58:06.16	SAB0	10.63	0.027	gas-polar	V, G	P
341	1-117966	23:23:28.0	14:05:30.33	Sa	10.24	0.041	gas-polar	V, G	E
342	1-135055	16:30:33.9	40:32:21.85	Edc	11.02	0.030	gas-polar	Cl, P, G, O	...
343	1-137714	09:04:09.4	42:18:12.32	Sb	10.03	0.027	gas-polar	Cl, G, O	E
344	1-137845	09:17:14.1	44:29:20.98	Edc	10.99	0.032	gas-polar	Cl, G, O	...
345	1-144473	13:46:29.6	03:52:41.93	Sc	9.46	0.018	gas-polar	Sh, G	E
346	1-145922	07:57:15.5	27:29:45.66	E	10.75	0.027	gas-polar	Cl, P, G, O	P
347	1-149683	11:30:50.6	52:12:27.74	S0	10.80	0.034	gas-polar	F, G, O	E
348	1-151330	12:19:21.3	52:41:37.95	S0	9.92	0.031	gas-polar	F, G	...
349	1-152018	12:56:27.5	52:16:46.10	S0	9.79	0.038	gas-polar	Sh, P, G	C
350	1-163594	07:41:58.6	23:10:34.97	S0	11.03	0.043	gas-polar	F, G, O	...
351	1-164007	07:59:10.2	26:05:12.02	SBa	10.12	0.020	gas-polar	Sh, G, O	B
352	1-167334	10:07:34.8	46:05:38.34	S0	10.46	0.024	gas-polar	F, G, O	...
353	1-175599	12:09:19.0	50:56:13.48	Edc	11.15	0.084	gas-polar	Cl, G	C
354	1-176525	17:01:40.3	34:31:13.31	Sa	10.40	0.029	gas-polar	F, G	E
355	1-176908	17:04:24.7	33:22:33.17	S0a	10.56	0.030	gas-polar	F, G, O	Sh
356	1-178838	20:48:05.7	00:04:07.83	Sa	10.22	0.025	gas-polar	V, G	E, T, P
357	1-179248	21:00:04.0	00:11:54.19	Edc	10.62	0.051	gas-polar	V, G	...
358	1-195208	13:07:13.9	53:31:24.02	S0	9.93	0.029	gas-polar	Cl, G	...
359	1-195268	13:04:57.9	53:46:51.11	S0a	10.51	0.029	gas-polar	Cl, G	E
360	1-195690	13:12:41.0	53:42:53.05	SBa	10.39	0.024	gas-polar	F, P, G	B, C
361	1-198180	14:58:27.8	48:29:32.53	E	11.09	0.038	gas-polar	Cl, G, O	T, C
362	1-2072	10:21:04.4	00:09:41.70	Sb	11.26	0.113	gas-polar	Cl, G	T, C
363	1-207984	14:40:38.5	53:28:41.02	S0	9.87	0.038	gas-polar	F, P, G, O	...
364	1-209772	15:59:54.0	44:42:32.36	Edc	10.94	0.042	gas-polar	Cl, G, O	...
365	1-217324	09:20:52.4	42:42:31.68	S0	10.31	0.025	gas-polar	F, P, G, O	...
366	1-217999	08:03:16.5	24:40:36.40	S0	10.93	0.043	gas-polar	F, G	C
367	1-218764	08:31:09.8	29:47:40.83	Edc	10.96	0.068	gas-polar	F, G	T
368	1-22821	17:06:15.8	60:42:18.68	SABab	9.40	0.012	gas-polar	V, G	...
369	1-23958	17:15:24.5	57:19:20.99	Edc	11.02	0.030	gas-polar	Cl, P, G	C
370	1-24425	17:34:06.1	56:47:58.61	S0a	10.53	0.029	gas-polar	F, P, G	E, P
371	1-245451	14:09:06.9	53:27:48.66	Edc	11.06	0.078	gas-polar	F, G, O	...
372	1-246517	15:03:46.0	49:31:33.18	Sa	9.47	0.019	gas-polar	Sh, G, O	E, P
373	1-246542	15:03:13.0	49:51:04.16	Sa	10.57	0.028	gas-polar	Sh, G, O	E
374	1-2469	10:35:29.0	-00:23:59.24	S0	11.14	0.085	gas-polar	Cl, G	...
375	1-247449	15:31:32.4	45:39:27.35	E	10.54	0.029	gas-polar	F, G, O	...
376	1-249735	16:44:14.3	31:44:58.94	S0a	9.71	0.039	gas-polar	F, G	...
377	1-252632	15:02:42.9	37:56:57.67	E	10.71	0.029	gas-polar	F, G	...
378	1-256446	11:06:02.4	43:10:24.50	E	10.83	0.058	gas-polar	F, G, O	...
379	1-25680	17:27:52.5	60:05:50.19	E	10.77	0.028	gas-polar	Cl, P, G	...
380	1-258685	12:16:46.5	44:40:15.80	E	11.34	0.086	gas-polar	Cl, G, O	...
381	1-260744	13:52:15.3	38:56:06.29	S0	10.88	0.062	gas-polar	F, G, O	...
382	1-260809	13:52:15.3	40:08:56.86	S0	11.31	0.057	gas-polar	V, G, O	...
383	1-262876	15:20:41.1	33:21:55.31	S0	11.11	0.082	gas-polar	Cl, G, O	...
384	1-268764	16:07:20.2	30:28:46.60	Sb	9.91	0.022	gas-polar	Sh, G	E
385	1-269131	16:11:27.2	29:47:38.84	Sa	10.67	0.052	gas-polar	Cl, G	...
386	1-269951	16:36:12.7	25:55:52.56	Edc	11.23	0.052	gas-polar	Cl, G	...
387	1-272745	16:42:09.1	24:58:50.18	Sa	10.89	0.063	gas-polar	F, G	...

Table 9 continued

Table 9 (continued)

No.	ID	R.A.	Dec.	Type	log M_*	z	Features	Environment	Morphology
(1)	(2)	(3)	(4)	(5)	(6)	(7)	(8)	(9)	(10)
388	1-273933	10:17:58.2	37:10:53.70	Edc	11.09	0.044	gas-polar	F, G, O	P
389	1-280965	11:51:53.3	43:20:53.05	S0	9.76	0.036	gas-polar	Sh, G, O	...
390	1-285994	13:42:39.5	45:35:03.66	Edc	10.94	0.038	gas-polar	F, G	...
391	1-294587	16:41:18.9	22:16:43.53	SAB0	10.90	0.035	gas-polar	F, G	...
392	1-294599	16:41:30.4	22:14:56.04	Edc	10.10	0.023	gas-polar	Sh, G	...
393	1-296174	16:20:47.1	25:59:50.64	E	11.32	0.072	gas-polar	F, G	...
394	1-296900	16:07:06.9	27:58:43.56	S0	10.30	0.046	gas-polar	F, G	...
395	1-298310	08:03:09.4	21:15:59.39	SB0a	10.26	0.045	gas-polar	V, G	B, C
396	1-298693	08:18:47.6	24:32:14.75	SBab	10.42	0.025	gas-polar	Sh, G	B
397	1-300461	09:08:38.5	32:35:34.63	Sb	10.43	0.014	gas-polar	V, G	E
398	1-314676	15:10:08.9	31:53:16.21	Edc	10.96	0.030	gas-polar	F, G, O	T, Sh
399	1-314700	15:06:21.9	31:15:26.22	Edc	11.13	0.087	gas-polar	F, G, O	...
400	1-315675	15:22:02.0	31:13:59.02	S0	10.66	0.031	gas-polar	F, G, O	E
401	1-322262	15:15:56.3	43:10:00.40	S	10.03	0.018	gas-polar	F, G, O	E, T, P
402	1-334549	15:10:09.1	08:23:27.72	Edc	11.02	0.076	gas-polar	F, G	T
403	1-338633	07:33:01.3	42:25:30.44	Sa	10.62	0.027	gas-polar	Sh, G, O	...
404	1-351971	08:10:14.5	51:52:21.17	E	10.87	0.061	gas-polar	Cl, P, G	...
405	1-36564	02:32:19.5	00:40:19.08	S0a	9.15	0.022	gas-polar	V, G	...
406	1-369413	15:01:36.0	05:40:58.21	S0	11.33	0.114	gas-polar	Cl, G	...
407	1-376102	15:57:26.3	23:16:21.08	SAB0a	9.85	0.023	gas-polar	Sh, G	T
408	1-378401	07:51:37.0	48:00:01.90	S0	10.87	0.061	gas-polar	F, G, O	...
409	1-378770	07:56:28.8	50:17:16.31	E	11.57	0.134	gas-polar	V, G, O	T, Sh
410	1-379214	07:58:24.5	52:46:06.74	S0	10.54	0.023	gas-polar	F, G	T, P
411	1-38428	03:23:45.6	00:00:26.76	S0	10.64	0.036	gas-polar	V, G	...
412	1-384400	08:27:01.4	21:42:24.31	Sa	10.27	0.015	gas-polar	Cl, G, O	E
413	1-386077	08:53:50.4	24:40:54.85	S0	10.89	0.066	gas-polar	Cl, G, O	E, T, P
414	1-38618	03:30:29.4	-00:29:19.57	S0	9.67	0.022	gas-polar	V, G	...
415	1-394355	10:30:46.5	36:57:16.63	S0	11.04	0.039	gas-polar	F, G, O	T, Sh
416	1-40936	01:18:21.7	15:24:33.93	Edc	10.88	0.038	gas-polar	V, G	...
417	1-41092	01:20:12.1	14:33:40.59	Edc	11.16	0.038	gas-polar	V, G	T, Sh
418	1-415592	13:13:53.0	34:07:29.16	E	10.82	0.037	gas-polar	F, G	T, C
419	1-419166	13:16:57.1	32:09:21.79	Sab	10.81	0.061	gas-polar	F, G	...
420	1-42899	01:58:16.2	14:17:47.85	S0	10.75	0.026	gas-polar	V, G	...
421	1-44690	08:05:13.9	46:19:53.98	SAB0	10.47	0.029	gas-polar	Sh, G, O	...
422	1-459273	08:07:12.3	14:59:06.80	SABab	10.56	0.029	gas-polar	F, G	Sh
423	1-462964	09:01:39.5	20:45:00.32	S0	10.53	0.031	gas-polar	F, G	...
424	1-462966	09:01:11.0	20:36:38.54	S0	10.80	0.032	gas-polar	F, P, G	...
425	1-47429	08:39:48.4	54:34:50.77	S0a	10.23	0.045	gas-polar	Cl, G	...
426	1-51810	03:39:37.2	-05:37:58.56	Edc	10.04	0.021	gas-polar	V, G	...
427	1-523238	13:44:34.6	23:47:47.80	E	10.36	0.028	gas-polar	F, G, O	...
428	1-53681	09:01:52.1	01:59:35.81	E	10.70	0.057	gas-polar	Cl, G	...
429	1-548341	08:14:01.5	52:45:08.84	E	11.00	0.071	gas-polar	F, G	T, Sh
430	1-567284	09:12:24.4	29:00:12.25	Edc	11.24	0.103	gas-polar	V, G	C
431	1-567948	07:33:08.4	44:33:03.49	Edc	11.36	0.131	gas-polar	V	...
432	1-575898	11:13:30.5	44:39:57.38	Edc	10.92	0.068	gas-polar	Sh, G	...
433	1-584701	07:59:06.5	27:27:50.44	S-merger	10.62	0.023	gas-polar	Cl, G	T, Sh
434	1-584896	08:21:10.3	39:15:46.94	S0	10.91	0.029	gas-polar	F, G	T, C
435	1-586486	10:17:40.6	-00:28:53.94	E	10.85	0.034	gas-polar	Cl, P, G	T, C
436	1-591979	13:39:57.8	30:06:27.75	SB0	10.82	0.034	gas-polar	V, P, G	B
437	1-593648	15:08:42.6	28:10:16.16	SAB0	9.98	0.026	gas-polar	V, G	Sh
438	1-605306	08:32:59.3	25:59:27.40	S0a	9.91	0.018	gas-polar	F, P, G, O	T
439	1-605863	09:25:50.4	49:19:47.48	SBab	10.63	0.027	gas-polar	Cl, P, G	B, T, Sh, C
440	1-61484	10:38:56.6	02:40:44.42	S0	11.23	0.099	gas-polar	Cl, G	T

Table 9 continued

Table 9 (continued)

No.	ID	R.A.	Dec.	Type	log M_*	z	Features	Environment	Morphology
(1)	(2)	(3)	(4)	(5)	(6)	(7)	(8)	(9)	(10)
441	1-634825	17:37:49.3	57:06:38.54	Edc	10.90	0.030	gas-polar	F	T, Sh, C
442	1-635485	21:14:00.5	00:32:06.33	S0	10.41	0.027	gas-polar	V, G	Sh
443	1-67037	13:18:02.3	01:06:50.76	SABa	11.38	0.081	gas-polar	Cl, G	T, C
444	1-77016	09:02:29.4	03:23:06.02	Sb	10.69	0.027	gas-polar	Sh, P, G	...
445	1-79983	10:35:01.9	04:32:41.72	SABa	10.11	0.044	gas-polar	F, G	...
446	1-90685	15:39:38.5	55:19:38.48	S0	10.62	0.052	gas-polar	Cl, G, O	...
447	1-92735	16:10:51.8	48:54:39.50	SAB0	10.45	0.045	gas-polar	F, G	...
448	1-93908	16:29:19.6	43:51:48.17	S0	11.08	0.047	gas-polar	Cl, G, O	...
449	1-97189	21:14:54.2	-07:24:27.60	S0	10.84	0.029	gas-polar	V, P, G	Sh
450	1-576427	15:18:42.1	47:33:04.54	SAB0	11.18	0.057	gas-polar, σ -elong.	Cl, P, G	T, Sh
451	1-339111	07:51:51.5	46:04:09.95	Edc	11.14	0.052	KDC	Cl, G, O	C
452	1-212201	16:59:36.3	32:03:26.19	SB0	11.41	0.090	KDC?	V, G, O	B
453	1-55529	09:06:29.7	56:47:47.02	SABb	11.31	0.067	NRR	Cl, G, O	Sh, C
454	1-174225	11:20:14.1	50:01:31.15	E	10.19	0.026	NRR, 2σ ?	F, G, O	...
455	1-122304	08:07:41.0	39:00:15.26	SAB0a	10.50	0.023	other	Sh, G, O	...
456	1-201314	07:45:31.1	28:26:27.63	Sb	9.29	0.016	other	F, O	T
457	1-318518	16:18:38.2	23:56:33.28	SAB0	11.53	0.104	other	Cl, G, O	T, P
458	1-385124	08:37:37.0	24:59:59.27	Sa	10.80	0.029	other	Cl, G, O	P
459	1-585869	09:57:39.3	44:53:50.69	SAB0	10.65	0.026	other	F, P, G	C
460	1-593972	15:40:48.4	28:17:31.49	Edc	11.08	0.033	other	Cl, P, G	...
461	1-320614	14:23:36.6	48:26:10.22	Edc	11.33	0.074	Srot	Cl, G	T
462	1-375863	15:48:38.3	25:24:15.02	Edc	11.09	0.033	Srot	F	C
463	1-322291	15:19:10.9	43:12:16.40	S0	10.07	0.028	Srot, CR-GS	Sh, G, O	...
464	1-40719	01:13:40.3	14:28:07.89	S0	10.72	0.056	Srot, CR-GS	V, G	...
465	1-634718	17:18:31.1	60:35:09.99	SAB0a	9.52	0.013	Srot, CR-GS	V, P, G	C
466	1-382452	07:52:39.0	18:19:17.78	Sa	10.84	0.045	Srot, σ -elong.	F, G	T, Sh
467	1-41258	01:28:42.0	14:36:33.23	S0a	10.74	0.036	Srot, σ -elong., KDC	V, G	Sh
468	1-251788	14:20:55.0	40:07:15.70	Edc	10.13	0.018	Srot?, KDC?	F, G, O	T

C. ANALYSIS OF RECOVERED LOSVD AND TWO-COMPONENT FULL-SPECTRUM FITTING

Figures like Fig. 6 have been prepared for all galaxies in the sample and are available at <https://zenodo.org/records/15132551>.